GEOPHYSICS

A two-billion-year history for the lunar dynamo

Sonia M. Tikoo,[1,2,3,4]* Benjamin P. Weiss,[1,2] David L. Shuster,[2,3] Clément Suavet,[1] Huapei Wang,[1] Timothy L. Grove[1]

Magnetic studies of lunar rocks indicate that the Moon generated a core dynamo with surface field intensities of ~20 to 110 μT between at least 4.25 and 3.56 billion years ago (Ga). The field subsequently declined to <~4 μT by 3.19 Ga, but it has been unclear whether the dynamo had terminated by this time or just greatly weakened in intensity. We present analyses that demonstrate that the melt glass matrix of a young regolith breccia was magnetized in a ~5 ± 2 μT dynamo field at ~1 to ~2.5 Ga. These data extend the known lifetime of the lunar dynamo by at least 1 billion years. Such a protracted history requires an extraordinarily long-lived power source like core crystallization or precession. No single dynamo mechanism proposed thus far can explain the strong fields inferred for the period before 3.56 Ga while also allowing the dynamo to persist in such a weakened state beyond ~2.5 Ga. Therefore, our results suggest that the dynamo was powered by at least two distinct mechanisms operating during early and late lunar history.

INTRODUCTION

The Moon is a unique venue for exploring the longevity of dynamos generated by planetary bodies intermediate in size between planets and asteroids. A central conundrum is that the lunar dynamo was apparently intense and long-lived, with surface fields reaching ~20 to 110 μT between at least 4.25 and 3.56 billion years ago (Ga) (*1*–*6*). The field intensity then precipitously declined by at least an order of magnitude (possibly even to zero) by ~3.19 Ga (*7*–*9*). It is unknown whether this decrease reflects total cessation of the dynamo or whether the dynamo persisted beyond 3.56 Ga in a markedly weakened state.

The mechanisms that generated such a long-lived dynamo are uncertain but may include thermal convection (*10*–*13*) and mechanical stirring produced by differential rotation between the lunar core and mantle driven by impacts (*14*) or mantle precession (*15*, *16*). Geophysical evidence for a ~200- to ~280-km-radius solid inner core (*17*, *18*) within a larger ~220- to ~450-km-radius liquid outer core (*17*–*23*) also suggests that thermochemical convection resulting from core crystallization—the driving force behind the Earth's dynamo—may have helped sustain the dynamo (*24*–*26*). Without invoking special conditions, such as an early thermal blanket enveloping the lunar core, a hydrous lunar mantle, or a low core adiabatic heat flux, purely thermal convection dynamos are unlikely to persist beyond ~4 Ga (*6*). Impact-driven dynamos are transient [lasting up to a few thousand years after each large basin-forming impact (*14*)] and cannot have occurred after the last basin-forming impact at ~3.7 Ga (*5*). On the other hand, mantle precession or thermochemical convection may be capable of powering a dynamo well beyond 3.5 Ga (*6*).

Key to distinguishing between these lunar dynamo mechanisms is establishing the lifetime of the dynamo. However, the poor magnetic recording properties (*7*, *8*, *27*) and complex thermal and deformational histories of most lunar samples (*6*, *7*) as well as the rarity of young (<3.2 Ga) Apollo igneous samples have thus far hindered efforts to establish when the dynamo ultimately ceased. Although some Apollo-era studies have suggested that lunar samples as young as ~200 million years old (Ma) formed in lunar paleofields of ~1 to ~10 μT (*28*), most of these values are likely upper limits given the samples' magnetic recording fidelities (*8*, *27*, *29*). Furthermore, it has been proposed that impact-generated plasmas could generate transient magnetic fields [lasting up to ~1 day for large basin-forming impacts (*30*) or <~1 s for the small impacts after 3.7 Ga (*8*)] that could magnetize shocked and quickly cooled rocks throughout lunar history (*31*, *32*). Given these complexities, determining when the lunar dynamo actually ceased requires a young rock with exceptionally high-fidelity magnetic recording properties and a well-constrained thermal and shock history. To address these deficiencies, we conducted a new analysis of such a young lunar sample, glassy regolith breccia 15498.

Apollo 15 sample 15498 was collected on 1 August 1971 as unoriented float on the southern rim of Dune Crater within eastern Mare Imbrium. The rock consists of a cohesive impact melt glass matrix containing <1-mm- to ~2-cm-diameter mare basalt clasts (Fig. 1) (*33*, *34*). The clasts are petrogenetically related to the Apollo 15 quartz- and olivine-normative mare basalt suites, suggesting that the breccia was melted and assembled in close proximity to the Apollo 15 landing site (*35*). The rock is partially coated by a variably ~1- to 6-mm-thick spatter of impact melt glass (textural relationships indicate that this rind is younger than the interior breccia, but its precise age is unknown). A network of fissures lined with vesicular glass crosscuts the interior of the rock (see section S1). Although the basalt clasts contain abundant shock deformation features, including maskelynite (*33*, *34*), the lack of microfractures within the glassy matrix (see section S1) indicates that the rock has not been significantly shocked [peak pressures likely <~3 GPa (*36*)] since lithification.

The petrography and degree of crystallinity of the glassy matrix of 15498 suggest that it formed by viscous sintering of a clast-laden melt (*37*). During this primary cooling, ferromagnetic metal grains crystallized from the melt portion of the breccia. Consistent with a previous study of metal compositions in 15498 (*38*), our electron microprobe analyses found that the major ferromagnetic minerals within the resulting glass matrix are kamacite (α-$Fe_{1-x}Ni_x$ for $x < \sim 0.05$) and martensite (α_2-$Fe_{1-x}Ni_x$ for $\sim 0.05 < x < \sim 0.19$). If an ambient magnetic field was present at the time 15498 formed, kamacite and martensite grains with the observed compositions would have acquired mostly thermoremanent magnetization (TRM), with some possible contribution of thermochemical remanent magnetization (TCRM) during primary cooling on the Moon.

[1]Department of Earth, Atmospheric, and Planetary Sciences, Massachusetts Institute of Technology, 77 Massachusetts Avenue, Cambridge, MA 02139, USA. [2]Department of Earth and Planetary Science, University of California, Berkeley, Berkeley, CA 94720, USA. [3]Berkeley Geochronology Center, 2455 Ridge Road, Berkeley, CA 94709, USA. [4]Department of Earth and Planetary Sciences, Rutgers University, 610 Taylor Road, Piscataway, NJ 08854, USA.
*Corresponding author. Email: sonia.tikoo@rutgers.edu

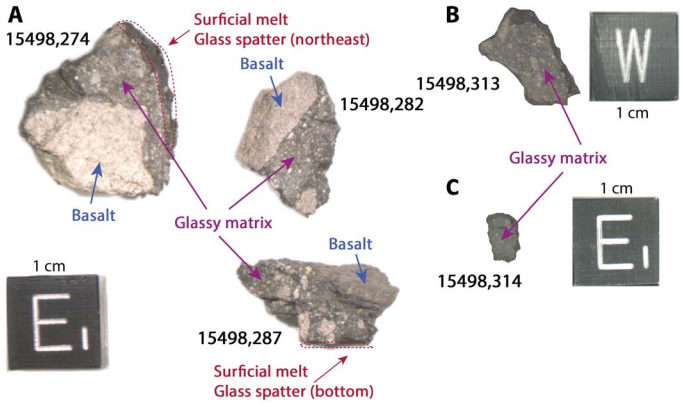

Fig. 1. Mutually oriented 15498 parent chips. (**A**) Chips 15498,274, 15498,282, and 15498,287. (**B**) Chip 15498,313. (**C**) Chip 15498,314. The sample contains abundant mare basalt fragments (blue arrows and labels) within a glassy matrix (purple arrows and labels). Surficial melt glass spatter locations are denoted with red arrows and outlines. The scale cubes have widths of 1 cm. The subsamples and scale cube are oriented following the Johnson Space Center (JSC) system for 15498.

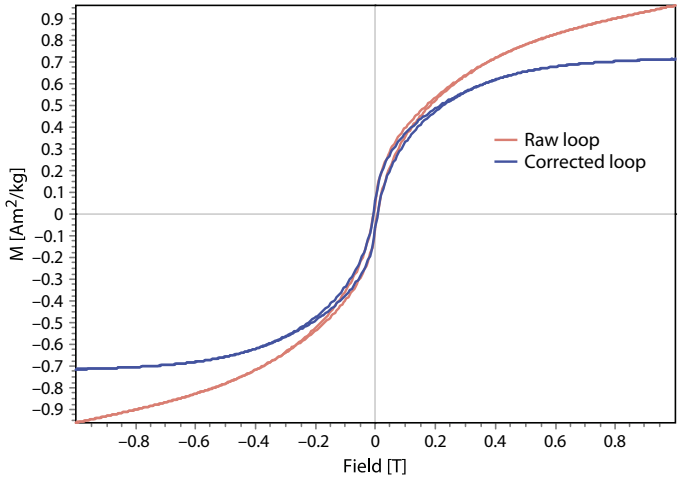

Fig. 2. Hysteresis curves for 15498. The red curve shows the measured data. The blue curve shows the data after application of a paramagnetic slope correction.

Conductive cooling calculations indicate that the glass matrix cooled from above the Curie temperature of kamacite (780°C) to ambient lunar surface temperatures (<100°C) over a period of at least a few hours (see section S1). However, this cooling time scale is long relative to the expected <1-s duration of impact fields when the rock formed. Therefore, impact fields are extremely unlikely to be the source of any TRM or TCRM acquired by the breccia's glass matrix during primary cooling.

Hysteresis data (see section S4) (*39*) and our electron microscopy imaging indicate that, in stark contrast to the multidomain grain size of metal in virtually all lunar crystalline rocks, metal within the glass matrix of 15498 is a mixture of predominantly superparamagnetic to pseudosingle domain grains, with only a relatively small contribution from multidomain grains in lithic fragments (Fig. 2). The presence of these fine-grained magnetic carriers indicates that the melt glass portion of 15498 should provide unusually high-fidelity paleomagnetic records. The relatively low Ni content of kamacite and martensite grains present within the rock suggests that the rock should retain any primary TRM and TCRM through laboratory thermal demagnetization experiments up to maximum temperatures between ~600° and 780°C [which correspond to the austenite-start solid-state phase transformation temperature for the observed martensite compositions and the kamacite Curie temperature, respectively (see section S1)]. In combination, these rock magnetic properties indicate that 15498 is an excellent target for lunar paleomagnetic studies.

A previous analysis of 15498 found that the glass matrix of the sample contained a stable natural remanent magnetization (NRM) component that persisted during alternating field (AF) demagnetization to at least 40 mT and during thermal demagnetization to at least 650°C (*39*, *40*). A paleointensity value of ~2.1 μT was obtained from one subsample (*40*) using a modified Thellier-Thellier (*41*) technique. However, this study was not able to conclusively demonstrate a robust record of the lunar dynamo due to lack of measurements of mutually oriented subsamples, checks for sample alteration during the paleointensity experiment, a detailed characterization of its postformational shock and metamorphic history, and, most importantly, a radiometric age.

RESULTS

Thermochronometry and sample age constraints

The glass matrix of 15498 should have acquired its original NRM during primary cooling. To establish the timing of this event and constrain the possibility of postformational thermal remagnetization, we conducted $^{40}Ar/^{39}Ar$ and $^{38}Ar/^{37}Ar$ thermochronometry on a whole-rock aliquot taken from the interior of a ~1-cm-diameter basalt clast from the interior of sample 15498. We obtained a minimum $^{40}Ar/^{39}Ar$ clast crystallization age of 3310 ± 24 Ma [1 SD analytical uncertainty not including uncertainties in the age of the fluence monitor and decay constant (*42*)]. This value is consistent with the crystallization ages of other studied Apollo 15 mare basalts (*43*, *44*) and is therefore likely close to the true clast crystallization age. Subsequent heating experienced by this clast due to breccia formation and daytime heating on the lunar surface triggered thermally activated diffusive loss of radiogenic ^{40}Ar. The apparent spatial distributions of radiogenic ^{40}Ar ($^{40}Ar^{*}$) and cosmogenic ^{38}Ar ($^{38}Ar_{cos}$) within clast K–rich mesostasis glass and feldspathic glass are consistent with a three-stage thermal history involving (i) clast formation at ~3.3 Ga, (ii) diffusive loss of Ar due to impact heating to peak temperatures of ~500° to ~650°C at the time of breccia lithification (occurring between ~2.5 and 1.0 Ga), and (iii) further Ar loss from daytime heating after the rock was exposed near the lunar surface at ~600 Ma [as indicated by our cosmogenic exposure age measurements (see section S5)] (Fig. 3).

Our inferred lithification age of ~2.5 to 1.0 Ga (with 1.0 Ga being our best estimate) is broadly consistent with other semiquantitative age estimates (~0.9 to 1.8 Ga) obtained from measuring trapped $^{40}Ar/^{36}Ar$ within the melt glass matrix (see section S5) (*45*). The trapped $^{40}Ar/^{36}Ar$ method aims to obtain breccia lithification model ages by measuring the ratio of lunar atmospheric ^{40}Ar to solar wind ^{36}Ar for the implanted component of Ar in the regolith. However, this method is subject to limitations associated with its primary assumptions. First, the trapped ^{40}Ar measured using this technique must have experienced a complex history of (i) formation from decay of ^{40}K in the Moon, (ii) degassing into the exosphere, and (iii) ionization and reimplantation into the lunar regolith, and assumptions are required about the efficiency of each of these processes. The method also assumes that solar wind ^{36}Ar at the Moon is constant with geological time, whereas this quantity

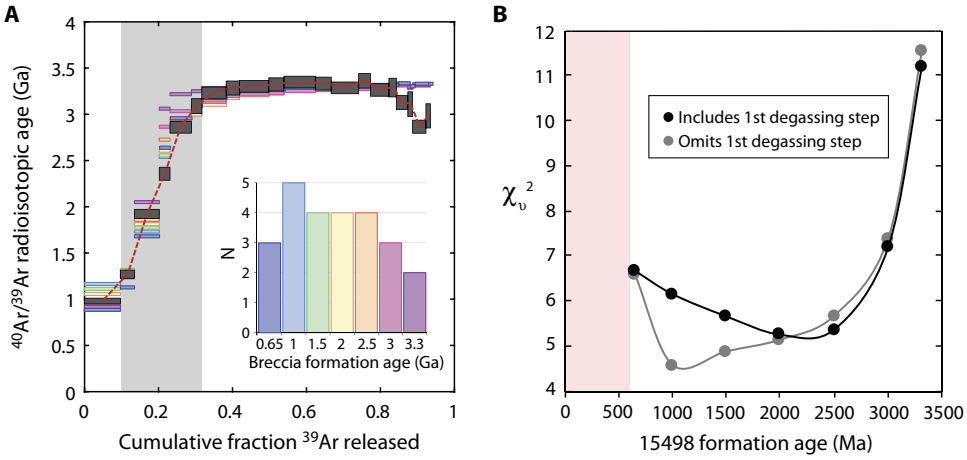

Fig. 3. ^{40}Ar/^{39}Ar thermochronometry constraints on the formation age of breccia 15498. (**A**) Multi-phase, multi-domain diffusion (MP-MDD) model predictions for diffusion of radiogenic ^{40}Ar* experienced by a 1-cm-diameter basalt clast within 15498 resulting from breccia formation between 650 and 3300 Ma (that is, from heating to temperatures ranging between 450° and 675°C), followed by daytime heating to effective mean temperatures ranging between 25° and 56°C after 600 Ma. Observed step heating ages ±1 SD (dark gray boxes) are plotted against the cumulative release fraction of ^{39}Ar released. The 3310 ± 24–Ma age inferred from the HT release steps represents the minimum crystallization age of the basalt clast. The colored steps are model release spectra calculated using MP-MDD model parameters corresponding to breccia formation at varying times (different formation ages are indicated with different colors). The inset displays the number of model degassing steps that are within error of the sample degassing path (individual steps connected by dashed red line) in the LT release fraction (heating steps 2 to 6) for different breccia formation ages (a value of $n = 5$ indicates all steps fit within error of the model). (**B**) Reduced χ^2 misfit values for model release spectra shown in (A). Misfits are shown both including (black circles) and excluding (gray circles) the first degassing step of the heating experiments. Red shaded box indicates formation ages precluded by the cosmogenic exposure age (≤600 Ma).

will actually vary depending on the strength of the lunar magnetic field (that is, its solar wind–shielding capacity) over time. Hence, this method relies on a calibration that accounts for these various factors (each subject to its own uncertainties) to relate the trapped ^{40}Ar/^{36}Ar to a lithification age in geologic time [see the studies of Fagan *et al.* (*45*) and Joy *et al.* (*46*) for further details regarding this method]. The aforementioned uncertainties in the trapped ^{40}Ar/^{36}Ar method encourage the use of an alternative chronometer to obtain complementary sample age constraints, and we were able to do so via our ^{40}Ar/^{39}Ar thermochronology modeling. In any case, we conclude that the breccia most likely formed between 1.0 and 2.5 Ga.

Paleomagnetism

To characterize the NRM in 15498, we studied 20 mutually oriented subsamples of 15498 collected from the glass matrix portions of five mutually oriented parent chips (15498,274, 15498,282, 15498,287, 15498,313, and 15498,314). Twelve subsamples were collected from the interior of 15498, and 8 subsamples were collected from near the edge of the rock (from a distance ≤~3 times the width of the young glass rind coating the sample in the vicinity of each subsample). The proximity of these peripheral subsamples to the young impact melt glass rind enables using thermal demagnetization to conduct a paleomagnetic baked contact test to determine whether the NRM of the interior subsamples predates sampling by the Apollo astronauts (*47*).

Of the 20 total subsamples, 7 subsamples were subjected to stepwise AF demagnetization (Fig. 4A). The remaining 13 subsamples were stepwise thermally demagnetized (Fig. 4B). Among the interior subsamples, we observed a low-coercivity (LC) and low-temperature (LT) magnetization component in all 12 subsamples that typically unblocked below AF levels of ≤6.5 mT and temperatures of ≤125°C, respectively. We observed a medium-coercivity (MC) and medium-temperature (MT) component in most subsamples that typically unblocked between the end of the LC/LT component and ~50 mT/~200°C (see section S2). The LC/LT and MC/MT components are largely non-unidirectional among mutually oriented subsamples (Fig. 5). The relatively low coercivities and unblocking temperatures associated with the LC/LT and MC/MT components suggest that these magnetizations likely represent viscous remanent magnetization (VRM) contamination from the terrestrial field acquired during storage and multiple stages of subdivision and handling at JSC over ≥42 years (see sections S2 and S4).

We also identified a high-coercivity (HC) and high-temperature (HT) component in all 12 interior subsamples that was blocked up to AF levels of at least 290 to 420 mT and temperatures of up to 660° to 750°C (see section S2). The HC/HT component decays linearly toward the origin (Fig. 4), suggesting that it is the characteristic magnetization component. Although there is modest dispersion (up to ~30°) in directions from individual subsamples (Fig. 6), the HC/HT components all generally cluster in the northeastern quadrant of the upper hemisphere. A Watson (*48*, *49*) statistical test for dispersion on a sphere demonstrates that the HC/HT component directions are nonrandom to 99% confidence [that is, the length of the resultant vector of our HC/HT component directions ($R = 11.5$) was greater than the critical value ($R_o = 6.55$ for 12 subsamples)] and therefore likely have a common origin. The low ratio of NRM to isothermal remanent magnetization (IRM) (≪0.1) suggests that this component was not imparted by a strong-field IRM (see section S3). The HC magnetization is unlikely to be a shock remanent magnetization (SRM), given that SRM acquired at pressures of <3 GPa is typically acquired by low-coercivity grains (see section S4) (*50*, *51*). Because single-domain kamacite grains (which dominantly carry the remanence in 15498) should not retain a terrestrial VRM after laboratory heating to temperatures above ~125°C (*52*), the persistence of the HT component to temperatures ≥660°C precludes its origin as a VRM. Crystallization remanent magnetization (CRM) is also excluded because the metal grains are in the form of primary low-Ni kamacite and martensite (and have not recrystallized to plessite or to Widmanstätten taenite and kamacite).

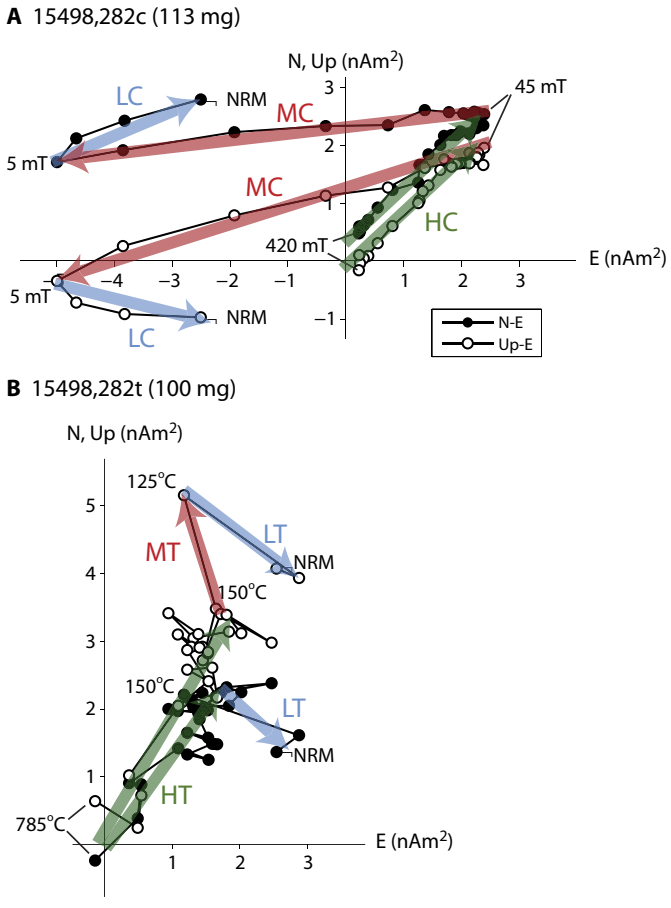

Fig. 4. Vector endpoint diagrams showing demagnetization of 15498 subsamples. (**A**) AF demagnetization of subsample 282c. (**B**) Thermal demagnetization of subsample 282t. Open and closed circles represent projections of the NRM vector onto the vertical (Up-E) and horizontal planes (N-E), respectively. Blue, red, and green arrows denote LC/LT, MC/MT, and HC/HT components, respectively. Subsample masses as well as selected AF levels and temperature steps are labeled.

We obtained high-quality Thellier-Thellier paleointensity values of 5 ± 2 μT (mean ± 1σ) from the HT components of six of the interior subsamples (Fig. 7). These values are broadly consistent with our anhysteretic remanent magnetization (ARM) and IRM paleointensity measurements on the HC components of four AF-demagnetized subsamples, which yielded values ranging between ~600 nT and ~2 μT [within the factor 2 to 5 uncertainties on the latter values (*6*)]. It is conceivable that the remanence being carried is not purely TRM and that some martensite may have acquired TCRM upon formation. However, if the NRM of 15498 is a TCRM, the paleointensities inferred from our Thellier experiments would likely represent lower limits due to the inefficiency of CRM relative to TRM (*53*). Regardless, paleointensities derived from TCRM are usually within several tens of percent of the actual value (*54*). Therefore, we suspect that our paleointensity results are reasonably accurate even if the remanence is not a pure TRM.

In contrast, four of the five thermally demagnetized peripheral subsamples taken from near the young melt glass rind were fully demagnetized by 360°C, and two of the three AF-demagnetized peripheral subsamples were fully demagnetized by ac fields of 20 mT. The only subsample that contained a magnetization component with the same direction as the HC/HT component observed within the interior subsamples was the subsample collected the farthest away (0.7 cm) from the melt glass rind (274v3). Furthermore, the inferred NRM intensities of these subsamples are, on average, ~90% lower than those of the interior subsamples (see Fig. 8 and section S2). The general absence of HC and HT magnetization within peripheral subsamples suggests that they were thermally demagnetized on the Moon when the impact melt glass was emplaced on the surface of the rock. Collectively, these data are consistent with a positive baked contact test for 15498 and indicate that the HC/HT component observed in the interior subsamples is very likely a TRM acquired during primary cooling in the presence of a temporally stable ambient field on the Moon.

DISCUSSION

The ~5-μT paleointensities obtained from the melt glass matrix of 15498 are ~1000 times stronger than the field measured by astronauts

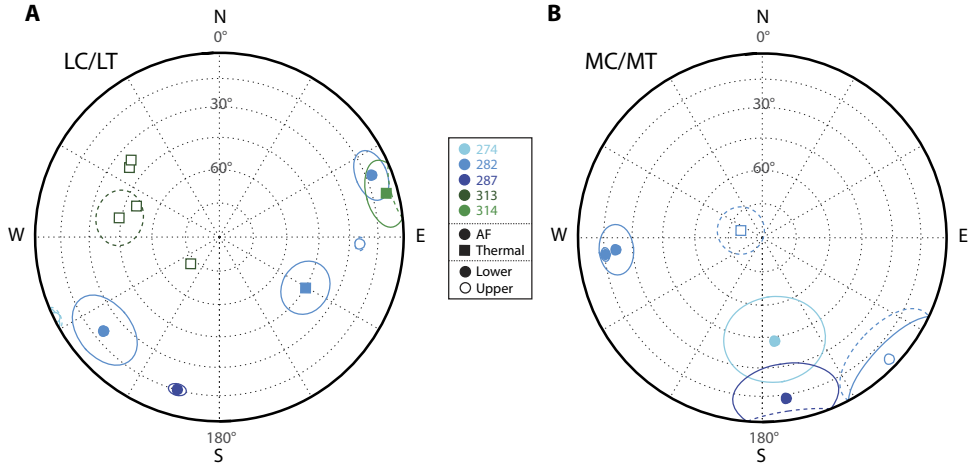

Fig. 5. Equal-area stereographic projections of LC/LT and MC/MT magnetization components observed for interior subsamples of 15498. (**A**) LC (circles) and LT (squares) component directions. (**B**) MC (circles) and MT (squares) component directions. Lines encircling component directions represent the maximum angular deviations associated with each direction. Open symbols (dashed lines) represent directions in the upper hemisphere, whereas filled symbols (solid lines) represent directions in the lower hemisphere. Subsamples from parent chips 274, 282, 287, 313, and 314 are denoted with light blue, medium blue, dark blue, dark green, and light green symbols, respectively.

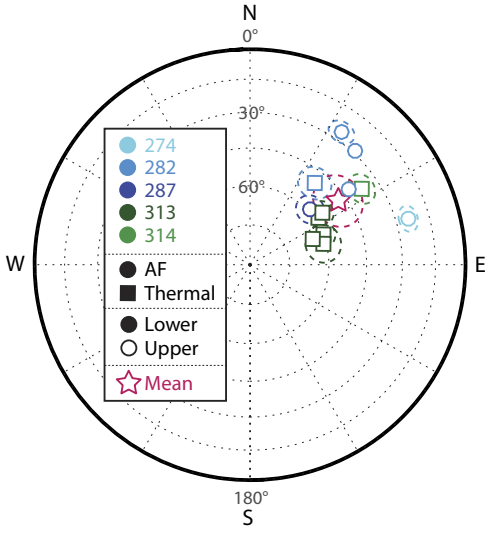

Fig. 6. Equal-area stereographic projection of HC and HT magnetization component directions. Shown directions are observed for mutually oriented matrix glass subsamples from the interior of 15498. Symbols and surrounding ellipses represent directions and associated maximum angular deviation values obtained from principal component analysis. AF and thermally demagnetized subsamples are displayed using circles and squares, respectively. Subsamples from parent chips 274, 282, 287, 313, and 314 are shown by light blue, medium blue, dark blue, dark green, and light green symbols, respectively. Open symbols (dashed lines) represent directions in the upper hemisphere, and filled symbols (solid lines) represent directions in the lower hemisphere. The Fisher mean direction and α_{95} confidence interval (star and surrounding ellipse, respectively) are shown.

at the Apollo 15 site (*55*), ~10 times stronger than the largest remanent crustal fields measured at any lunar landing site (Apollo 16), and several orders of magnitude greater than external field sources like the Earth, Sun, and galactic magnetic fields (*55*). The most likely mechanisms capable of generating ~5-μT fields at the lunar surface at 1 to 2.5 Ga are impact fields and a core dynamo. Because the slow primary cooling time scale of 15498 excludes an impact field origin for the observed TRM, our data strongly indicate that the glass matrix portion of 15498 preserves a dynamo record.

Our data indicate that the lunar core dynamo persisted until at least ~1.0 to ~2.5 Ga, thereby extending the known lifetime of the dynamo by ~1.0 billion to ~2.5 billion years [from the previous youngest dynamo record observed in 3.56-Ga mare basalts (*5*)]. Exactly when the lunar dynamo ceased remains unclear. Given the expected geophysical properties of the lunar interior, no current dynamo scenarios powered by large impacts or purely thermal convection predict that the magnetic field could persist this late in lunar history. Thermal evolution models suggest that thermochemical convection produced by core crystallization could generate a ~1-μT dynamo field that persisted (either continuously or in an intermittent "start-stop" regime) beyond ~1.6 Ga (*24*, *26*). However, according to current scaling laws for convective dynamos, thermochemical convection alone may not be able to reproduce the high ~20- to ~110-μT surface fields inferred for Apollo samples aged 4.25 to 3.56 Ga (*6*). In contrast, a precession dynamo may be capable of generating ~10- to ~100-μT fields for the period before 3.56 Ga (*15*, *16*), but persistence of such a dynamo beyond ~2 Ga would likely require that the Moon's orbit receded from the Earth at a rate far slower than expected (*6*, *8*). Given these constraints, no single dynamo generation mechanism proposed thus far can readily reproduce the paleointensity record inferred from Apollo samples. One possible solution is that the dynamo may have been powered by at least two distinct mechanisms operating during early and late lunar history. A second possible solution

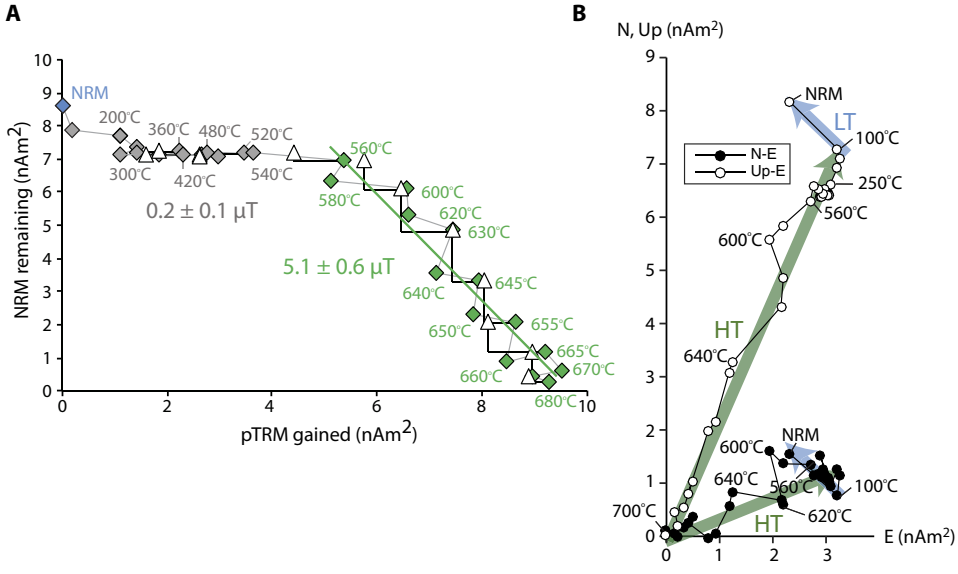

Fig. 7. Thellier-Thellier paleointensity experiment for subsample 15498,313e. (**A**) Arai plot displaying NRM lost during progressive thermal demagnetization (ordinate) versus laboratory pTRM gained (abscissa). Peak temperatures for selected steps are shown. pTRM checks for alteration are shown as triangles. Paleointensities for unblocking temperature ranges of 250° to 540°C and 560° to 680°C are denoted with dark gray and green symbols, respectively. Gray segments link consecutive thermal steps. (**B**) Vector endpoint diagram showing zero-field thermal demagnetization steps for subsample 313e. LT and HT components are denoted using blue and green symbols, respectively. Paleointensity experiments were conducted following the IZZI protocol (alternating zero-field and in-field measurements).

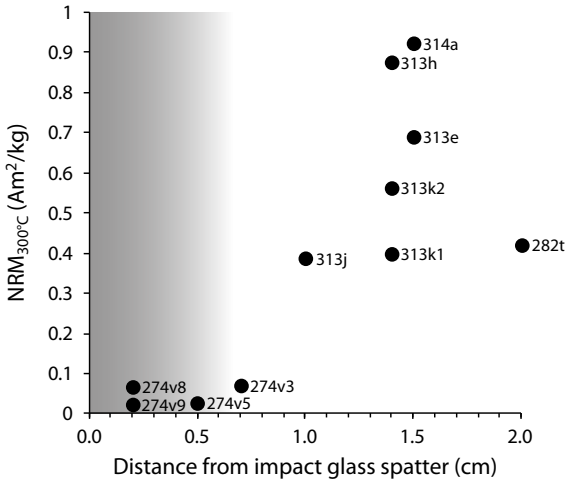

Fig. 8. Magnetization versus distance from the peripheral impact glass spatter. Shown are residual magnetization values for thermally demagnetized 15498 matrix glass subsamples after heating to 300°C. Individual subsample names are labeled. The gray shaded box denotes the zone likely to have been remagnetized by emplacement of the impact glass spatter (approximately three half-widths of the local glass spatter thickness).

is that dynamo was powered by a single bistable mechanism that transitioned from a strong-dipole dominated state to a weaker multipolar state after 3.56 Ga (*56*).

METHODS

Paleomagnetic and rock magnetic analyses

All paleomagnetic measurements were conducted using a 2G Enterprises Superconducting Rock Magnetometer 755 located within a magnetically shielded room (ambient field of <200 nT) in the Massachusetts Institute of Technology (MIT) Paleomagnetism Laboratory. The magnetometer is equipped with automated AF demagnetization, sample handling, and rock magnetic remanence characterization capabilities (*57*). Purely nondestructive static three-axis AF demagnetization experiments were conducted on 7 of the 20 total subsamples up to peak ac fields of at least 290 mT. Purely thermal demagnetization was conducted on nine subsamples up to maximum temperatures of 660° to 700°C, or until samples were fully demagnetized, in a new controlled oxygen fugacity oven (*58*). Thermal experiments were conducted in an H_2-CO_2 atmosphere at 1 log unit below the iron-wüstite buffer. The four remaining subsamples were AF-pretreated up to peak ac fields of 35 mT and then thermally demagnetized. The subsamples were measured in differing orientations, and the demagnetization data were subsequently rotated into a mutually oriented reference frame for analysis. Principal component analysis was used to determine the best-fit directions for all observed magnetization components (*59*). Thellier-Thellier paleointensity experiments were conducted on six of the thermal demagnetization subsamples following the IZZI (in-field, zero-field, zero-field, in-field) protocol (*60*), including partial TRM (pTRM) checks for alteration. ARM and/or IRM paleointensities (*2*, *5*, *61*) were determined for four subsamples. Full details of the demagnetization and paleointensity experiments are provided in section S3. Remanence-based rock magnetic experiments (for example, ARM and IRM acquisition and demagnetization) were conducted at MIT. Hysteresis and first-order reversal curve (FORC) measurements were conducted using a vibrating sample magnetometer at the Institute for Rock Magnetism at the University of Minnesota (see section S4).

$^{40}Ar/^{39}Ar$ and $^{38}Ar/^{37}Ar$ thermochronology

All $^{40}Ar/^{39}Ar$ and $^{38}Ar/^{37}Ar$ thermochronometry experiments were conducted at the Berkeley Geochronology Center. Using the procedures described in previous works (*4*, *5*, *62*), we conducted stepwise degassing $^{40}Ar/^{39}Ar$ and $^{38}Ar/^{37}Ar$ experiments on one (~2 mg) whole-rock aliquot of a basalt clast (referred to as 282-1 herein) located adjacent to the glass matrix portion of parent chip 15498,282 that we used for paleomagnetic analyses. Additional stepwise degassing experiments conducted on two whole-rock aliquots of matrix glass yielded complex, discordant age spectra from which no plateau age could be inferred due to the presence of excess nonradiogenic (trapped) ^{40}Ar and solar wind ^{36}Ar. This degassing behavior has been observed for many other lunar impact glasses and regoliths (*63*). Because it was not possible to directly obtain ages for the matrix glass samples, we do not discuss these experiments further. Apparent $^{40}Ar/^{39}Ar$ ages for each degassing step were calculated relative to the Hb3gr fluence monitor [age, 1081 Ma (*42*)] using the decay constants of Renne *et al.* (*42*) and the isotopic abundances of Steiger and Jäger (*64*). We also determined apparent cosmogenic ^{38}Ar exposure ages for each degassing step following procedures described in previous works (*4*, *5*, *65*). Following Shea *et al.* (*4*), we constructed multi-phase, multi-diffusion domain (MP-MDD) model fits to the $^{40}Ar/^{39}Ar$ age spectrum and the cosmogenic ^{38}Ar age spectrum to quantify the diffusion of radiogenic ^{40}Ar ($^{40}Ar^*$) and cosmogenic ^{38}Ar ($^{38}Ar_{cos}$) in our sample in the context of various possible thermal histories. All modeled thermal histories include (i) the initial formation of the basalt clast, (ii) diffusive loss of Ar due to impact heating at the time of breccia lithification, and (iii) further loss of Ar from daytime heating while the rock was exposed near the lunar surface before its collection. Full details regarding our MP-MDD models are given in section S5.

SUPPLEMENTARY MATERIALS

Supplementary material for this article is available at http://advances.sciencemag.org/cgi/content/full/3/8/e1700207/DC1

section S1. Sample 15498
section S2. NRM behavior
section S3. Paleointensity
section S4. Rock magnetic properties
section S5. $^{40}Ar/^{39}Ar$ and $^{38}Ar/^{37}Ar$ thermochronology
fig. S1. Apollo 15 landing site and 15498 sampling context.
fig. S2. Sample 15498.
fig. S3. Backscattered scanning electron microscopy images of 15498 matrix showing absence of post-lithification microfracturing.
fig. S4. BSEM images of FeNi grains in 15498.
fig. S5. Equal-area stereographic projections of LC/LT and MC/MT magnetization components observed for peripheral subsamples of 15498.
fig. S6. AF demagnetization of sample 15498,282a over the range of the HC component.
fig. S7. Thellier-Thellier paleointensity experiments for subsamples 15498,313k1 and 15498,313k2 following the IZZI variant.
fig. S8. Paleointensity fidelity limit tests for 15498.
fig. S9. FORC distribution for sample 15498,287b1.
fig. S10. Rock magnetic experiments on 15498,282a.
fig. S11. PRM acquisition by 15498 subsample 15498,282a.
fig. S12. VRM decay experiment on sample 15498,282c.
fig. S13. The predicted effects of 600 Ma of solar heating at the lunar surface, calculated using the 15498 MP-MDD model.
fig. S14. Arrhenius plots with calculated diffusion coefficients for ^{39}Ar and ^{37}Ar released during the first 20 release steps.
fig. S15. Schematic depicting time-temperature conditions underlying our thermochronological models.
fig. S16. 15498 MP-MDD model predictions for diffusion of $^{40}Ar^*$ resulting from impact heating at 2000 Ma (to temperatures ranging between 450° and 675°C), followed by daytime heating to an effective mean temperature of 69°C after 600 Ma.

fig. S17. 15498 MP-MDD model predictions for diffusion of $^{40}Ar^*$ resulting from impact heating at various times in lunar history (to temperatures ranging between 450° and 675°C), followed by daytime heating to effective mean temperatures ranging between 35° and 56°C after 600 Ma.
fig. S18. 15498 MP-MDD model age spectra incorporating diffusion of $^{40}Ar^*$ resulting from impact heating at 650 Ma (to temperatures ranging between 450° and 675°C), followed by daytime heating to an effective mean temperature of 25°C after 600 Ma.
table S1. WDS measurements of metal grains in 15498 thin sections 298 and 299.
table S2A. NRM components identified for interior matrix glass subsamples of 15498.
table S2B. NRM components identified for peripheral matrix glass subsamples of 15498.
table S2C. Fisher mean component directions derived from 15498 data in table S2A.
table S3A. Thellier-Thellier paleointensity determinations for 15498 subsamples.
table S3B. Comparison of pTRM and pTRM check values for 15498 subsamples.
table S3C. ARM paleointensity determinations for 15498 subsamples.
table S3D. IRM paleointensity determinations for 15498 subsamples.
table S4. Rock magnetic and hysteresis parameters.
table S5. Anisotropy of ARM (85-mT ac field with 0.01-mT dc field).
table S6. Complete $^{40}Ar/^{39}Ar$ incremental heating results.
table S7. Oxide weight percent compositions of K-bearing phases in basalt clast 15498-282-1.
table S8. Summary of MP-MDD model parameters with cosmogenic ^{38}Ar production rates for 15498.
table S9. Summary of $^{40}Ar/^{39}Ar$ chronology for 15498.
table S10. Reduced χ^2 misfit statistics for best-fit thermochronometry models for a variety of breccia formation ages.
data file S1. 15498 demagnetization data sets.
data file S2. 15498 Thellier-Thellier paleointensity data sets.
References (*66*–*125*)

REFERENCES AND NOTES

1. C. Cournède, J. Gattacceca, P. Rochette, Magnetic study of large Apollo samples: Possible evidence for an ancient centered dipolar field on the Moon. *Earth Planet. Sci. Lett.* **331–332**, 31–42 (2012).
2. I. Garrick-Bethell, B. P. Weiss, D. L. Shuster, J. Buz, Early lunar magnetism. *Science* **323**, 356–359 (2009).
3. L. L. Hood, Central magnetic anomalies of Nectarian-aged lunar impact basins: Probable evidence for an early core dynamo. *Icarus* **211**, 1109–1128 (2011).
4. E. K. Shea, B. P. Weiss, W. S. Cassata, D. L. Shuster, S. M. Tikoo, J. Gattacceca, T. L. Grove, M. D. Fuller, A long-lived lunar core dynamo. *Science* **335**, 453–456 (2012).
5. C. Suavet, B. P. Weiss, W. S. Cassata, D. L. Shuster, J. Gattacceca, L. Chan, I. Garrick-Bethell, J. W. Head, T. L. Grove, M. D. Fuller, Persistence and origin of the lunar core dynamo. *Proc. Natl. Acad. Sci. U.S.A.* **110**, 8453–8458 (2013).
6. B. P. Weiss, S. M. Tikoo, The lunar dynamo. *Science* **346**, 1246753 (2014).
7. K. Lawrence, C. Johnson, L. Tauxe, J. Gee, Lunar paleointensity measurements: Implications for lunar magnetic evolution. *Phys. Earth Planet. Inter.* **168**, 71–87 (2008).
8. S. M. Tikoo, B. P. Weiss, W. S. Cassata, D. L. Shuster, J. Gattacceca, E. A. Lima, C. Suavet, F. Nimmo, M. D. Fuller, Decline of the lunar core dynamo. *Earth Planet. Sci. Lett.* **404**, 89–97 (2014).
9. M. Fuller, Lunar magnetism—A retrospective view of the Apollo sample magnetic studies. *Phys. Chem. Earth* **23**, 725–735 (1998).
10. A. J. Evans, M. T. Zuber, B. P. Weiss, S. M. Tikoo, A wet, heterogeneous lunar interior: Lower mantle and core dynamo evolution. *J. Geophys. Res.* **119**, 1061–1077 (2014).
11. W. Konrad, T. Spohn, Thermal history of the Moon: Implications for an early core dynamo and post-accertional magmatism. *Adv. Space Res.* **19**, 1511–1521 (1997).
12. M. Laneuville, M. A. Wieczorek, D. Breuer, N. Tosi, Asymmetric thermal evolution of the Moon. *J. Geophys. Res.* **118**, 1435–1452 (2013).
13. D. R. Stegman, A. M. Jellinek, S. A. Zatman, J. R. Baumgardner, M. A. Richards, An early lunar core dynamo driven by thermochemical mantle convection. *Nature* **421**, 143–146 (2003).
14. M. Le Bars, M. A. Wieczorek, Ö. Karatekin, D. Cébron, M. Laneuville, An impact-driven dynamo for the early Moon. *Nature* **479**, 215–218 (2011).
15. C. A. Dwyer, D. J. Stevenson, F. Nimmo, A long-lived lunar dynamo driven by continuous mechanical stirring. *Nature* **479**, 212–214 (2011).
16. S. Stanley, B. Y. Tian, B. P. Weiss, S. M. Tikoo, The ancient lunar dynamo: How to resolve the intensity and duration conundrums. *Proc. Lunar Planet. Sci. Conf.* **48**, 1462 (2017).
17. R. C. Weber, P.-Y. Lin, E. J. Garnero, Q. Williams, P. Lognonne, Seismic detection of the lunar core. *Science* **331**, 309–312 (2011).
18. J. G. Williams, A. S. Konopliv, D. H. Boggs, R. S. Park, D.-N. Yuan, F. G. Lemoine, S. Goossens, E. Mazarico, F. Nimmo, R. C. Weber, S. W. Asmar, H. J. Melosh, G. A. Neumann, R. J. Phillips, D. E. Smith, S. C. Solomon, M. M. Watkins, M. A. Wieczorek, J. C. Andrews-Hanna, J. W. Head, W. S. Kiefer, I. Matsuyama, P. J. McGovern, G. J. Taylor, M. T. Zuber, Lunar interior properties from the GRAIL mission. *J. Geophys. Res.* **119**, 1546–1578 (2014).
19. R. F. Garcia, J. Gagnepain-Beyneix, S. Chevrot, P. Lognonné, Very preliminary reference Moon model. *Phys. Earth Planet. Inter.* **188**, 96–113 (2011).
20. L. L. Hood, D. L. Mitchell, R. P. Lin, M. H. Acuna, A. B. Binder, Initial measurements of the lunar induced magnetic dipole moment using Lunar Prospector Magnetometer data. *Geophys. Res. Lett.* **26**, 2327–2330 (1999).
21. Z. Jing, Y. Wang, Y. Kono, T. Yu, T. Sakamaki, C. Park, M. L. Rivers, S. R. Sutton, G. Shen, Sound velocity of Fe–S liquids at high pressure: Implications for the Moon's molten outer core. *Earth Planet. Sci. Lett.* **396**, 78–87 (2014).
22. A. S. Konopliv, A. B. Binder, L. L. Hood, A. B. Kucinskas, W. L. Sjogren, J. G. Williams, Improved gravity field of the moon from lunar prospector. *Science* **281**, 1476–1480 (1998).
23. H. Shimizu, F. Matsushima, F. Takahashi, H. Shibuya, H. Tsunakawa, Constraint on the lunar core size from electromagnetic sounding based on magnetic field observations by an orbiting satellite. *Icarus* **222**, 32–43 (2013).
24. M. Laneuville, M. A. Wieczorek, D. Breuer, J. Aubert, G. Morard, T. Rückriemen, A long-lived lunar dynamo powered by core crystallization. *Earth Planet. Sci. Lett.* **401**, 251–260 (2014).
25. N. Zhang, E. M. Parmentier, Y. Liang, A 3-D numerical study of the thermal evolution of the Moon after cumulate mantle overturn: The importance of rheology and core solidification. *J. Geophys. Res.* **118**, 1789–1804 (2013).
26. A. Scheinberg, K. M. Soderlund, G. Schubert, Magnetic field generation in the lunar core: The role of inner core growth. *Icarus* **254**, 62–71 (2015).
27. S. M. Tikoo, B. P. Weiss, J. Buz, E. A. Lima, E. K. Shea, G. Melo, T. L. Grove, Magnetic fidelity of lunar samples and implications for an ancient core dynamo. *Earth Planet. Sci. Lett.* **337–338**, 93–103 (2012).
28. M. A. Wieczorek, B. L. Jolliff, A. Khan, M. E. Pritchard, B. P. Weiss, J. G. Williams, L. L. Hood, K. Righter, C. R. Neal, C. K. Shearer, I. S. McCallum, S. Tompkins, B. R. Hawke, C. Peterson, J. J. Gillis, B. Bussey, The constitution and structure of the lunar interior. *Rev. Mineral. Geochem.* **60**, 221–364 (2006).
29. J. Buz, B. P. Weiss, S. M. Tikoo, D. L. Shuster, J. Gattacceca, T. L. Grove, Magnetism of a very young lunar glass. *J. Geophys. Res.* **120**, 1720–1735 (2015).
30. L. L. Hood, N. A. Artemieva, Antipodal effects of lunar basin-forming impacts: Initial 3D simulations and comparisons with observations. *Icarus* **193**, 485–502 (2008).
31. D. A. Crawford, P. H. Schultz, Electromagnetic properties of impact-generated plasma, vapor and debris. *Int. J. Impact Eng.* **23**, 169–180 (1999).
32. L. J. Srnka, Spontaneous magnetic field generation in hypervelocity impacts. *Proc. Lunar Planet. Sci. Conf.* **8**, 785–792 (1977).
33. B. Mason, Mineralogy and petrology of polymict breccia 15498, in *The Apollo 15 Lunar Samples* (The Lunar Science Institute, 1972), pp. 137–139.
34. G. Ryder, Ed., *Catalog of Apollo 15 Rocks* (NASA Curatorial Branch, 1985), vol. 72.
35. S. K. Vetter, J. W. Shervais, M. M. Lindstrom, Petrology and geochemistry of olivine-normative and quartz-normative basalts from regolith breccia 15498: New diversity in Apollo 15 mare basalts. *Proc. Lunar Planet. Sci. Conf.* **18**, 255–271 (1988).
36. P. Lambert, Fractures induced by shock in quartz and feldspar. *Mineral. Mag.* **43**, 527–533 (1979).
37. D. R. Uhlmann, L. C. Klein, Crystallization kinetics, viscous flow and thermal histories of lunar breccias 15286 and 15498. *Proc. Lunar Planet. Sci. Conf.* **7**, 2529–2541 (1976).
38. G. W. Pearce, G. S. Hoye, D. W. Strangway, B. M. Walker, L. A. Taylor, Some complexities in the determination of lunar paleointensities. *Proc. Lunar Planet. Sci. Conf.* **7**, 3271–3297 (1976).
39. W. A. Gose, G. W. Pearce, D. W. Strangway, J. Carnes, Magnetism of Apollo 15 samples, in *The Apollo 15 Lunar Samples* (The Lunar Science Institute, 1972), pp. 430–434.
40. W. A. Gose, D. W. Strangway, G. W. Pearce, A determination of the intensity of the ancient lunar magnetic field. *The Moon* **7**, 196–201 (1973).
41. E. Thellier, O. Thellier, Sur l'intensité du champ magnétique terrestre dans le passé historique et géologique. *Ann. Geophys.* **15**, 285–376 (1959).
42. P. R. Renne, G. Balco, K. R. Ludwig, R. Mundil, K. Min, Response to the comment by W.H. Schwarz et al. on "Joint determination of ^{40}K decay constants and $^{40}Ar^*/^{40}K$ for the Fish Canyon sanidine standard, and improved accuracy for $^{40}Ar/^{39}Ar$ geochronology" by P.R. Renne et al. (2010). *Geochim. Cosmochim. Acta* **75**, 5097–5100 (2011).
43. D. L. Shuster, W. S. Cassata, Paleotemperatures at the lunar surfaces from open system behavior of cosmogenic ^{38}Ar and radiogenic ^{40}Ar. *Geochim. Cosmochim. Acta* **155**, 154–171 (2015).
44. D. Stöffler, G. Ryder, B. A. Ivanov, N. A. Artemieva, M. J. Cintala, R. A. F. Grieve, Cratering history and lunar chronology. *Rev. Mineral. Geochem.* **60**, 519–596 (2006).
45. A. L. Fagan, K. H. Joy, D. D. Bogard, D. A. Kring, Ages of globally distributed lunar paleoregoliths and soils from 3.9 Ga to the present. *Earth Moon Planets* **112**, 59–71 (2014).
46. K. H. Joy, D. A. Kring, D. D. Bogard, D. S. McKay, M. E. Zolensky, Re-examination of the formation ages of the Apollo16 regolith breccias. *Geochim. Cosmochim. Acta* **75**, 7208–7225 (2011).

47. C. W. F. Everitt, J. A. Clegg, A field test of palaeomagnetic stability. *Geophys. J. Int.* **6**, 312–319 (1962).
48. G. S. Watson, Analysis of dispersion on a sphere. *Geophys. J. Roy. Astron. Soc.* **7**, 153–159 (1956).
49. G. S. Watson, A test for randomness of directions. *Geophys. J. Roy. Astron. Soc.* **7**, 160–161 (1956).
50. J. Gattacceca, M. Boustie, L. Hood, J.-P. Cuq-Lelandais, M. Fuller, N. S. Bezaeva, T. de Resseguier, L. Berthe, Can the lunar crust be magnetized by shock: Experimental groundtruth. *Earth Planet. Sci. Lett.* **299**, 42–53 (2010).
51. S. M. Tikoo, J. Gattacceca, N. L. Swanson-Hysell, B. P. Weiss, C. Suavet, C. Cournède, Preservation and detectability of shock-induced magnetization. *J. Geophys. Res.* **120**, 1461–1475 (2015).
52. I. Garrick-Bethell, B. P. Weiss, Kamacite blocking temperatures and applications to lunar magnetism. *Earth Planet. Sci. Lett.* **294**, 1–7 (2010).
53. D. J. Dunlop, K. S. Argyle, Thermoremanence, anhysteretic remanence and susceptibility of submicron magnetites: Nonlinear field dependence and variation with grain size. *J. Geophys. Res.* **102**, 20199–20210 (1997).
54. K. Fabian, Thermochemical remanence acquisition in single-domain particle ensembles: A case for possible overestimation of the geomagnetic paleointensity. *Geochem. Geophys. Geosyst.* **10**, Q06Z03 (2009).
55. P. Dyal, C. W. Parkin, W. D. Daily, Magnetism and the interior of the moon. *Rev. Geophys. Space Phys.* **12**, 568–591 (1974).
56. T. Gastine, L. Duarte, J. Wicht, Dipolar versus multipolar dynamos: The influence of the background density stratification. *Astron. Astrophys.* **546**, A19 (2012).
57. J. L. Kirschvink, R. E. Kopp, T. D. Raub, C. T. Baumgartner, J. W. Holt, Rapid, precise, and high-sensitivity acquisition of paleomagnetic and rock-magnetic data: Development of a low-noise automatic sample changing system for superconducting rock magnetometers. *Geochem. Geophys. Geosyst.* **9**, Q05Y01 (2008).
58. C. Suavet, B. P. Weiss, T. L. Grove, Controlled-atmosphere thermal demagnetization and paleointensity analyses of extraterrestrial rocks. *Geochem. Geophys. Geosyst.* **15**, 2733–2743 (2014).
59. J. L. Kirschvink, The least-squares line and plane and the analysis of palaeomagnetic data. *Geophys. J. Roy. Astron. Soc.* **62**, 699–718 (1980).
60. L. Tauxe, H. Staudigel, Strength of the geomagnetic field in the Cretaceous Normal Superchron: New data from submarine basaltic glass of the Troodos Ophiolite. *Geochem. Geophys. Geosyst.* **5**, Q02H06 (2004).
61. Y. Yu, Paleointensity determination using anhysteretic remanence and saturation isothermal remanence. *Geochem. Geophys. Geosyst.* **11**, Q02Z12 (2010).
62. W. S. Cassata, P. R. Renne, D. L. Shuster, Argon diffusion in plagioclase and implications for thermochronometry: A case study from the Bushveld Complex, South Africa. *Geochim. Cosmochim. Acta* **73**, 6600–6612 (2009).
63. L. Husain, ^{40}Ar-^{39}Ar chronology and cosmic ray exposure ages of the Apollo 15 samples. *J. Geophys. Res.* **79**, 2588–2606 (1974).
64. R. H. Steiger, E. Jäger, Subcommission on geochronology: Convention on the use of decay constants in geo- and cosmochronology. *Earth Planet. Sci. Lett.* **36**, 359–362 (1977).
65. W. S. Cassata, D. L. Shuster, P. R. Renne, B. P. Weiss, Evidence for shock heating and constraints on Martian surface temperatures revealed by ^{40}Ar/^{39} Ar thermochronometry of Martian meteorites. *Geochim. Cosmochim. Acta* **74**, 6900–6920 (2010).
66. D. R. Scott, A. F. Worden, J. B. Irwin, Crew observations, in *Apollo 15 Preliminary Science Report*, J. P. Allen, Ed. (National Aeronautics and Space Administration, 1972).
67. D. B. J. Bussey, P. D. Spudis, B. R. Hawke, P. G. Lucey, G. J. Taylor, Geology and composition of the Apennine mountains, lunar Imbrium basin. *Proc. Lunar Planet. Sci. Conf.* **29**, 1352 (1998).
68. P. D. Spudis, G. A. Swann, R. Greeley, The formation of Hadley Rille and implications for the geology of the Apollo 15 region. *Proc. Lunar Planet. Sci. Conf.* **18**, 243–254 (1988).
69. B. W. Chappell, D. H. Green, Chemical compositions and petrogenetic relationships in Apollo 15 mare basalts. *Earth Planet. Sci. Lett.* **18**, 237–246 (1973).
70. E. Dowty, M. Prinz, K. Keil, Composition, mineralogy, and petrology of 28 mare basalts from Apollo 15 rake samples. *Proc. Lunar Planet. Sci. Conf.* **4**, 423 (1973).
71. P. A. Helmke, D. P. Blanchard, L. A. Haskin, K. M. Telander, C. K. Weiss, J. W. Jacobs, Major and trace elements in crystaline rocks from Apollo 15. *Proc. Lunar Planet. Sci. Conf.* **4**, 349 (1973).
72. J. M. Rhodes, Major element chemistry of Apollo 15 mare basalts, in *The Apollo 15 Lunar Samples* (The Lunar Science Institute, 1972), pp. 250–252.
73. J. M. Rhodes, N. J. Hubbard, Chemistry, classification, and petrogenesis of Apollo 15 mare basalts. *Proc. Lunar Planet. Sci. Conf.* **4**, 1127–1148 (1973).
74. P. D. Spudis, G. Ryder, Geology and petrology of the Apollo 15 landing site: Past, present, and future understanding. *Eos. Trans. AGU* **66**, 721–726 (1985).
75. A. R. Duncan, M. K. Sher, Y. C. Abraham, A. J. Erlank, J. P. Willis, L. H. Ahrens, Interpretation of the compositional variability of Apollo 15 soils. *Proc. Lunar Planet. Sci. Conf.* **6**, 2309–2320 (1975).
76. G. Ryder, D. Bogard, D. Garrison, Probable age of Autolycus and calibration of lunar stratigraphy . *Geology* **19**, 143–146 (1991).
77. T. S. Culler, T. A. Becker, R. A. Muller, P. R. Renne, Lunar impact history from ^{40}Ar/^{39}Ar dating of glass spherules. *Science* **287**, 1785–1788 (2000).
78. B. R. Hawke, D. T. Blewett, P. G. Lucey, G. A. Smith, J. F. Bell, B. A. Campbell, M. S. Robinson, The origin of lunar crater rays. *Icarus* **170**, 1–16 (2004).
79. C. H. Simonds, Thermal regimes in impact melts and the petrology of the Apollo 17 Station 6 boulder. *Proc. Lunar Planet. Sci. Conf.* **6**, 641–672 (1975).
80. J. Gattacceca, L. Berthe, M. Boustie, F. Vadeboin, P. Rochette, T. De Resseguier, On the efficiency of shock magnetization processes. *Phys. Earth Planet. Inter.* **166**, 1–10 (2008).
81. T. Nagata, Introductory notes on shock remanent magnetization and shock demagnetization of igneous rocks. *Pure Appl. Geophys.* **89**, 159–177 (1971).
82. J. Pohl, U. Bleil, U. Hornemann, Shock magnetization and demagnetization of basalt by transient stress up to 10 kbar. *J. Geophys.* **41**, 23–41 (1975).
83. N. S. Bezaeva, J. Gattacceca, P. Rochette, R. A. Sadykov, V. I. Trukhin, Demagnetization of terrestrial and extraterrestrial rocks under hydrostatic pressure up to 1.2 GPa. *Phys. Earth Planet. Inter.* **179**, 7–20 (2010).
84. J. Gattacceca, M. Boustie, E. Lima, B. P. Weiss, T. de Resseguier, J. P. Cuq-Lelandais, Unraveling the simultaneous shock magnetization and demagnetization of rocks. *Phys. Earth Planet. Inter.* **182**, 42–49 (2010).
85. W. D. Daily, P. Dyal, Theories for the origin of lunar magnetism. *Phys. Earth Planet. Inter.* **20**, 255–270 (1979).
86. R. J. Reisener, J. I. Goldstein, Ordinary chondrite metallography: Part 2. Formation of zoned and unzoned metal particles in relatively unshocked H, L, and LL chondrites. *Meteorit. Planet. Sci.* **38**, 1679–1696 (2003).
87. L. Kaufman, M. Cohen, The martensitic transformation in the iron-nickel system. *JOM* **8**, 1393–1401 (1956).
88. J. A. Wood, The cooling rates and parent planets of several iron meteorites. *Icarus* **3**, 429–459 (1964).
89. L. J. Swartzendruber, V. P. Itkin, C. B. Alcock, The Fe-Ni (iron-nickel) system. *J. Phase Equilibria* **12**, 288–312 (1991).
90. G. W. Pearce, W. A. Gose, D. W. Strangway, Magnetic studies of Apollo 15 and 16 lunar samples. *Proc. Lunar Planet. Sci. Conf.* **4**, 3045–3076 (1973).
91. C. J. Hale, M. Fuller, R. C. Bailey, On the application of microwave heating to lunar paleointensity determination. *Proc. Lunar Planet. Sci. Conf.* **9**, 3165–3179 (1978).
92. A. Stephenson, Three-axis static alternating field demagnetization of rocks and the identification of natural remanent magnetization, gyroremanent magnetization, and anisotropy. *J. Geophys. Res.* **98**, 373–381 (1993).
93. D. J. Dunlop, Viscous magnetization of 0.04–100 μm magnetites. *Geophys. J. Roy. Astron. Soc.* **74**, 667–687 (1983).
94. E. Thellier, Sur l'aimantation des terres cuites et ses applications géophysiques. *Ann. Inst. Phys. Globe* **16**, 157–302 (1938).
95. S. M. Cisowski, D. W. Collinson, S. K. Runcorn, A. Stephenson, M. Fuller, A review of lunar paleointensity data and implications for the origin of lunar magnetism. *J. Geophys. Res.* **88**, A691–A704 (1983).
96. A. Stephenson, D. W. Collinson, Lunar magnetic field palaeointensities determined by an anhysteretic remanent magnetization method. *Earth Planet. Sci. Lett.* **23**, 220–228 (1974).
97. A. Stephenson, S. K. Runcorn, D. W. Collinson, Paleointensity estimates from lunar samples 10017 and 10020. *Proc. Lunar Planet. Sci. Conf.* **8**, 679–687 (1977).
98. J. Gattacceca, P. Rochette, Toward a robust normalized magnetic paleointensity method applied to meteorites. *Earth Planet. Sci. Lett.* **227**, 377–393 (2004).
99. P. Wasilewski, Magnetization of small iron-nickel spheres. *Phys. Earth Planet. Inter.* **26**, 149–161 (1981).
100. Y. Yu, L. Tauxe, J. S. Gee, A linear field dependence of thermoremanence in low magnetic fields. *Earth Planet. Sci. Lett.* **162**, 244–248 (2007).
101. S.-C. L. L. Lappe, J. M. Feinberg, A. R. Muxworthy, R. J. Harrison, Comparison and calibration of nonheating paleointensity methods: A case study using dusty olivine. *Geochem. Geophys. Geosyst.* **14**, 2143–2158 (2013).
102. Y. Yu, D. J. Dunlop, Ö. Özdemir, Are ARM and TRM analogs? Thellier analysis of ARM and pseudo-Thellier analysis of TRM. *Earth Planet. Sci. Lett.* **205**, 325–336 (2003).
103. R. Shaar, L. Tauxe, Thellier GUI: An integrated tool for analyzing paleointensity data from Thellier-type experiments. *Geochem. Geophy. Geosyst.* **14**, 677–692 (2013).
104. P. Rochette, Magnetic classification of story meteorites: 1. Ordinary chondrites. *Meteorit. Planet. Sci.* **38**, 251–268 (2003).
105. C. R. Pike, A. P. Roberts, K. L. Verosub, Characterizing interactions in fine magnetic particle systems using first order reversal curves. *J. Appl. Phys.* **85**, 6660 (1999).
106. R. Egli, VARIFORC: An optimized protocol for calculating non-regular first-order reversal curve (FORC) diagrams. *Global Planet. Change* **110**, 302–320 (2013).
107. R. J. Harrison, J. M. Feinberg, FORCinel: An improved algorithm for calculating first-order reversal curve distributions using locally weighted regression smoothing. *Geochem. Geophy. Geosyst.* **9**, Q01056 (2008).

108. A. P. Roberts, D. Heslop, X. Zhao, C. R. Pike, Understanding fine magnetic particle systems through use of first-order reversal curve diagrams. *Rev. Geophys.* **52**, 557–602 (2014).
109. S. Cisowski, Interacting vs. non-interacting single domain behavior in natural and synthetic samples. *Phys. Earth Planet. Inter.* **26**, 56–62 (1981).
110. D. J. Dunlop, Ö. Özdemir, *Rock Magnetism: Fundamentals and Frontiers. Cambridge Studies in Magnetism* (Cambridge Univ. Press, 1997), pp. 573.
111. R. Egli, Analysis of the field dependence of remanent magnetization curves. *J. Geophys. Res.* **108**, 2081 (2003).
112. R. A. Sadykov, N. S. Bezaeva, A. I. Kharkovskiy, P. Rochette, J. Gattacceca, V. I. Trukhin, Nonmagnetic high pressure cell for magnetic remanence measurements up to 1.5 GPa in a superconducting quantum interference device magnetometer. *Rev. Sci. Instrum.* **79**, 115102 (2008).
113. D. J. Dunlop, The rock magnetism of fine particles. *Phys. Earth Planet. Inter.* **26**, 1–26 (1981).
114. A. Stephenson, S. Sadikun, D. K. Potter, A theoretical and experimental comparison of the anisotropies of magnetic susceptibility and remanence in rocks and minerals. *Geophys. J. Roy. Astron. Soc.* **84**, 185–200 (1986).
115. G. Turner, ^{40}Ar-^{39}Ar ages from the lunar maria. *Earth Planet. Sci. Lett.* **11**, 169–191 (1971).
116. O. M. Lovera, F. M. Richter, T. M. Harrison, Diffusion domains determined by ^{39}Ar released during step heating. *J. Geophys. Res.* **96**, 2057–2069 (1991).
117. H. Fechtig, S. T. Kalbitzer, The diffusion of argon in potassium-bearing solids, in *Potassium Argon Dating*, O. A. Schaeffer, J. Zähringer, Eds. (Springer-Verlag, 1966), pp. 68–107.
118. S. Huang, Surface temperatures at the nearside of the Moon as a record of the radiation budget of Earth's climate system. *Adv. Space Res.* **41**, 1853–1860 (2008).
119. S. J. Kiehm, K. Peters, M. G. Langseth, J. L. Chute Jr., Apollo 15 measurement of lunar surface brightness temperatures thermal conductivity of the upper 1 1/2 meters of regolith. *Earth Planet. Sci. Lett.* **19**, 337–351 (1973).
120. R. C. Reedy, J. Masarik, Production rates of cosmogenic nuclides deep in the Moon. *Meteoritics* **30**, 564–565 (1995).
121. F. Hörz, E. Schneider, D. E. Gault, J. B. Hartung, D. E. Brownlee, Catastrophic rupture of lunar rocks: A Monte-Carlo simulation. *The Moon* **13**, 235–258 (1975).
122. P. T. Delaney, Heat transfer during emplacement and cooling of mafic dykes, in *Mafic Dyke Swarms*, H. C. Halls, W. Fahrig, Eds. (Geological Association of Canada, 1987), pp. 123–135.
123. M. G. Langseth, S. J. Keihm, K. Peters, Revised lunar heat-flow values. *Proc. Lunar Planet. Sci. Conf.* **7**, 3143–3171 (1976).
124. R. S. Coe, S. Gromme, E. A. Mankinen, Geomagnetic paleointensities from radiocarbon-dated lava flows on Hawaii and the question of the Pacific nondipole low. *J. Geophys. Res.* **83**, 1740–1756 (1978).
125. O. Eugster, T. Michel, Common asteroid break-up events of eucrites, diogenites, and howardites, and cosmic-ray production rates for noble gases in achondrites. *Geochim. Cosmochim. Acta* **59**, 177–199 (1995).

Acknowledgments: We thank M. Fuller for suggesting the study of regolith breccias, J. Gattacceca for sharing pressure remanent magnetization cell, B. Carbone for administrative support, and the Institute for Rock Magnetism at the University of Minnesota for use of their vibrating sample magnetometer. We also thank P. Boehnke and two anonymous reviewers for helpful suggestions. **Funding:** We thank the NASA Solar System Workings and Planetary Major Equipment Programs (grant #NNX15AL62G), the NASA Solar System Exploration Research Virtual Institute node at Brown-MIT (grant #NNA14AB01A), the MIT International Science and Technology Initiatives Global Seed Fund, the Rutgers University School of Arts and Sciences, and the Miller Institute for Basic Research in Science for financial support. **Author contributions:** S.M.T., B.P.W., and D.L.S. conceived the study and supervised the research. S.M.T. designed and carried out the experiments. C.S., H.W., and T.L.G. assisted with the experimental work and analysis. S.M.T. led the writing of the paper with contributions from B.P.W. and D.L.S. **Competing interests:** The authors declare that they have no competing interests. **Data and materials availability:** All data needed to evaluate the conclusions in the paper are present in the paper and/or the Supplementary Materials. Additional data related to this paper may be requested from the authors and will be posted in the Magnetics Information Consortium (MagIC) database (www2.earthref.org/MagIC/).

Submitted 6 February 2017
Accepted 11 July 2017
Published 9 August 2017
10.1126/sciadv.1700207

Citation: S. M. Tikoo, B. P. Weiss, D. L. Shuster, C. Suavet, H. Wang, T. L. Grove, A two-billion-year history for the lunar dynamo. *Sci. Adv.* **3**, e1700207 (2017).

A two-billion-year history for the lunar dynamo

Sonia M. Tikoo, Benjamin P. Weiss, David L. Shuster, Clément Suavet, Huapei Wang and Timothy L. Grove

Sci Adv **3** (8), e1700207.
DOI: 10.1126/sciadv.1700207

Science Advances

AAAS

advances.sciencemag.org/cgi/content/full/3/8/e1700207/DC1

Supplementary Materials for

A two-billion-year history for the lunar dynamo

Sonia M. Tikoo, Benjamin P. Weiss, David L. Shuster, Clément Suavet, Huapei Wang, Timothy L. Grove

Published 9 August 2017, *Sci. Adv.* **3**, e1700207 (2017)
DOI: 10.1126/sciadv.1700207

The PDF file includes:

- fig. S15. Schematic depicting time-temperature conditions underlying our thermochronological models.
- fig. S16. 15498 MP-MDD model predictions for diffusion of ^{40}Ar* resulting from impact heating at 2000 Ma (to temperatures ranging between 450° and 675°C), followed by daytime heating to an effective mean temperature of 69°C after 600 Ma.
- fig. S17. 15498 MP-MDD model predictions for diffusion of ^{40}Ar* resulting from impact heating at various times in lunar history (to temperatures ranging between 450° and 675°C), followed by daytime heating to effective mean temperatures ranging between 35° and 56°C after 600 Ma.
- fig. S18. 15498 MP-MDD model age spectra incorporating diffusion of ^{40}Ar* resulting from impact heating at 650 Ma (to temperatures ranging between 450° and 675°C), followed by daytime heating to an effective mean temperature of 25°C after 600 Ma.
- table S1. WDS measurements of metal grains in 15498 thin sections 298 and 299.
- table S2A. NRM components identified for interior matrix glass subsamples of 15498.
- table S2B. NRM components identified for peripheral matrix glass subsamples of 15498.
- table S2C. Fisher mean component directions derived from 15498 data in table S2A.
- table S3A. Thellier-Thellier paleointensity determinations for 15498 subsamples.
- table S3B. Comparison of pTRM and pTRM check values for 15498 subsamples.
- table S3C. ARM paleointensity determinations for 15498 subsamples.
- table S3D. IRM paleointensity determinations for 15498 subsamples.
- table S4. Rock magnetic and hysteresis parameters.
- table S5. Anisotropy of ARM (85-mT ac field with 0.01-mT dc field).
- table S6. Complete ^{40}Ar/^{39}Ar incremental heating results.
- table S7. Oxide weight percent compositions of K-bearing phases in basalt clast 15498-282-1.
- table S8. Summary of MP-MDD model parameters with cosmogenic ^{38}Ar production rates for 15498.
- table S9. Summary of ^{40}Ar/^{39}Ar chronology for 15498.
- table S10. Reduced χ^2 misfit statistics for best-fit thermochronometry models for a variety of breccia formation ages.
- References (*66–125*)

Other Supplementary Material for this manuscript includes the following:
(available at advances.sciencemag.org/cgi/content/full/3/8/e1700207/DC1)

- data file S1 (.txt format). 15498 demagnetization data sets.
- data file S2 (.txt format). 15498 Thellier-Thellier paleointensity data sets.

section S1. Sample 15498

1.1. Geology of the Apollo 15 landing site

Apollo 15 landed on the eastern margin of Mare Imbrium, within the lava plain Palus Putredinis, in a location between Hadley Rille on the west and the Apennine Mountains on the east (fig. S1). Bedrock in the vicinity of the Apollo 15 landing site consists of mare basalt (*66*), although the

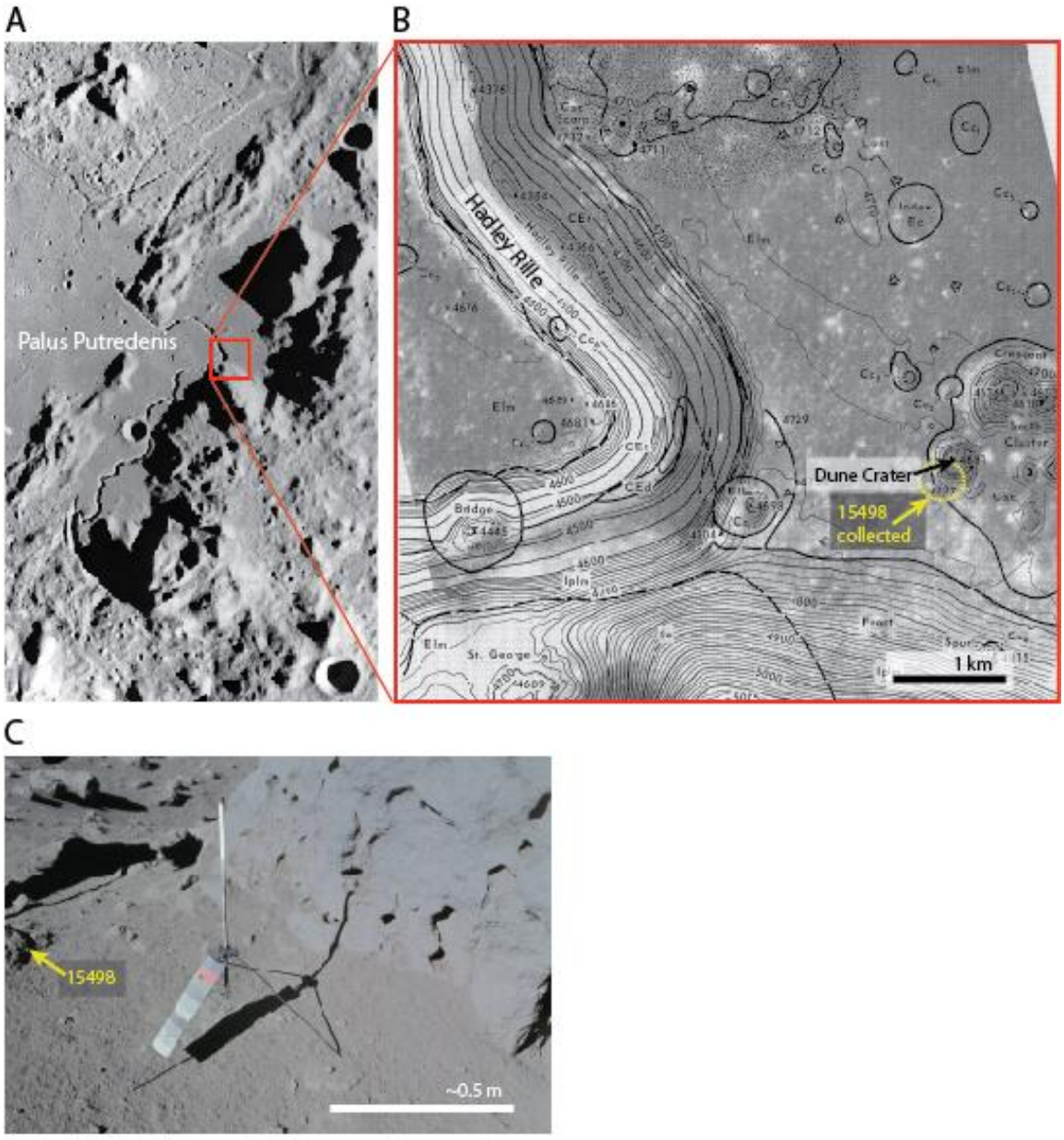

fig. S1. Apollo 15 landing site and 15498 sampling context. (**A**) Context image of Palus Putredinis, in the southeastern region of Mare Imbrium. (**B**) Location of the Apollo 15 landing site, showing locations of Hadley Rille and Dune Crater, near which sample 15948 was collected from the regolith. (**C**) Location where sample 15498 was collected, near the southwestern rim of Dune Crater.

nearby Apennine Mountains contain substantial upper crustal (anorthositic) and lower crustal (noritic) material that was uplifted during the Imbrium impact event (*67*, *68*). The Apollo 15 mare basalts are typically divided into two main petrologic groups based on petrographic characteristics and major element chemistry: quartz-normative basalts (QNB) and olivine-normative basalts (ONB) (*69*–*73*). These mare basalts primarily formed during the period ~3.25-3.35 Ga (*44*). Since that time, impact bombardment has produced a regolith that consists mostly of basalt and basaltic soil breccias such as our sample 15498 along with fragments of highlands rocks (*66*).

The constituents of regolith breccias at the Apollo 15 landing site, including 15498, are locally derived (*74*). There are several craters, ranging in size, in the vicinity of the Apollo 15 landing site that could have been the source of 15498: Dune Crater (the crater closest to where 15498 was collected), Bridge Crater, Elbow Crater, St. George crater, and more. In particular, Dune crater may be a secondary crater of either the Aristillus or Autolycus craters, which have ejecta rays extending to the Apollo 15 landing site (*75*). Aristullus and Autolycus, which are located in the eastern portion of Mare Imbrium (~130-180 km away from the Apollo 15 landing site) are inferred to be about 1.3 Ga and ≤2.1 Ga, respectively, based on $^{40}Ar/^{39}Ar$ dating of Apollo 15 potassium, rare earth elements, and phosphorous (KREEP) basalts thought to be sourced from those craters (*76*–*78*). These ages for Aristillus and Autolycus are indistinguishable from the age range we present for 15498 in this work (see main text and Section 5). Therefore, if Dune crater is indeed (*i*) the source crater for 15498 as well (*ii*) a secondary crater created by the impact of ejecta from either Aristillus or Autolycus, then the inferred 1.3-2.1 Ga age for Dune crater is consistent with our age range for 15498 (see main text and Section 5). However, given these uncertainties, it is difficult to conclusively link 15498 to a specific crater and a corresponding age based on geologic context alone.

1.2. Petrographic description and formation history of 15498

Sample 15498 is a regolith breccia. Its petrography was described in detail by Mason (*33*) and Ryder (*34*). The rock contains 20% clasts typically ~0.5-2 mm in size (and ranging up to ~1 cm) that are predominantly of local Apollo 15 mare basalt origin (*35*), although limited highlands and KREEP-rich materials are also present (fig. S2). The clasts are welded together by a matrix that comprises the remaining 80% of the sample and consists of ~50% impact melt glass and ~50% fine (< 0.5 mm) clastic material, mineral fragments, and glass fragments from the lunar soil. In aggregate, the rock consists of ~60% lithic and clastic material and ~40% impact melt glass. A network of glass-lined fissures crosscuts the rock. Surficial impact melt glass spatters of varying thickness (locally up to ~6 mm) partially coat the surface of the rock. The lack of microfractures in the bulk rock away from the fissures (fig. S3) suggests it has not experienced shock pressures above ~3 GPa during its post-lithification residence on the lunar surface.

We consider the peak temperature and cooling rates experienced by the clastic material and melt matrix in 15498 during its formation. 15498 is thought to have formed by an impact event that

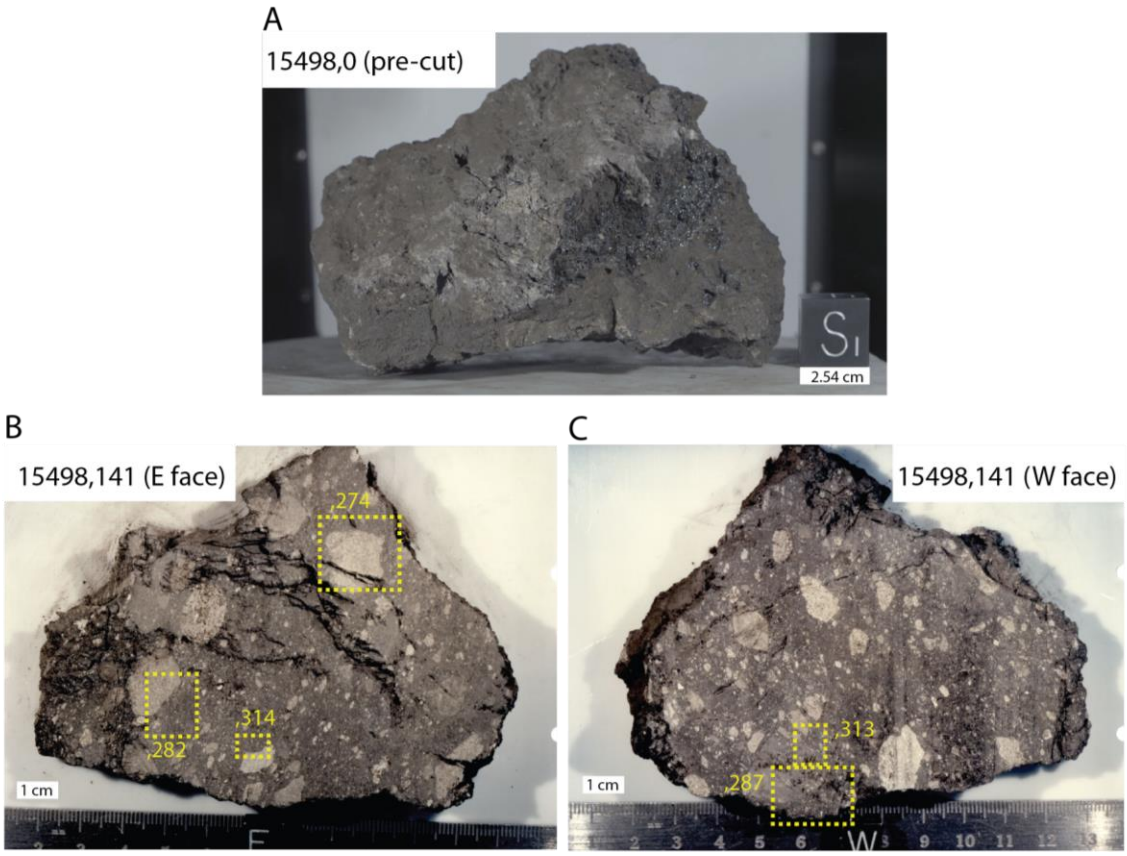

fig. S2. Sample 15498. (**A**) Image of 15498,0 main mass showing exterior with impact glass spatter. (**B**) Image of East (laboratory coordinates) face of slab 15498,141. Locations from which our parent chips 15498,274, 15498,282, and 15498,314 were collected are labeled. (**C**) Image of West face of the slab, with location of parent chips 15498,287 and 15498,313 labeled. Figure adapted from NASA images *S71-45982*, *S85-43128*, and *S85-43129*.

assembled regolith fragments together and welded them with newly-formed molten impact-melt glass. As discussed by Uhlmann and Klein (*37*), the assembly process likely had two stages. First, cold (<100°C) clasts were first mixed with melt that was initially at or above its 1270 ± 10°C liquidus temperature, leading to rapid cooling to a uniform temperature. This was followed by a second stage of slow-cooling by thermal conduction into the surrounding matrix and/or by radiation into space.

We seek to determine the peak equilibration temperature, T_{eq}, of the clasts and breccia after they were assembled by the impact during the first stage. Continuous cooling and time-temperature curves corresponding to the degree of crystallinity in the 15498 glass indicate that during the first stage, the glass cooled at a rate of ~130°C min^{-1}. If we assume that clasts were not significantly digested by the surrounding melt, then the petrographic observations described above indicate that the initial mixture consisted of approximately 2/3 clasts and 1/3 melt. We assume that the heat capacity of the clasts, c_c, and the melt, c_m, are equal (*79*). Given that the latent heat of fusion for silicates is equivalent to heat released by cooling the same amount of melt by ~400°C (*79*), it will buffer the melt temperature during crystallization. Based on this, conservation of energy indicates that (*79*)

$$m_c\, c_c\, (T_{eq} - T_c) = m_m\, c_m\, (T_m - T_{eq}) + m_m\, c_m\, (400°C) \qquad (1)$$

where $m_c = 2\, m_m$, $c_c = c_m$, T_c = 100°C (initial temperature of clasts), and T_m = 1270°C (liquidus temperature, assumed to be the initial temperature of the melt). Solving for the clast equilibration temperature gives T_{eq} = 623°C. Note that this equilibrium temperature is more accurate than the 807°C value reported by Uhlmann and Klein (*37*), which was estimated from the inaccurate assumption that $m_c = 0.5 m_m$. Also note that this temperature is a lower limit because the melt may have initially been at a temperature exceeding the liquidus.

Cooling during the second stage was limited by conduction within the rock volume and into the surroundings. A minimum cooling rate during this stage can be estimated assuming the rock's present size (18 × 14 × 12 cm) was no smaller than its original size after assembly. Using a radius l = 0.07 m and thermal diffusivity $D = 10^{-6}$ m^2 s^{-1}, we find that the *e*-folding conductive cooling timescale from 623°C is $t > l^2 / D$ = 1.4 h.

1.3. Petrographic constraints on 15498 paleomagnetism

Thermoremanent magnetization (TRM) is acquired when rocks cool below their Curie or ordering temperatures [780°C for the mineral kamacite (α-$Fe_{0.95\text{-}1}Ni_{0\text{-}0.05}$)] in the presence of an ambient magnetic field. Rocks may acquire secondary shock remanent magnetization (SRM) from the passage of impact shock waves in the presence of a field (*50*, *80–82*). In the absence of a field, rocks may experience shock demagnetization (*81*, *83*, *84*). However, the relatively low extent of post-formational shock (<~3 GPa) experienced by the glass matrix of 15498, as evidenced by the relative lack of microfractures (fig. S3), suggests that the rock is unlikely to have been completely demagnetized or remagnetized by secondary shock processes. Therefore, 15498 should retain a substantial fraction of any magnetization acquired during primary cooling. The ambient field required for imparting primary TRM or secondary SRM can either be a long-lived field such as that from an active dynamo or crustal remanence (*85*) or a transient field generated or amplified by the motions of impact plasmas (*31*, *32*). While impacts are in principle capable of generating fields lasting as long as ~1 day for the largest, basin-forming impacts (*30*), impact fields are unlikely to persist for longer than a few seconds for the smaller impacts which took place on the moon after ~3.7 Ga (*8*, *31*, *32*). If a rock preserves TRM, determining the primary cooling timescale informs regarding whether the rock acquired its natural remanent magnetization (NRM) from a long-lived dynamo or crustal field or a transient impact-generated field. The minimum second-stage cooling rate discussed in Section 1.2 indicates that 15498 cooled from the 623°C equilibrium temperature to ambient lunar surface temperatures (~0°C) over a period of a few hours. This timescale is much longer than the expected duration of impact-generated fields after 3.7 Ga. Therefore, TRM observed in 15498 would be a record of a long-lived field such as that from a dynamo or crustal remanence rather than an impact-generated field.

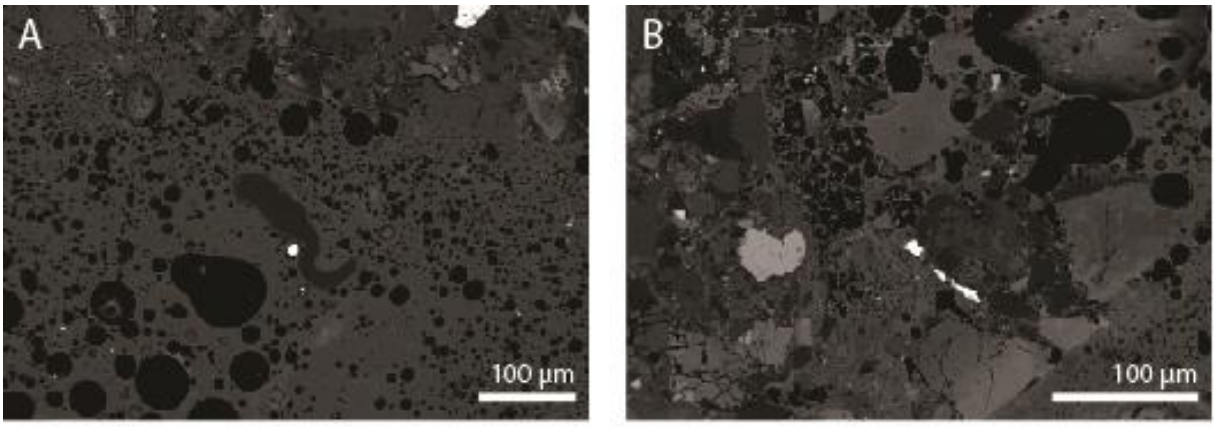

fig. S3. Backscattered scanning electron microscopy images of 15498 matrix showing absence of post-lithification microfracturing. (**A**) Vesicular impact melt glass mostly devoid of lithic fragments. (**B**) Glass matrix containing entrained lithic fragments.

1.4. Ferromagnetic mineralogy

We employed optical petrography as well as wavelength dispersive spectroscopy (WDS) and backscattered electron microscopy (BSEM) to determine the mineralogical and elemental composition of the metallic magnetization carriers in 15498 thin sections 298 and 299 (table S1). Single-phase <1 μm metal grains are found as neoformed crystals in the matrix glass and as <1-50 μm grains in lithic material that formed prior to breccia assembly (fig. S4). Lithic metal grains manifest as inclusions within pyroxene or as independent fragments between silicates. The fine grain sizes of neoformed metal grains in the matrix glass are broadly consistent with hysteresis data that indicate a bulk superparamagnetic to pseudo single domain grain size for ferromagnetic minerals in the 15498 glass (Section 4) (*39*).

We measured elemental abundances for Fe, Ni, P, Co, S, Si, Al, W, Ti, O, and Cr within metal grains in both the melt glass and lithic portions of thin sections 298 and 299 using a JEOL-JXA-8200 electron microprobe housed at the MIT Electron Microprobe Facility. The isolated metal grains in the melt glass portion of the matrix were generally too small (<1 μm in diameter) to be accurately measured (fig. S4). However, we were able to measure elemental abundances for a two-point transect across one isolated grain in the matrix glass (grain 2T in table S1), as well as for many larger lithic metal grains. In agreement with a previous study (*38*), our WDS analyses found that these grains are predominantly Fe-Ni-Co alloys, with 0-19 wt. % Ni and 0-2 wt. % Co, with 11 out of 13 clastic FeNi grains having Ni contents <10 wt. %. Our WDS measurements found that 1 out of 13 clastic metal grains and the single neoformed metal grain

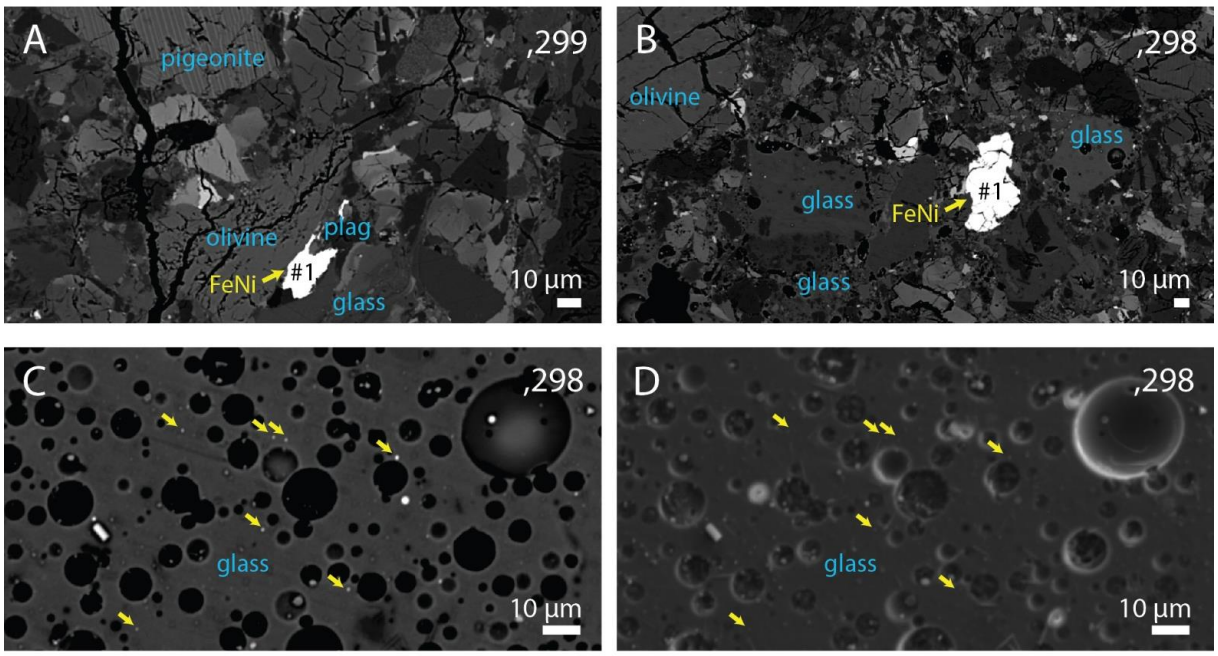

fig. S4. BSEM images of FeNi grains in 15498. (**A**, **B**) Clastic FeNi fragments (yellow arrows and labels) within the glassy matrix. (**C**) Neo-formed FeNi grains (arrows) crystallized from vesicular impact melt glass. (**D**) Secondary electron microscope (SE) image of the same region shown in (C). FeNi grain numbers indicate corresponding WDS measurement numbers in Table S1. Melt glass matrix and other clastic minerals are labeled in blue.

analyzed had P contents above the detectable threshold (0.03 wt. %). It is possible that the presence of P may have facilitated the development of equilibrium kamacite-taenite intergrowths during primary cooling in such grains (*86*). However, the observed metal compositions, the consistent Ni content measured across transects of metal grains (varying by no more than 1.5 wt. %), and the rapid ~1 h cooling time scale corresponding to the breccia's formation collectively suggest that the primary ferromagnetic carriers in 15498 are most likely individual grains of single-phase kamacite and martensite (*87*, *88*). In support of this, our BSEM observations (fig. S4) did not reveal any obvious intergrowth textures that would indicate Widmanstätten or plessitic exsolution. Ref. (*38*) reported the presence of two-phase assemblages of kamacite and a higher Ni phase present as inclusions within troilite within and in the proximity of one olivine gabbro clast. As such, it is possible that small quantities of two-phase assemblages of kamacite and taenite are present within the sample at large, although no two-phase FeNi assemblages or troilites were observed in our thin sections.

In the presence of a stable ambient field, kamacite grains in the melt glass would record a TRM as they cooled below their 780°C Curie temperature. Depending on their composition (5-19 wt. % Ni), martensite grains in the melt glass would begin to form at martensite-start temperatures ranging between ~680ºC (low-Ni) and ~240°C (high-Ni). The martensite grains would finish crystallizing at martensite-finish temperatures ranging between ~620°C (low-Ni) and ~140°C (high-Ni) (*89*). In general, the presence of kamacite and the narrow temperature interval (~100°C) over which individual martensite grains form indicate the rock would have acquired mostly a TRM rather than a thermochemical remanent magnetization (TCRM) if an ambient magnetic field was present during primary cooling. During thermal demagnetization, kamacite should completely demagnetize by the 780°C Curie point, while martensite should transform to taenite at austenite-finish temperatures ranging from ~600ºC (high-Ni) to 780°C (low-Ni). This also means that we expect that during our Thellier-Thellier experiments, thermochemical alteration should begin to set in at temperatures somewhere between 600-780°C

1.5. Sampling

In October 1985, the main mass of 15498 (15498,0) was cut with a band saw at Johnson Space Center (JSC) to produce slab 141. In August 2012, 3 parent chips (274, 282, and 287) were produced from slab 141 at JSC (fig. S2). These parent chips arrived at the Massachusetts Institute of Technology (MIT) Paleomagnetism Laboratory in late September 2012. In mid-January 2015, 2 additional parent chips (313 and 314) were produced from slab 141 at JSC and arrived at MIT prior to the end of that month. After arrival at MIT, we divided the matrix glass portions of each parent chip into a total of 20 subsamples using a wire saw in our magnetically shielded room. Chip 274 was subdivided into 7 matrix subsamples (274d, 274v3, 274v5, 274v6, 274v8, and 294v9), one sample of the surficial young glass rind (274a) and a composite sample of interior matrix and surficial glass spatter (274t). Chip 282 was subdivided into 4 matrix subsamples (282a, 282b, 282c, 282t). Chip 287 was subdivided into 1 matrix subsample (287b) and a composite sample of interior matrix and surficial glass rind (287a). Chip 313 was subdivided into 5 matrix subsamples (313e, 313h, 313j, 313k1, and 313k2). Chip 314 was used in its entirety as a single subsample, hereafter referred to as 314a. The matrix material in our subsamples consists of mostly impact melt glass and a fraction (typically <~30%) of entrained lithic fragments. All glass-bearing subsamples were mutually re-oriented using photographic

documentation of subsampling according to JSC orientation conventions. We also studied one unoriented basalt clast fragment from parent chip 282 (subsample 282h) and two thin sections (298 and 299). Subsamples 274d, 274t, 274v3, 274v5, 274v8, 274v9, 282a, 282b, 282c, 282t, 287a, and 314a were collected from the band saw cut face of slab 141. Subsamples 274a, 274v6, 287b, 313e, 313h, 313j, 313k1, and 313k2 were collected at least ~0.25 cm away from the band saw cut face. Sections 298 and 299, used for petrographic and compositional analyses, were produced from materials adjacent to parent chips 287 and 282, respectively.

section S2. NRM behavior

2.1. Previous paleomagnetic studies of 15498

The <3.3 Ga formation age and small (<1 μm) ferromagnetic grain sizes for sample 15498 present a fortuitous opportunity to study the NRM of an exceptionally high magnetic fidelity sample that formed after the lunar dynamo precipitously declined between 3.56 and ~3.3 Ga. Previous paleomagnetic studies were conducted on two subsamples collected from the interior of 15498 (35 and 36) that were not mutually oriented (*39, 40, 90*). Both subsamples were subjected to stepwise alternating field (AF) demagnetization up to 40 mT. After this AF pre-treatment, subsample 36 was further demagnetized using thermal demagnetization up to 700°C. Both subsamples 35 and 36 contained a directionally stable NRM component that persisted up to the maximum applied AF level. During thermal demagnetization of subsample 36, this magnetization component continued to remain stable up to an unblocking temperature of 650°C. Above 650°C, the sample experienced significant thermal alteration. A modified Thellier-Thellier (*41*) experiment yielding a paleointensity of ~2.1 μT was made in conjunction with the thermal demagnetization experiment (*40*). Microwave heating Thellier-Thellier paleointensity experiments were also attempted on clastic material from 15498 (*91*), although the resulting paleointensities (~0.3-0.5 μT) are likely unreliable because the clasts do not retain stable remanence (Section 2.3.1). While the previous AF and thermal demagnetization studies demonstrated that the glass matrix portion of 15498 carried a highly stable magnetization component that persisted to high unblocking temperatures, the authors did not determine the age of its NRM and were unable to unambiguously demonstrate whether it was acquired in an ancient lunar dynamo field. Our goal is to conclusively determine the origin of NRM in 15498.

Methods

Essentially all previous thermal demagnetization and Thellier-Thellier experiments on lunar rocks have failed due to the multidomain grain size of the majority of lunar rocks and thermochemical alteration caused by laboratory heating (*7, 28*). The abundance of single and pseudo-single domain grains within the glass matrix of 15498 means that it is not limited by the former difficulty. To avoid the latter difficulty, we conducted thermal demagnetization experiments on 13 subsamples in a controlled oxygen fugacity environment specially designed to mitigate thermochemical alteration (*58*). 4 of these 13 subsamples were AF-pretreated to ac fields of ~30-35 mT to remove low coercivity overprints prior to heating. We supplemented these thermal demagnetization measurements with nondestructive stepwise AF demagnetization methods for 7 additional subsamples. AF demagnetization also has the advantage over thermal demagnetization of more effectively removing nonthermal overprints such as SRM (*50, 51, 80*) and contaminating magnetization produced by strong artificial magnetic fields during sample handling and transport (*90*).

Static three-axis AF demagnetization experiments were conducted on the 7 AF subsamples up to 290 mT (all subsamples except 282c) or 420 mT (subsample 282c, which was analyzed after a new AF demagnetization system capable of reaching higher peak ac fields was installed at MIT). Samples initially magnetized in a weak to null magnetic field that have a substantial population of low-coercivity (multidomain) grains are particularly susceptible to magnetic contamination by the acquisition of spurious anhysteretic remanent magnetization (ARM) and gyroremanent magnetization (GRM) during AF demagnetization experiments (*92*). As AF demagnetization proceeds, the magnitude of acquired ARM and GRM increases until the remaining NRM is overwhelmed at high AF levels. Because the lunar dynamo field had likely declined to below ~5 μT before sample 15498 formed (*8*) and because lithic fragments within the breccia contain occasional multidomain FeNi grains that will preferentially acquire spurious remanence during the earlier stages of the demagnetization, care must be taken to identify and correct AF data for the acquisition of these spurious remanences. In our experiments, AF was applied along each orthogonal axis and the data were averaged to mitigate the effects of spurious ARM and GRM.

Subsamples were measured in differing orientations to mitigate systematic influence of any ambient stray magnetic fields. Following the demagnetization experiments, the data from each subsample were rotated into the JSC coordinate system for interpretation of mutually oriented remanence directions (table S2). As the original demagnetization system at MIT could only apply transverse (along the *x*- and *y*- directions) AF fields up to 85 mT, the subsamples (with exception of 282c) were rotated manually for AF applications and measurements above 85 mT until the maximum AF level of 290 mT. Subsample 282c (which was demagnetized using the new AF system) was rotated manually for AF applications above 140 mT.

2.3. Demagnetization results

2.3.1. Mare basalt portion. Consistent with previous paleomagnetic studies of young (≤3.3 Ga) mare basalts, an unoriented basalt clast chip (15498,282h) exhibited unstable AF demagnetization behavior. A low coercivity (LC) component unblocked below 8 mT and no stable remanence was present at higher AF levels. This nonideal demagnetization behavior can be ascribed to the poor magnetic recording properties of multidomain FeNi grains in mare basalts that preclude retrieval of thermoremanent magnetization acquired in weak (generally <~20 μT) ambient fields using AF methods. Therefore, we did not conduct paleomagnetic measurements on any additional basalt clasts and we do not further discuss data from subsample 282h in this work.

2.3.2. Interior matrix glass subsamples. Among the 20 total matrix glass subsamples, 12 subsamples were prepared from the interior of the rock (>~0.7 cm from where a ~1-2 mm thick melt glass spatter variably coats the surface). Out of these 12 subsamples, the 5 subsamples subjected to purely AF demagnetization contained three NRM components: an LC overprint that unblocked below 6.5 mT, a medium coercivity (MC) secondary magnetization that unblocked below 50 mT, and an apparently primary high coercivity (HC) magnetization that unblocked up to the maximum applied AF level (290 or 420 mT, depending on subsample). Thermal demagnetization experiments on the other 7 subsamples revealed the presence of low temperature (LT) component that unblocked below 125-200°C and medium temperature (MT) secondary components that unblocked below 250°C (note that several subsamples lacked a

MC/MT component), followed by stable high temperature (HT) components blocked up to the 780°C Curie temperature of kamacite.

The LC/LT and MC/MT components were generally non-unidirectionally oriented amongst the subsamples (see Fig. 5 of the main text). Although the HC/HT components typically persisted above 290 mT (e.g., Fig. 4 of the main text), we only conducted principal component analysis (PCA) (*59*) fits on magnetization components for AF levels up to 85 mT to mitigate the influence of spurious remanence acquired at higher AF levels on our fit directions. The deviation angle (DANG) and maximum angular deviation (MAD) values for each HC/HT component were then compared to qualitatively assess whether they were origin-trending (*60*). In this test, the angle between the component direction and a line connecting the origin to the centroid of the data (DANG) is compared with the MAD of the component. If the MAD value is greater than the DANG value, the component is considered to be origin-trending. HC/HT components were origin-trending for the majority (6 out of 8) of subsamples, suggesting that they represent primary magnetization.

2.3.3. Peripheral matrix glass subsamples. The melt glass spatter on the edge of 15498 formed after the interior breccia but certainly while the sample was on the Moon. Therefore, it affords the opportunity of a baked contact test (*47*) for establishing whether the NRM of the interior breccia predates sampling by the Apollo astronauts. With this motivation, 8 subsamples were collected from closer to the periphery of 15498, within proximity (≤7 mm) of the variably ~1-6 mm thick impact melt glass rind coating the rock's surface. The glass rind thicknesses from the

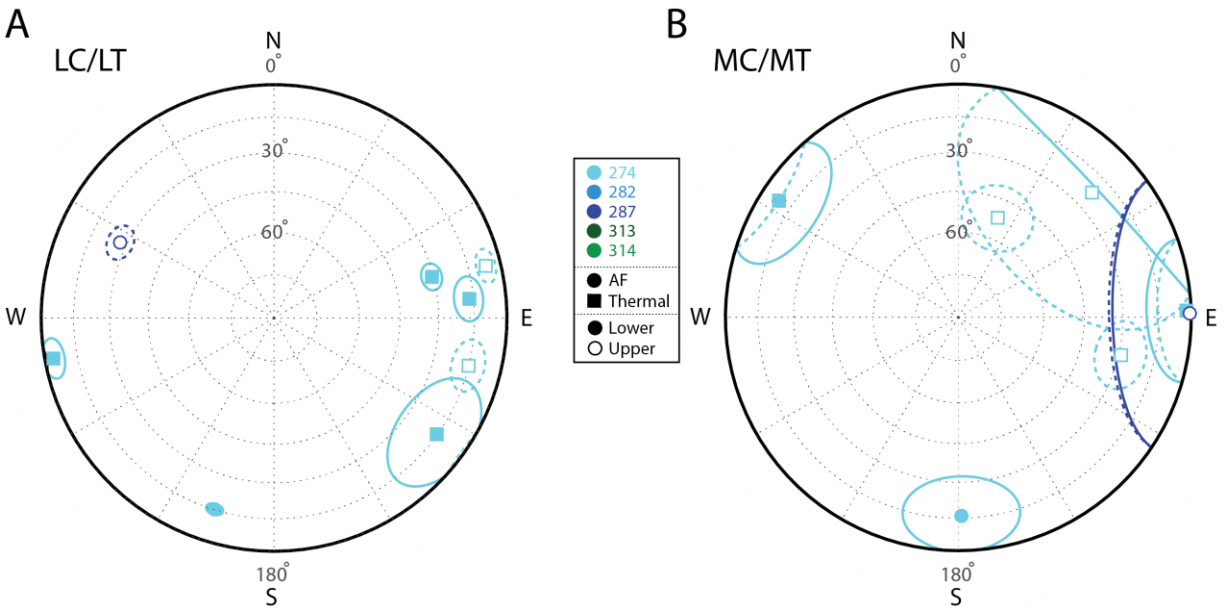

fig. S5. Equal-area stereographic projections of LC/LT and MC/MT magnetization components observed for peripheral subsamples of 15498. (**A**) LC (circles) and LT (squares) component directions. (**B**) MC (circles) and MT (squares) component directions. Lines encircling component directions represent the MAD associated with the component. Open symbols (dashed lines) represent directions in the upper hemisphere, while filled symbols (solid lines) represent directions in the lower hemisphere. Subsamples from parent chips 274, 282, 287, 313, and 314 are denoted with light blue, medium blue, dark blue, dark green, and light green symbols, respectively.

regions adjacent to where our subsamples were collected ranged between ~1-2 mm. These may be considered lower bounds on the initial spatter rind thicknesses as some material may have eroded away due to impact gardening in the lunar regolith. Out of these, subsample 274a consisted of material entirely sourced from the glass rind (approximate location outlined in Fig. 1a of the main text). Subsamples 274t and 287a consisted of a mixture of the impact glass spatter and the breccia matrix. The remaining 5 subsamples were collected along a transect starting adjacent to the glass spatter and moving progressively inward into the breccia. The centers of subsamples 274v8 and 274v9 were located ~0.2 cm away from the edge of the spatter. Subsamples 274v5 and v6 were located ~0.5 cm away from the edge. Subsample 274v3 was collected from ~0.7 cm away from the edge. Purely AF demagnetization was conducted on subsamples 274a and 287a. Subsamples 274v3, 274v5, and 274v9 were AF demagnetized using ac fields up to 30 mT prior to controlled atmosphere thermal demagnetization. Subsamples 274t, 274v6, and 274v6 were subjected to purely thermal demagnetization.

All AF demagnetized peripheral subsamples contained LC/LT magnetization components blocked up to ~7 mT or 200°C, respectively. 6 out of 8 subsamples contained one or more MC/MT components blocked up to ~37 mT or ~360°C, respectively. The MT component for 274v3 (0.7 cm away from the edge of the sample) may have persisted above 480°C (the maximum heating step applied to the peripheral batch of subsamples), but there was no appreciable decay in remanence between ~300 and 480°C (so temperatures within this range were excluded from our PCA fits). Note that the MT component direction for 274v3 resembles that of the HT component in the interior subsamples and may represent the same magnetization event (table S2). Also note that subsample 287a had a second MC component (MC2) blocked up to 85 mT and 274t had a second MT (MT2) component blocked up to 550°C. However, these two subsamples were prepared from the saw cut face of 15498 and as a result they may have acquired some surficial contamination from the saw blade that was not fully removed by sanding. The magnetization directions of the MC2 and MT2 components (as well as the aforementioned LC/LT and MC/MT) are scattered and are not consistent with that of the HT component observed in the interior subsamples (fig. S5).

We also compared the residual NRM intensities after heating to 300°C for subsamples collected from the interior of the rock to those collected from the periphery near the glass spatter. We found that the interior subsamples consistently had residual NRM intensities at least 4 times higher than the NRMs of the peripheral subsamples near the young melt glass rind (Fig. 8 of the main text). The absence of stable HC/HT remanence and low NRM intensities observed in nearly all peripheral subsamples strongly suggest that the interior subsamples were thermally demagnetized on the Moon from the emplacement of the impact melt glass spatter at high temperatures in a null field. The contrasting remanence behaviors of the peripheral subsamples relative to the interior subsamples coupled with the fact that high temperature magnetization in subsample 274v3 (the farthest from the melt glass rind) is similar to that in the interior subsamples are indicative of a positive baked contact test (*47*). These data indicate that the HC/HT component in the interior subsamples represents primary magnetization acquired in a stable field on the Moon when the breccia formed.

2.4. Interpretation of matrix glass NRM from 15498 interior subsamples

2.4.1. LC/LT magnetization and MC/MT magnetization. The absence of aqueous alteration excludes secondary weathering CRM as the source of any magnetization in 15498. The non-unidirectional nature of the LC/LT and MC/MT components and their low (generally <250°C) unblocking temperatures and low (<50 mT) coercivity relative to the peak unblocking temperatures and grain coercivities in the rock preclude total TRM. Because these subsamples were collected from a slab that had been prepared using a band saw, it is possible that a partial TRM (pTRM) was acquired during dry saw cutting (*8*). Physical contamination from the band saw blade is entirely precluded for subsamples that were not directly collected from the saw cut face (e.g., all subsamples from chip 313). Because JSC saw cut faces of subsamples were sanded off within our magnetically shielded room prior to paleomagnetic measurements, significant surficial contamination from the saw blade is unlikely for most subsamples, except for possibly the MT components observed in subsamples 274t and 314a (i.e., the only subsamples with overprints that persisted to unblocking temperatures >360°C). SRM acquired on the Moon is likely also precluded given the non-unidirectional nature of these components. In contrast, isothermal remanent magnetization (IRM) acquired from exposure to strong magnetic fields is in principle capable of creating non-unidirectional secondary magnetizations. However, the low NRM/IRM (<<0.1) ratios of these subsamples over the coercivity ranges of the LC/LT and MC/MT fractions (Section 3.1.3-3.1.4) likely exclude an IRM origin, although it is possible that these components reflect viscously decayed IRM. As discussed in detail in Section 4.4, the highly viscous nature of this sample and the <250°C unblocking temperatures associated with most of these components suggest that the LC/LT and MC/MT components are predominantly viscous remanent magnetization (VRM) from the terrestrial field. The non-unidirectional nature of these components is likely explained by differing VRM acquisition rates between the melt glass (which typically has pseudo-single domain and smaller ferromagnetic grains) and entrained <1 mm lithic fragments (which have multidomain ferromagnetic grains), and the fact that the sample was rotated and stored in different orientations numerous times during its >42-year residence at JSC (e.g., in between our two sample allocations in 2012 and 2015). Previous experiments on magnetite have shown that VRM acquisition rates tend to vary with ferromagnetic grain size (*93*).

2.4.2. HC/HT magnetization. The HC/HT magnetization components in the interior subsamples of 15498 are generally origin-trending (table S2) and unidirectional across mutually oriented subsamples (see Fig. 6 of main text). During demagnetization experiments, they persist to the highest applied AF levels (>290 mT) and are blocked up to somewhere between 660-780°C. These features are consistent with the HC/HT component being a TRM carried by martensite- and kamacite-bearing samples. To further assess whether the HC/HT component is a TRM, we compared the AF demagnetization curve of the HC component in subsample 282a to that of laboratory ARM (a proxy for TRM), saturation IRM (SIRM), and pressure remanent magnetization (PRM, a proxy for SRM). We found that the NRM in 282a is more resistant to AF demagnetization than PRM, IRM, and ARM (fig. S6). The high stability of the NRM is broadly consistent with it being a total TRM. On the other hand, it is more stable than even ARM, which is typically considered an analog for TRM. This may because ARM is not a good analog for TRM in this sample or perhaps that the the original total TRM of 15498 was hardened by partial demagnetization of lower coercivity grains. Such hardening could have occurred if the breccia's primary NRM was partially shock demagnetized on the Moon during events

postdating breccia formation such as the impact that created the network of vesicular glass fissures that crosscut the rock. Alternatively, the low coercivity fraction of the primary magnetization could have viscously decayed on the Moon and/or in our magnetically shielded room prior to our AF demagnetization experiment. In contrast, laboratory-induced ARM, IRM, and PRM were demagnetized immediately after they were acquired, and were thus unable to substantially decay prior to measurement.

Nevertheless, the high stability and generally unidirectional nature of the HC/HT component, the successful Thellier-Thellier paleointensity experiments (Section 3.1.1), and the agreement between the Thellier-Thellier and ARM and IRM paleointensity estimates (Section 3.1.2) strongly suggests that the HC/HT component is indeed a primary TRM. Given the slow cooling time scale of the 15948 glass relative to the <~1s expected duration of impact-generated fields this late in lunar history (<3.3 Ga), any TRM carried by 15498 would require a longer-lived ambient field such as that of a core dynamo or remanent crustal fields. A dynamo origin for the NRM is favored because the ~1-3 μT paleointensities obtained from our study as well as a previous study of 15498 are orders of magnitude higher than the intensities of remanent crustal fields measured at the Apollo 15 landing site (3 nT) or at any other Apollo landing site (<350 nT) (*55*).

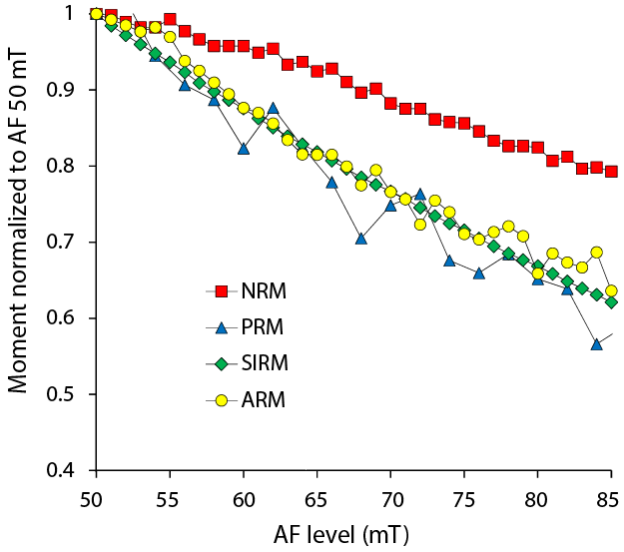

fig. S6. AF demagnetization of sample 15498,282a over the range of the HC component. Shown is the intensity of NRM (red squares) during AF demagnetization compared to that of various forms of laboratory-induced magnetization: ARM acquired in a 290 mT AC field and 3 μT DC bias field (yellow circles), IRM acquired in a 886.5 mT field (green diamonds), and PRM acquired in a field of 0.5 mT at a pressure of 2 GPa (blue triangles).

section S3. Paleointensity

3.1. Paleointensity estimates

Determining the strength of lunar surface fields at different points will constrain the longevity and power source(s) of the core dynamo. The intensity of TRM that a rock acquires during primary cooling below its Curie temperature is proportional to the strength of the magnetizing field

$$M = \chi_{\mathrm{TRM}} B_{\mathrm{paleo}} \quad (2)$$

where B_{paleo} is the ancient magnetizing field intensity (paleointensity) and χ_{TRM} is the TRM susceptibility of the source rocks (*94*).

There are two broad classes of techniques for recovering B_{paleo}. In the Thellier-Thellier method (*41*), the natural remanent magnetization (NRM) is progressively demagnetized by stepwise heating in a zero field. Interleaved between successive demagnetization steps, a partial thermoremanent magnetization (pTRM) is given to the sample in a known field (B_{lab}) at the same temperature level as the preceding heating step. Comparing the amount of NRM lost (Δ NRM) with the amount of pTRM gained (Δ pTRM) over an equivalent temperature range allows for a direct paleointensity determination

$$B_{paleo} = \frac{\Delta NRM}{\Delta pTRM} \cdot B_{lab} \quad (3)$$

This process is repeated for sequential heating steps of increasing temperature up to the Curie temperature. An observed linear relationship between Δ NRM and Δ pTRM across the range of temperature steps associated with the primary TRM component is consistent with a robust result. It is important that the sample not alter during the laboratory heating process for the Thellier-Thellier method to be successful. Because lunar rocks formed in a much more reducing environment relative to the Earth, they are especially prone to mineralogical alteration during heating experiments unless proper care is taken to control for oxygen fugacity (*58*). Furthermore, lunar samples often contain secondary IRM components (typically blocked <10 mT) that were likely acquired during sample return and handling (*9*). They may have also acquired SRM overprints during impact events on the lunar surface (*50*). Using the Thellier-Thellier method on samples containing such nonthermal overprints may yield inaccurate results because relationship (3) does not hold when the NRM is not a TRM and also thermal demagnetization will simultaneously remove the overprint (*7*).

These limitations motivated the development of a second class of relative paleointensity techniques that do not involve laboratory heating. These methods rely on AF demagnetization instead of thermal demagnetization and use either ARM or isothermal remanent magnetization (IRM) as a proxy for laboratory TRM (*95–97*). Paleointensities from the ARM (P_{ARM}) and IRM (P_{IRM}) methods are calculated using the following formulas

$$P_{\mathrm{ARM}} = \frac{\Delta \mathrm{NRM}}{\Delta \mathrm{ARM}} \cdot \frac{b}{f'} \quad (4)$$

$$P_{\mathrm{IRM}} = \frac{\Delta \mathrm{NRM}}{\Delta \mathrm{IRM}} \cdot a \qquad (5)$$

where Δ NRM, Δ ARM and Δ IRM are the changes in moment between AF demagnetization steps for NRM, ARM, and IRM , respectively, *b* is a DC bias field, *f'* is the TRM/ARM ratio, and *a* is a calibration constant with units of field. Here we adopt values of 1.34 for *f'* and 3000 μT for *a* (*96*, *98*). Note that values of *a* similar to the latter have also been measured for martensite-bearing samples (*99*). Excepting rare circumstances where grains might exhibit high shape anisotropy (*100*) or carry a substantial fraction of pseudo-single domain grains that can enter vortex states during AF applications (*53*, *61*, *101*, *102*), paleointensities derived from the ARM and IRM methods are typically accurate to within a factor 2-3 (*6*, *8*, *98*).

3.1.1. Thellier-Thellier paleointensity experiments. We conducted Thellier-Thellier paleointensity experiments following the IZZI (in-field, zero-field, zero-field, in-field) protocol (*60*) on subsamples 313e, 313h, 313j, 313k1, 313k2, and 314a (table S3a). Subsample 313j was pre-treated with AF demagnetization to 30 mT. For each temperature step, the sample was heated once in zero field and once in a laboratory field for pTRM acquisition with the ordering of IZ and ZI alternating with each subsequent temperature step. All heating experiments were conducted in a controlled atmosphere of H_2-CO_2 using the method of Suavet et al. (*58*), with the oxygen fugacity at 1 log unit below the iron-magnetite or iron-wüstite buffer. The temperature steps were in increments of 50°C between 100°C and 300°C, 30°C between 300°C and 480°C, 20°C between 480°C and 620°C, 10°C between 620°C and 640°C, and 5°C between 640°C and 680°C (except for subsample 313k1 which broke after the 660°C demagnetization step). A dc bias field of 3 μT was used for the pTRM acquisitions. Repeated pTRM acquisitions to check for alteration were made after heating to 360°C (at 300°C), 420°C (at 360°C), 480°C (at 420°C), 520°C (at 480°C), 560°C (at 520°C), 600°C (at 560°C), 630°C (at 600°C), 645°C (at 630°C), 655°C (at 645°C), 665°C (at 655°C), 675°C (at 665°C), and 680°C (at 675°C). Starting at 520°C, pTRM field application directions were reversed (nearly antipodally, by flipping the sample in the oven) after every two temperature steps to mitigate the contribution of pTRM tails to the zero-field measurements.

We obtained paleointensity values of 5.1 ± 1.6 μT (mean ± 1σ) for HT magnetization that was usually blocked between temperatures of 560°C and 660-680°C, depending on the subsample (see Fig. 7 of main text and fig. S7). At a lower unblocking temperature range (250-540°C), paleointensity values were generally lower [typically a few hundred nT, with exception of subsample 314a which had a substantial (possibly JSC saw-cutting related) overprint that was removed at 450°C]. We interpret these low values to reflect partial shock demagnetization on the Moon in a near-zero field environment, perhaps after the cessation of the lunar dynamo. This interpretation is also consistent with our observation that the NRM is more resistant to AF demagnetization than laboratory-induced ARM and SIRM, whereas ARM typically demagnetizes at a similar rate as TRM (fig. S6). Paleointensity values and corresponding Thellier quality criteria are reported in table S3a. Difference ratio sum (DRATS) alteration parameters (*60*, *103*) for the high unblocking temperature range (560-680°C) fall between 8-63%, with two subsamples' DRATS values below the 25% cutoff value above which terrestrial paleointensity experiments are typically deemed unacceptable. Above 560°C, pTRM checks came within 1-47% of corresponding initial in-field pTRM values, with 84% of pTRM checks falling within 20% of initial values across all Thellier-Thellier subsamples (table S3b). 2 out of

6 subsamples (313j and 313k1) had all pTRM check values fall within 20% of their corresponding initial pTRM values. As such, paleointensities may be robustly computed using heating steps up to at least 655°C for our 15498 subsamples (and up to 680°C for subsample 313e), consistent with the expected thermal stability of martensite with our observed Ni contents. Nevertheless, it appears that a combination of limited pTRM tails (from the small fraction of

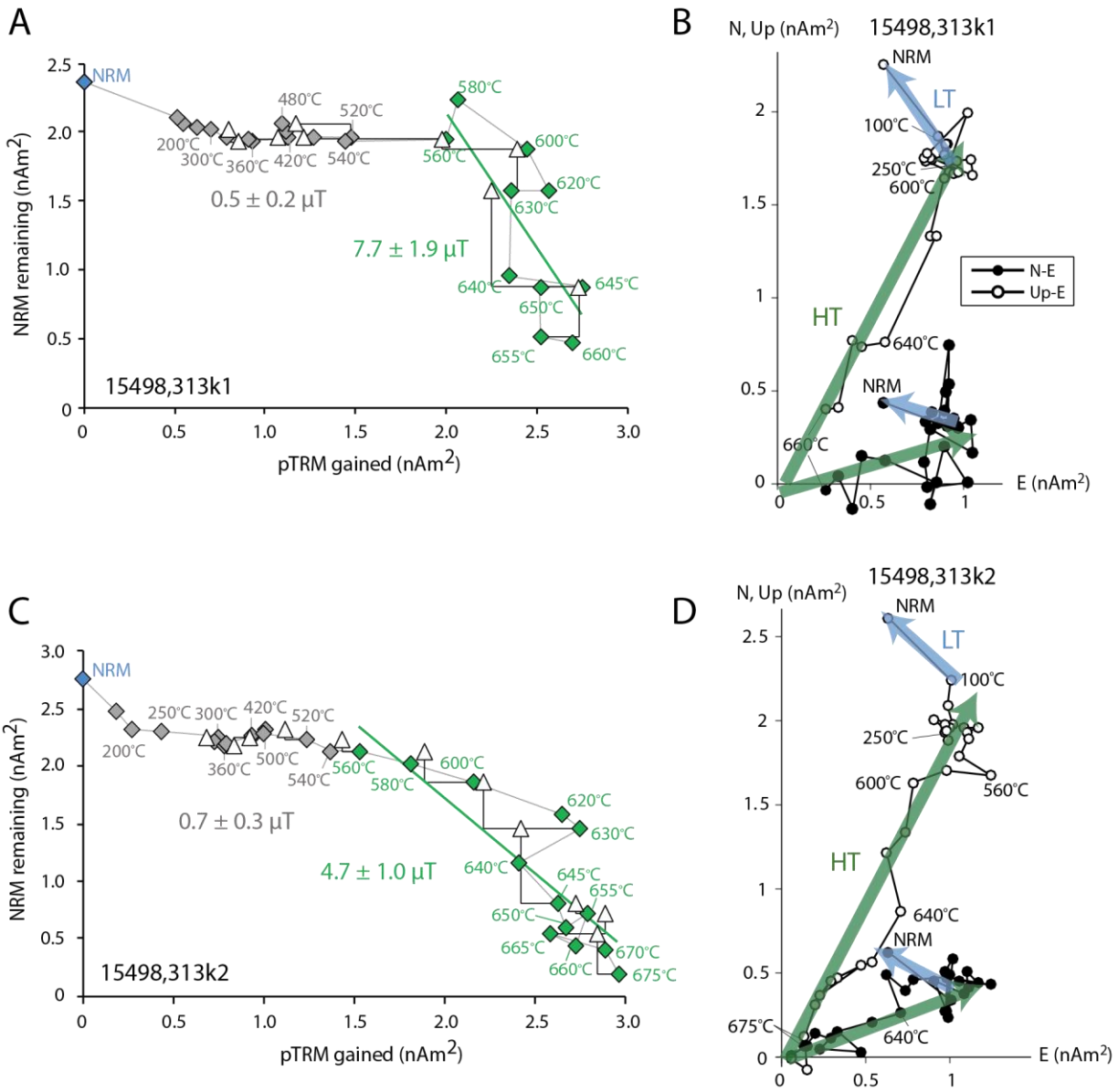

fig. S7. Thellier-Thellier paleointensity experiments for subsamples 15498,313k1 and 15498,313k2 following the IZZI variant. (**A, C**) Arai plots displaying NRM lost during progressive thermal demagnetization (ordinate) versus laboratory partial thermoremanent magnetization (pTRM) gained (abscissa) for subsamples 313k1 and 313k2, respectively. Peak temperatures for selected steps are shown. pTRM checks for alteration are shown using triangles. Paleointensities for unblocking temperature ranges of 250-540°C and ≥560°C are denoted with dark gray and green symbols, respectively. Gray segments link consecutive thermal steps. (**B, D**) Vector endpoint diagrams showing zero field thermal demagnetization steps for subsamples 313k1 and 313k2, respectively. LT and HT components are denoted using blue and green symbols, respectively.

multidomain grains in the sample) and small variations in heating time versus temperature control (which can be important due to the high magnetic viscosity of this sample) may have contributed some zig-zag behavior that is apparent in the Arai plots (see Fig. 7 of the main text and fig. S7) and reflected in the Thellier statistics (table S3a).

3.1.2. ARM and IRM paleointensity experiments. In addition to our Thellier-Thellier paleointensity experiments, we used the nondestructive ARM method to determine paleointensities for the LC, MC, and HC components of several subsamples of 15498 (274d, 282a, 282c, and 287b) (table S3c). We also determined IRM paleointensities for the magnetization components in subsample 282a (table S3d). ARM and IRM paleointensities for the LC components in our subsamples range between ~7-20 μT. MC paleointensities range between ~1-6 μT. The HC components have ARM paleointensities ranging between ~600 nT to 2.8 μT (mean value of 1.5 ± 0.9) that are broadly consistent with our Thellier-Thellier paleointensity determinations.

3.2. AF-based paleointensity fidelity limit tests

AF methods may impart samples with spurious ARM and GRM as demagnetization experiments proceed (*27*). For samples susceptible to these remanences, the magnitude of contaminating ARM or GRM increases with progressively higher AF levels until it eventually overwhelms the remaining NRM. This effect ultimately places a lower limit on the paleointensity value (the paleointensity fidelity limit) that can be accurately recovered from a given sample using AF-based methods (*8, 27*). If the fidelity limit is lower than the retrieved paleointensity value from a given subsample, then the paleointensity determination is considered accurate to within the factor ~2-3 error associated with AF-based paleointensity methods. In this section, we address the robustness of our AF-based paleointensity determinations.

Following Tikoo et al. (*8, 27*), we determined the AF-based paleointensity fidelity limit of subsample 282c. We applied laboratory ARM (as an analog of thermoremanent NRM) that was then AF demagnetized. The ARMs were produced using an AC field of 290 mT and DC fields ranging from 1 to 10 μT [corresponding to TRM-equivalent fields from 0.7 to 7.5 μT, using the TRM/ARM ratio of 1.34 discussed above]. We then used the ARM method to retrieve a paleointensity value for each laboratory-induced magnetization. To ensure that we were only determining paleointensity fidelity limits for grains that could have retained magnetization acquired on the Moon, we only included those AF levels above which any secondary overprints were identified by PCA (i.e., AF levels above 45 mT, the end of the MC component). A sample was considered to have acceptable paleointensity fidelity at fields where either the percentage difference between the retrieved paleointensity and the laboratory field, or the percentage difference between the formal uncertainty (the 95% confidence interval determined using a two-tailed Student's *t*-test) and the laboratory field, were less than 100% (whichever occurred at a higher laboratory DC field value). We found that robust paleointensities could be retrieved from subsample 282c for magnetizing fields <0.7 μT (the minimum applied TRM-equivalent laboratory field in our experiments) (fig. S8). Therefore, the AF-based paleointensities retrieved from this and other 15498 subsamples (ranging from ~600 nT to ~3 μT) are likely accurate to within the systematic errors associated with the ARM and IRM methods.

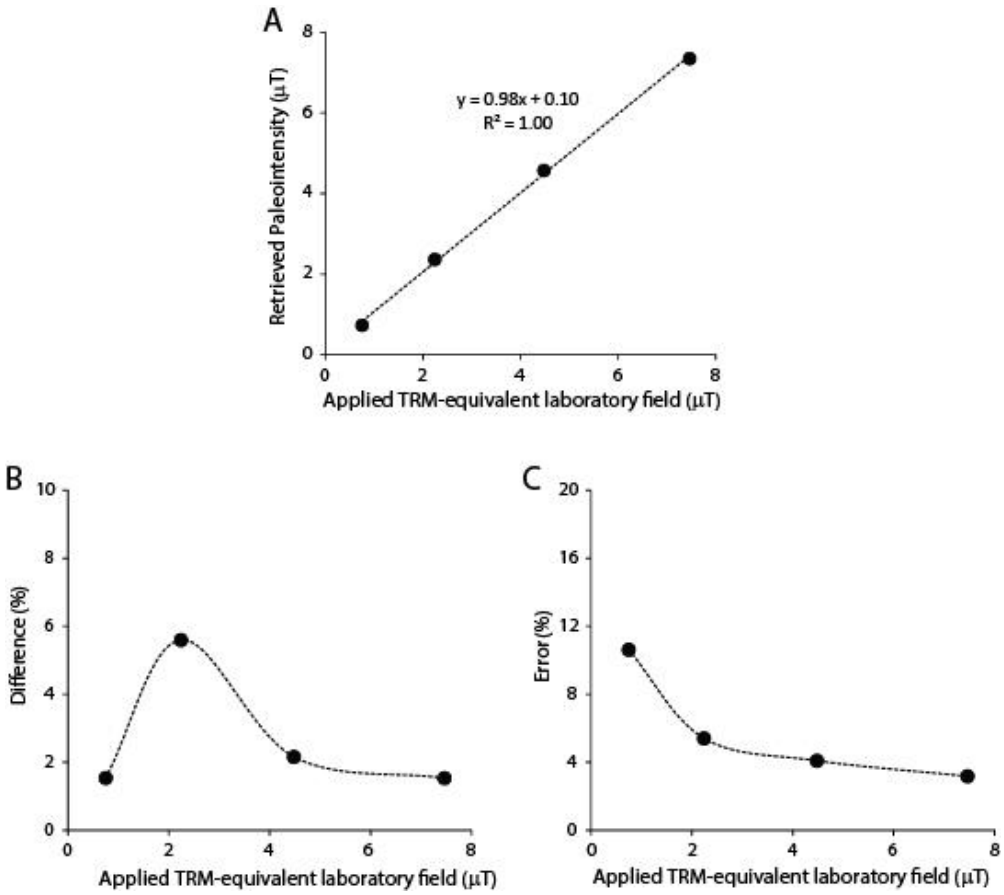

fig. S8. Paleointensity fidelity limit tests for 15498. (**A**) Retrieved paleointensity versus TRM-equivalent applied laboratory field. (**B**) Difference and (**C**) error for recovered paleointensities versus TRM-equivalent applied laboratory field.

section S4. Rock magnetic properties
4.1. Hysteresis and domain state

To determine the average domain state of the magnetic carriers in 15498, we measured hysteresis loops on two pieces of subsample 287b: 287b1 (35 mg) and 287b2 (80 mg). These measurements were made using a Princeton Instruments MicroMag vibrating sample magnetometer housed at the Institute for Rock Magnetism at the University of Minnesota. The bulk hysteresis parameters suggest that the average grain size of the magnetic carriers are superparamagnetic to single-domain: the ratio of saturation remanence to saturation magnetization (M_{rs}/M_s) is 0.08-0.09 and the ratio of remanent coercivity to coercivity (H_{cr}/H_c) is 7.8-9.9 (table S4, Fig. 2 of the main text). These values are consistent with those obtained by a previous study of 15948 (*39*). Despite the existence of observable >1 μm lithic FeNi grains within the breccia matrix (multidomain grains), remanence in 15498 is predominantly carried by the fine grain size (i.e., pseudo single domain and smaller) fraction of ferromagnetic carriers. This may be confirmed by comparing the petrographically estimated metal content of the 15498 matrix to the metal content estimated from the sample hysteresis properties. The visible metal content (multidomain grains) within the 15498 matrix is ~0.01 wt. % (*38*). The M_s of the 15498 matrix is ~0.8 Am^2/kg. Dividing this value by the M_s of kamacite [224 Am^2/kg (*104*)] gives a total metal content of 0.357 wt. % for 15498, which is more than an order of magnitude higher than what is observed via microscopy.

To further characterize the distribution of grain sizes within 15948, we measured room-temperature first order reversal curves (FORCs) on subsamples 287b1 and 287b2 following ref. (*105*). FORC distributions quantify the range of magnetostatic interactions (H_u) vs. the range of microcoercivities (H_c) present in a given sample. Our FORC distributions were calculated over the range H_u = -50 to 50 mT and H_c = 0 to 500 mT. FORC data were processed using the VARIFORC smoothing protocol (*106*) within the FORCinel software package (*107*). The following VARIFORC smoothing factors were used to reduce the data: Sc0 = 3, Sb0 = 2, Sc1 = 4, Sb1 = 4, $\lambda_{horizontal}$ = 0.1, $\lambda_{vertical}$ = 0.1 [see ref. (*106*) for smoothing factor definitions]. In the FORC diagram (fig. S9), the presence of a horizontal ridge extending to high coercivity (>100 mT) along H_u = 0 is consistent with a population of single domain grains within the sample, whereas the cluster near H_c = 0 spread along the H_u axis is consistent with the presence of superparamagnetic grains (*108*).

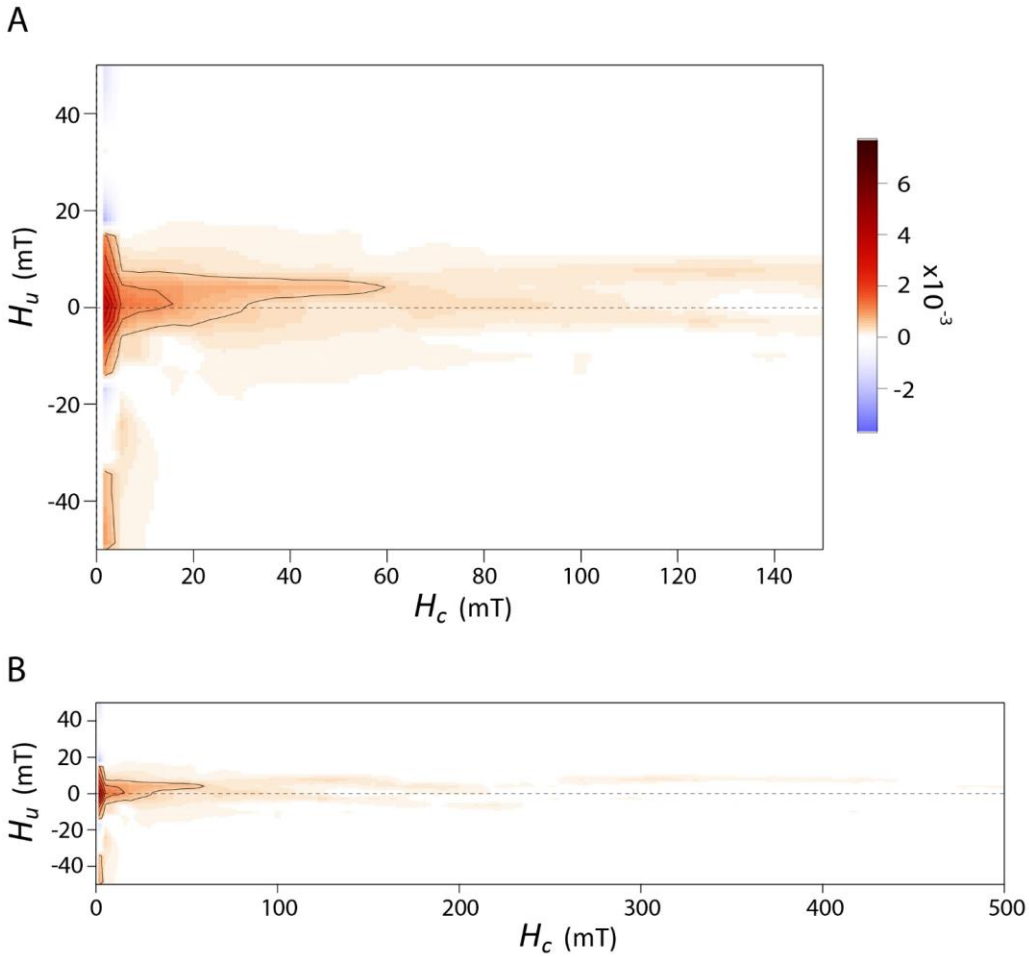

fig. S9. FORC distribution for sample 15498,287b1. FORC diagrams display H_u (degree of magnetostatic interactions) on the ordinate, H_c (coercivity) on the abscissa. The color bar shows the probability density of hysterons belonging to a given H_u and H_c. (**A**) Plot truncated to an H_c range of 0-150 mT. (**B**) Entire FORC distribution (H_c range of 0-500 mT). FORC diagrams were generated using the FORCinel software package (see text for details).

4.2. Other rock magnetic parameters

We performed a series of additional rock magnetic experiments on subsample 15498,282a to assess its magnetic recording properties (fig. S10). First, the sample was progressively given ARM using an ac field of 200 mT and dc bias fields incrementally increasing from 0 to 2 mT. This allows an estimation of the Cisowski *R*-value, an indicator of the extent of magnetostatic interactions (*109*). The final ARM applied (peak AC field = 200 mT, DC field = 2 mT) was AF demagnetized at increasing fields to 290 mT. Using this, we estimated a median destructive field (MDF; i.e., the peak ac field required to reduce the magnetization by half) of ARM of 51 mT. Similarly, we obtained an MDF of IRM value of 52 mT by applying and subsequently stepwise AF demagnetizing a 200 mT IRM to 290 mT (*110*). Finally, IRM was acquired stepwise to 886.5 mT and subsequently AF demagnetized to 290 mT. The acquisition and demagnetization of IRM

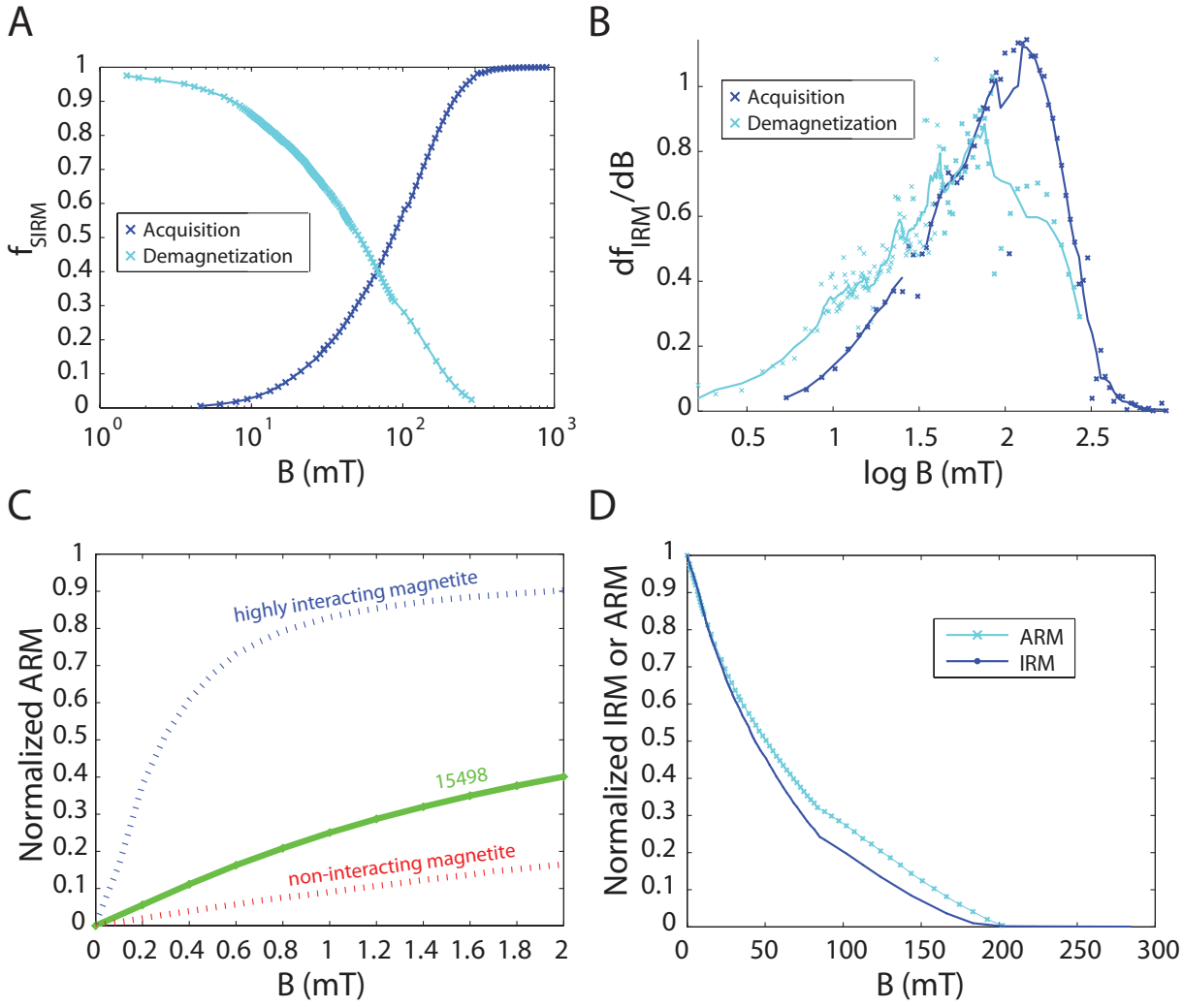

fig. S10. Rock magnetic experiments on 15498,282a. (**A**) Moment-normalized IRM acquisition (dark blue curve) and AF demagnetization (light blue curve). (**B**) Coercivity spectra [i.e., derivative of IRM acquisition (dark blue curve) and AF demagnetization of IRM (light blue curve)]. (**C**) ARM acquisition curve for 15498,282a (green). ARM was acquired in a 200 mT ac field as a function of dc bias field. Upper (blue) dotted curve is that of highly interacting chiton tooth magnetite and lower (red) dotted curve is non-interacting magnetite in magnetotactic bacteria. (**D**) Normalized demagnetization of ARM (ac field = 200 mT, dc field = 2 mT) and IRM (200 mT).

enables the construction of coercivity spectra (*111*). The intersection of the acquisition and demagnetization curves indicates an H_{cr} value of 70 mT. The low Cisowski *R*-value of 0.39 in this subsample and the limited dispersion along the H_u axis in the FORC data for subsample 15498,287b1 (fig. S9) jointly indicate that the extent of magnetostatic interactions between metal grains in the 15498 matrix should be modest. Normalized AF demagnetization curves of laboratory ARM and IRM show that ARM is slightly more resistant to AF demagnetization than IRM across most of the coercivity spectrum, indicating a major population of fine (single domain or pseudo-single domain) magnetic grains. The ferromagnetic grain size range present in 15498 and the high remanent coercivity of this sample indicate that it is capable of providing exceptionally high fidelity paleomagnetic records.

4.3. Possibility of shock remanent magnetization

It is possible that 15498 instantaneously acquired SRM as a result of a meteoroid impact that occurred subsequent to the rock's formation. Although the unfractured nature of the 15948 glassy matrix likely constraints post-formation peak shock pressures to below 3 GPa, shocks at or below this level usually do not leave any petrographic evidence but can still produce magnetization or demagnetize preexisting magnetization [e.g., Gattacceca et al. (*80*)]. To investigate whether SRM could explain the observed NRM in 15948, we conducted a series of PRM acquisition experiments at MIT. Subsample 282a was placed in a cylindrical Teflon cavity which was then filled with polyethilsiloxane fluid and placed in a non-magnetic pressure cell similar to that described in Sadykov (*112*). A coil surrounding the pressure cell applied a 500 μT DC field. Pressure was applied to the cell using a 15 T manual hydraulic press. The sample was kept in-field for at least one minute before the pressure was released. In this study, PRM experiments were conducted for pressures of 0, 0.5, 1, 1.5, and 2 GPa.

Consistent with previous studies of lunar rocks (*4*, *5*, *8*, *50*), we found that PRM was preferentially acquired by a lower coercivity fraction of ferromagnetic grains relative to the HC component in 15498,282a (fig. S6). This suggests that shock demagnetization processes are unlikely to have fully demagnetized the sample (assuming PRM acquisition and pressure demagnetization affect similar coercivity ranges). This is broadly consistent with the pressure demagnetization experiments of Bezaeva et al. (*83*). Therefore, any primary TRM the rock may have acquired during formation should have been mostly retained even if it experienced shocks <3 GPa. Following Shea et al. (*4*), we assumed a linear relationship between demagnetized PRM and pressure to estimate an upper limit on the intensity of a 5 GPa PRM acquired in a 500 μT field and place an upper limit on the fraction of such a PRM remaining after demagnetization to AF levels equivalent to the end of the LC component at AF 4 mT and the end of the MC component at AF 50 mT (see stars in fig. S11). This then allows us to calculate the paleofield intensities that would have been necessary to produce the observed LC, MC, and HC components assuming they are SRM produced by a 5 GPa shock (*4*, *5*, *8*). We find that 870, 7, and 43 μT ambient fields are required to reproduce the NRM intensities for the HC, MC, and LC components, respectively. Lower peak pressures would require higher ambient field intensities to reproduce the NRM. The required field intensity to reproduce the HC component with a 5 GPa PRM is higher than estimates for a lunar dynamo field at any stage in lunar history (maximum value several tens of μT), although it is conceivable that transient impact-generated fields could reach such intensities [e.g., ref. (*31*)]. However, the high coercivity nature of the

NRM in 15498, as well as the slow primary cooling timescale for 15948 (Section 1.3) relative to the duration of impact fields provide evidence against an SRM origin for the HC component. The field intensities required to reproduce the MC and LC components are potentially within range of a dynamo field. However, the non-unidirectional nature of the MC and LC magnetizations in 15948 likely precludes an SRM origin for either of these components.

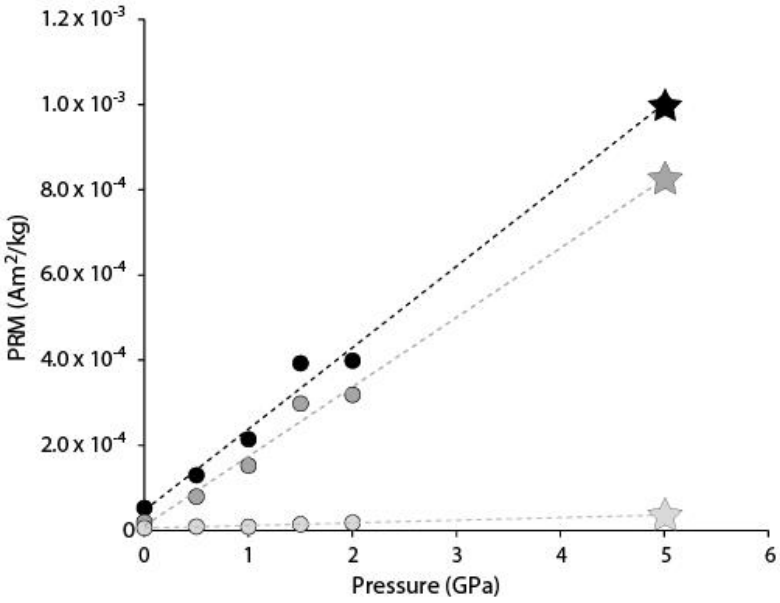

fig. S11. PRM acquisition by 15498 subsample 15498,282a. Shown is the PRM intensity as a function of applied pressure (0, 0.5, 1, 1.5, and 2 GPa) acquired in a 0.5 mT field. Black circles are PRM without any subsequent AF demagnetization. Medium gray and light gray circles are PRM intensity at demagnetization steps AF 4 mT and AF 50 mT that correspond to the end of the LC and MC components, respectively. Dashed lines are best fit linear regression to data. Extrapolation yields a maximum estimate of the PRM acquired at 5 GPa (stars).

4.4. Viscous remanent magnetization

For single domain FeNi grains (which are abundant in this sample), VRM acquired during ~40 years of residence in the terrestrial field is unlikely to remain after the sample has been heated to temperatures in excess of ~125°C, assuming a standard 20 minute laboratory heating experiment (*52*). While the unblocking curves for FeNi presented in ref. (*52*) were calculated for $1/e$ acquisition and decay of remanence, unblocking curves for $1/e^2$ and $1/e^3$ acquisition and decay are very similar [e.g., see treatment for single domain magnetite in Fig. 17 of ref. (*113*)]. Therefore, the peak unblocking temperature estimated for a terrestrial VRM should not depart significantly from ~125°C. Thus, the HC/HT magnetization component in 15498 (that persists to unblocking temperatures well above 500°C) is not residual VRM.

In contrast, the low <250°C maximum unblocking temperature of the LC/LT and MC/MT components strongly favor a VRM origin for these secondary magnetizations, although it is also possible that they may reflect viscously decayed IRM. We conducted a laboratory VRM acquisition and decay experiment on subsample 282c to further test whether the LC/LT and MC/MT magnetization components in our 15498 subsamples could be VRM acquired as the result of 42 years of room-temperature exposure to the terrestrial field. Subsample 282c was placed in the Earth's field in a fixed position for 5 days, 19 hours, and 59 minutes. The subsample was subsequently returned to our magnetically shielded room. After a ~1 minute delay (to load the subsample into the magnetometer), the magnetization was repeatedly measured to determine the intensity of the acquired VRM and its decay rate with time.

We found that a VRM component of magnitude 1.71×10^{-8} Am^2 (equivalent to 445% of the initial NRM) was acquired during the experiment. The decay rate of this laboratory VRM was essentially linear with log(time) (i.e., $R^2 = 1$), allowing us to compute a magnetic viscosity decay coefficient S_d = d(VRM lost)/d[log(time)] of 3.93×10^{-9} Am^2/log(s) (*note*: subsample mass was 113 mg). Although we cannot precisely determine the VRM acquisition and decay rate over 42 years without an equivalently-long experiment, we can extrapolate the linear fit to our week-long experimental data to provide an upper limit for how much of the NRM in 15498 could be produced by VRM. For sample 15498,282c, our linear fit (red line in fig. S12) predicts that the total VRM resulting from 42 years of exposure to the Earth's field [log(time) = 9.1 log(s)] followed by approximately a year of viscous decay in our magnetically shielded room prior to our first NRM measurements [log(time) = 7.6 log(s)] would be ~150% of the total NRM for this subsample. However, note that this value is *significantly overestimated* because the calculation incorrectly assumes that 15498 remained stationary during the 42 years it resided at JSC. Sample 15498 was physically manipulated and rotated multiple times during its residence at JSC as portions of the rock were subdivided and allocated to different investigators over the years.

As we have demonstrated, sample 15498 is highly susceptible to acquisition of VRM. Therefore, it is expected that VRM represents a major contributor to the LC/LT and MC/MT magnetization components in this samples. While VRM is typically expected to exhibit paleointensities similar to that of the terrestrial field (~50 μT), the low paleointensities observed for the LC and MC components (1-20 μT) are easily explained by the rock having been rotated numerous times during its residence on Earth, randomizing the VRM contribution in the sample. The non-unidirectional nature of the LC and MC components across many subsamples is dually consistent with physical rotations during long-term storage and sampling. The compositional heterogeneity of the breccia makes it likely that VRM was acquired at different rates in different

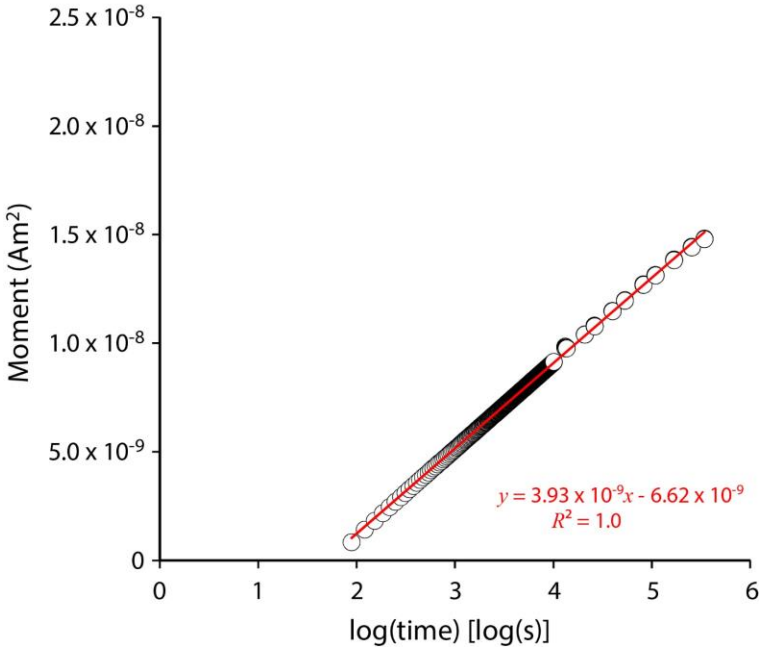

fig. S12. VRM decay experiment on sample 15498,282c. Sample was stored for 1 week in the terrestrial field (~50 μT) and then returned to our shielded room (< 200 nT) where its moment was semi-continuously measured (white circles). Time data can be linearly fit (red line). An equation for the linear fit is shown on the plot with *y* representing the ordinate and *x* the abscissa.

regions of the parent rock [i.e., glassy regions with fine-grained magnetization carriers may be more susceptible to VRM acquisition than regions with greater concentrations of lithic fragments with multidomain grains (*93*)].

4.5. Magnetic anisotropy

The presence of high remanence anisotropy in a sample may lead to incorrectly biased paleomagnetic directions and paleointensities. To assess the extent of magnetic anisotropy in sample 15498, we determined ARM anisotropy ellipsoids for several matrix glass subsamples. In our experiments, ARM was applied with an 85 mT AC field and a 0.01 mT DC field in the three orthogonal directions. The principal axes of the anisotropy ellipsoid were calculated following ref. (*114*). The nature of anisotropy in a given sample can be characterized by the degree of anisotropy, *P*, and the shape factor, *T*. *P* is the ratio of the magnetization acquired along the easy and hard magnetic axes of the anisotropy ellipsoid. *T* is a parameter calculated from the ratios of magnetization acquired along the easy, medium, and hard axes that quantifies

the shape of the anisotropy ellipsoid. $P > 0$ implies an oblate ellipsoid, while $P < 0$ is characteristic of a prolate ellipsoid. Our results indicate that the subsamples of 15498 have modest magnetic anisotropies ($1.08 < P < 1.20$) that will not significantly bias paleodirectional and paleointensity results (table S5). 5 out of 6 measured subsamples had oblate anisotropy ellipsoids ($0.15 < T < 0.70$), while subsample 287a had a prolate ellipsoid ($T = -0.20$).

section 5. $^{40}Ar/^{39}Ar$ and $^{38}Ar/^{37}Ar$ thermochronology

A key question is when the NRM contained in the glass matrix of 15498 was acquired. In this section, we use thermochronology to place temporal constraints on when the breccia formed and acquired primary magnetization and on its subsequent thermal history.

5.1. Analytical results

Whole-rock $^{40}Ar/^{39}Ar$ incremental heating experiments were conducted on an aliquot from the interior of basalt clast 282-1 (table S6). WDS measurements on thin section 15498,299 indicate that the main K-bearing phases within clast 282-1 are a K-rich glass, a feldspathic glass, and pyroxene (table S7). The first 7 degassing steps (comprising the first 40% of ^{39}Ar released from K-rich glass and feldspathic glass) have relatively low apparent ages that monotonically increase from an initial step age of ~980 Ma to ages ranging between 3264 and 3362 Ma in the subsequent 9 degassing steps (i.e., the final 60% of total ^{39}Ar). The weighted mean age from the final 60% of total ^{39}Ar was 3310 ± 50 Ma; uncertainties are 1 standard deviation and include uncertainty in the decay constant and fluence monitor age (see main text Fig. 3). Higher temperature extractions were dominated by gas release from pyroxene as determined from their $^{37}Ar_{Ca}/^{39}Ar_K$ ratio. Given that nearly all Apollo 15 mare basalts formed at ~3.3-3.2 Ga, the 3310 Ma age obtained from the high temperature release steps almost certainly reflects the crystallization age of the clast.

Relatively low apparent ages are also observed in the first 7 steps of the cosmogenic ^{38}Ar exposure age spectrum (~40% of the extracted ^{37}Ar), rising from 153 Ma in the first degassing step to 583-640 Ma in extractions 8-18 (i.e., the final ~60% of total ^{37}Ar). The weighted mean cosmogenic exposure age was ~600 ± 8 Ma (fig. S13).

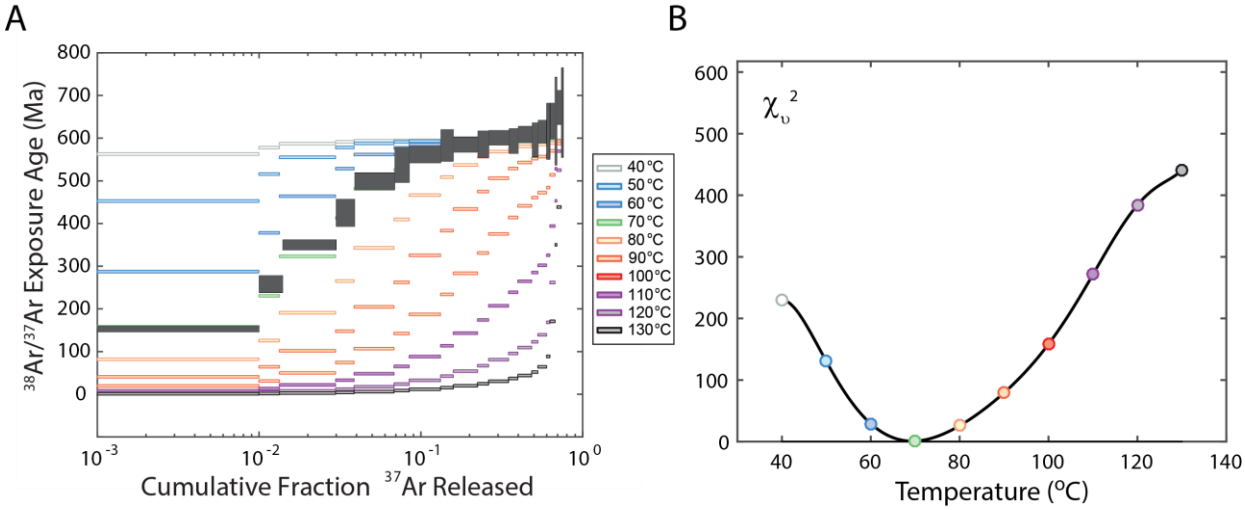

fig. S13. The predicted effects of 600 Ma of solar heating at the lunar surface, calculated using the 15498 MP-MDD model. (**A**) The production and diffusion of $^{38}Ar_{cos}$. The observed exposure ages ± 1 standard deviation (dark gray boxes) are plotted against the cumulative release fraction of ^{37}Ar released (note the log scale). The colored steps are model release spectra calculated using the MP-MDD model parameters and $^{38}Ar_{cos}$ production rates shown in Table S8. For the diffusion of $^{38}Ar_{cos}$, 15498 was subjected to various constant effective daytime temperatures ranging from 40 to 130°C as the best-fit effective mean temperature. (**B**) Reduced chi squared fit statistic for each model, identifying ~69°C as the best-fit effective mean temperature.

5.2. Thermochronological modeling

Discordance in the lower temperature release steps in radiogenic and cosmogenic age spectra generally indicates thermally-activated diffusive loss of $^{40}Ar^*$ and $^{38}Ar_{cos}$, respectively. Prior work demonstrates that discordance in the age spectra of mare basalts is generally produced either by rock burial in a hot impact ejecta blanket, daytime heating on the lunar surface, or a combination thereof (*4*, *5*, *8*, *43*, *115*). Although the precise thermal history that clast 282-1 experienced on the lunar surface is unclear, three events that affected Ar diffusion are certain to have occurred: (*i*) the parent basalt erupted and crystallized during primary cooling, (*ii*) an impact event occurred that incorporated this clast into regolith breccia 15498 and produced the melt glass matrix, (*iii*) impact gardening brought sample 15498 to the lunar surface. Here we describe our thermochronological modeling for estimating the timing of breccia formation (event *ii*) that incorporates likely constraints for (events *i* and *iii*).

5.2.1. Diffusion parameters. Because analyses were conducted on a whole-rock sample rather than mineral separates, neutron-irradiated ^{39}Ar and ^{37}Ar were released from multiple phases (i.e., K-rich glass, feldspathic glass, and pyroxene), with each phase represented by a diversity of crystals and, in turn, diffusion domain sizes. To quantify the diffusion of radiogenic ^{40}Ar ($^{40}Ar^*$) and cosmogenic ^{38}Ar ($^{38}Ar_{cos}$) in our sample in the context of the various possible thermal histories, we constructed multi-phase, multi-domain diffusion (MP-MDD) model fits to the data shown in figs. S13 and main text Fig. 3 (model parameters shown in table S8), following the method of Shea et al. (*4*). Similar MDD models and their application to natural samples with multiple K-bearing phases have been reported by refs. (*4*, *5*, *8*, *65*, *116*). We calculated apparent ^{39}Ar and ^{37}Ar diffusion coefficients (see Arrhenius plot in fig. S14) from the whole-rock stepwise release data (table S6) following ref. (*117*) using procedures described in refs. (*4*, *5*, *65*). We then used the diffusion coefficient values (table S8) to explore a variety of possible thermal histories.

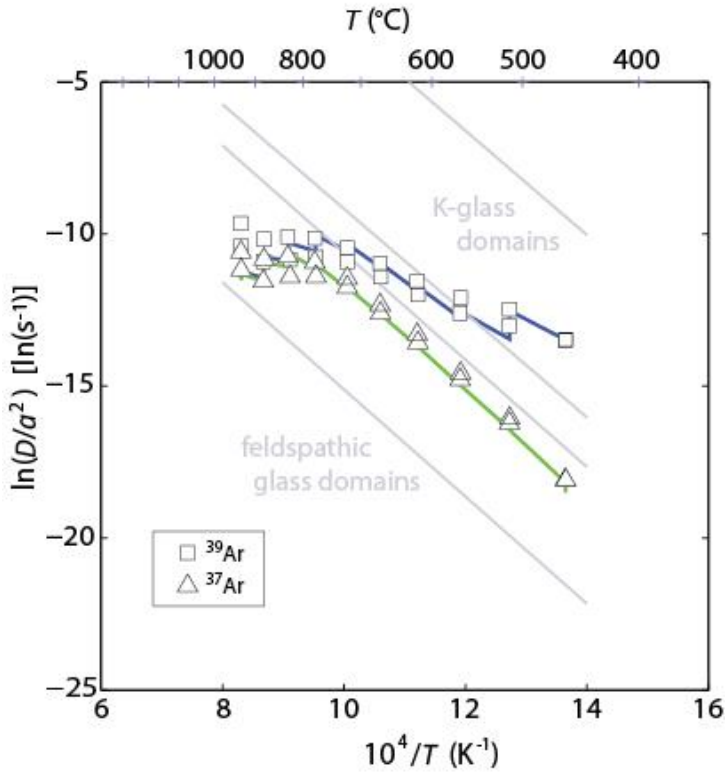

fig. S14. Arrhenius plots with calculated diffusion coefficients for ^{39}Ar and ^{37}Ar released during the first 20 release steps. Points are diffusion coefficients, D, divided by the square of the effective diffusive length scale, *a*. ^{39}Ar is represented by squares and blue lines. ^{37}Ar is represented by triangles and green lines. *T* is the controlled temperature during the laboratory extraction. Blue and green lines represent MP-MDD model fits to the ^{39}Ar and ^{37}Ar data using our laboratory heating schedule and the 4 specified domain sizes and gas fractions listed in table S8. Each temperature step was run twice. The grey lines indicate the input diffusion kinetics of each of the 4 model domains.

5.2.2. Constructing potential thermal histories. We first explored time-temperature conditions required to reproduce the $^{38}Ar/^{37}Ar$ cosmogenic exposure age spectrum to place initial constraints on the daytime heating temperatures experienced by the rock. As seen in fig. S13, discordance in the exposure age spectrum is best explained by daytime heating at an effective mean (i.e., square pulse) temperature of 69°C after 600 Ma (its cosmic ray exposure age), which corresponds to a peak temperature during the lunation cycle of ~90°C. This value slightly underestimates maximum daytime temperatures of ~98°C measured at the Apollo 15 landing site (*118*). This suggests that 15498 was shallowly buried in the regolith for some of its near surface exposure history (i.e., it was partially buffered from surface temperature variations but shallow enough to accumulate cosmogenic nuclides). Note that regolith at depths >10 cm remain at a relatively constant -23°C at the Apollo 15 landing site (*119*), whereas production rates for $^{38}Ar_{cos}$ vary in the top ~2 m of the regolith and decrease exponentially down to ~10 m with an e-folding length of ~120 cm (assuming a regolith density of 1500 kg m^{-3}) (*120*).

We subsequently explored a range of time-temperature conditions to attempt to reproduce the $^{40}Ar/^{39}Ar$ age spectrum given our knowledge of the breccia clast's history. We assumed that the clast formed at 3310 Ma (table S9) and that it subsequently experienced thermal excursions from breccia formation (sometime after 3310 Ma) and daytime heating from 600 Ma (the cosmogenic exposure age) to the present (fig. S15). For simplicity, we assumed there was no diffusive loss of Ar between 3310 Ma and the time of breccia formation. We modeled impact-related time-temperature conditions according to the process for breccia formation previously described in Section 1.2. We assumed that during the breccia formation event, the clast's temperature increased from an initial value of 100°C to a set of clast-melt equilibrium temperatures ranging

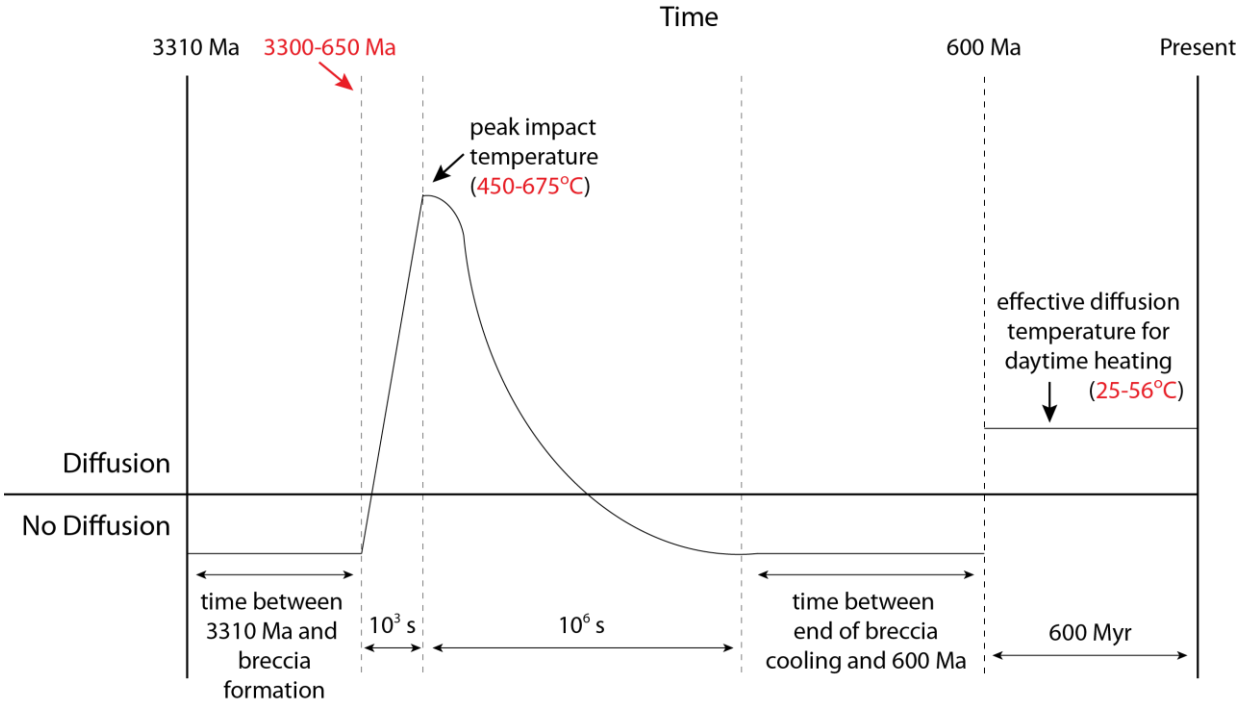

fig. S15. Schematic depicting time-temperature conditions underlying our thermochronological models. Independent variables in our models such as the timing of breccia formation, peak temperatures experienced by the clast during breccia formation, and effective daytime heating temperatures are indicated by red text.

between 450°C and 675°C over a span of 1000 s. To model the subsequent conductive cooling of the consolidated breccia to surrounding rocks, we idealized the breccia as a tabular channel of width 20 cm [i.e., roughly twice the current diameter of the rock; this larger size allows for expected impact-induced fracturing of the parent rock after it formed (given its long ~600 Ma residence near the lunar surface) (*121*)] and infinite length. Following Delaney (*122*), we constructed cooling curves starting from the peak equilibration temperature and terminating 10^6 seconds later, by which time the rock would have cooled down to temperatures that would not produce significant Ar diffusion [e.g., in 10^6 seconds, the breccia would have cooled down to just 2˚C from a given peak equilibration temperature of 623 ˚C into a surrounding regolith of -35˚C; note that the surrounding regolith temperatures may have been anywhere between approximately -200˚C and 80˚C, depending on the regolith depth at which 15498 formed (*118, 123*)]. We assumed that there was no diffusive loss of Ar between the end of breccia cooling and 600 Ma. We included diffusive loss of Ar due to daytime heating from 600 Ma to the present in our composite thermal history.

It is possible that the emplacement of the impact glass spatter on the exterior of the rock contributed to a transient heating of the exterior regions of the rock. However, the glass emplacement is unlikely to have affected the clast that we conducted the thermochronology modeling on for the following reasons: this clast (from parent chip 282) was located about 2 cm from the nearest incidence of impact melt glass splatter, and the spatter thickness at that location was <1-2 mm. This thin glass would have cooled very rapidly [we calculate an upper limit *e*-folding cooling timescale of $l^2/D = 4$ s for a 2 mm thick (l) rind assuming a typical silicate rock thermal diffusivity (D) of 10^{-6} m^2 s^{-1}]. Given this low glass thickness and fast cooling timescale, heating related to emplacement of the glass spatter would not have penetrated far into the interior of the rock where the modeled clast was located.

We ran a series of thermochronology models that varied the timing and peak equilibration temperature associated with the breccia-forming impact between 3300 Ma and 650 Ma. Thermal models using the 69°C effective mean daytime heating temperature inferred from the cosmogenic exposure spectrum produced too much diffusion in the initial laboratory heating steps and hence could not be reconciled with our sample's $^{40}Ar/^{39}Ar$ age spectrum (fig. S16). The best-fit daytime heating temperature varied with modeled impact age such that older impact events required higher mean daytime heating temperatures to match the age spectrum [~56°C for a 3300 Ma impact and ~25°C for a 650 Ma impact (table S10)]. The cosmogenic exposure age requires 15498 to be near the surface (<3 m) for the past 600 Ma. Directly at the surface, the temperature fluctuates between about -200 ˚C and about 80 ˚C at the Apollo 15 landing site (*118*). At depths ranging between 50-150 cm, the lunation temperatures are limited to -23 ± 5˚C (*123*). Therefore, being shadowed by any nearby boulders for some time or shallow burial in the regolith could easily permit 15498 to exhibit the surface temperatures (56-23˚C) inferred from our thermochronology models.

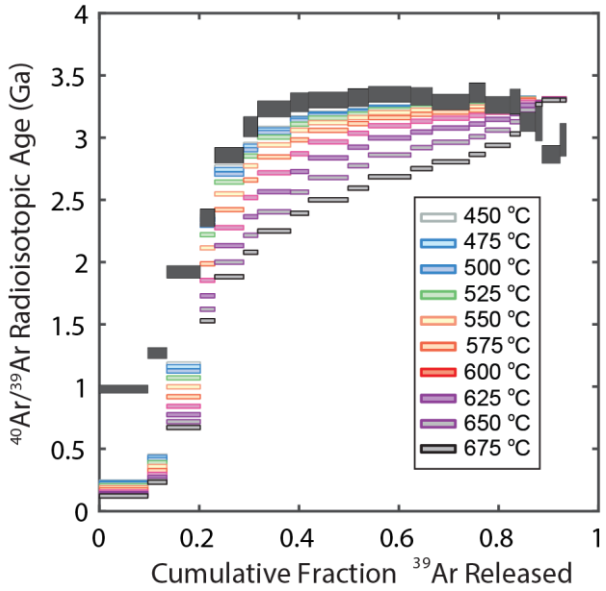

fig. S16. 15498 MP-MDD model predictions for diffusion of ^{40}Ar* resulting from impact heating at 2000 Ma (to temperatures ranging between 450° and 675°C), followed by daytime heating to an effective mean temperature of 69°C after 600 Ma. The clast crystallization age was assumed to be 3310 Ma. The observed ages ± 1 standard deviation (dark gray boxes) are plotted against the cumulative release fraction of ^{39}Ar released. The colored steps are model release spectra calculated using the MP-MDD model parameters shown in Table S8.

Therefore, we fixed the daytime heating temperature to whatever temperature produced the best-fit ordinate-intercept of the age spectrum (between 25°C and 56°C, depending on the model) and instead varied the impact age and the peak temperatures experienced by the clast during breccia formation. Using these assumptions, we were able to exclude breccia-forming impacts occurring at or before 3000 Ma because such models either do not produce enough diffusive loss in the lower-temperature release steps (i.e., those between the 20% and 30% ^{39}Ar release steps of the sample age spectrum) or the models produce too much diffusion at the higher temperature release steps, lowering the model crystallization age (i.e., the >30% ^{39}Ar release steps) (fig. S17). Accordingly, impact ages ≥3000 Ma also produced the highest reduced chi squared misfits (χ^2_u > 7) to the entire sample age spectrum (table S10). Impact ages close to the cosmogenic exposure age (e.g., 650 Ma) produce non-unique best-fit solutions and do not reproduce the form of the ^{40}Ar/^{39}Ar age spectrum as well as other impact age models (fig. S18). Models for impacts occurring between 2500 Ma and 1000 Ma had the lowest misfits ($5 < \chi^2_u < 6$) when employing peak impact heating temperatures ranging from 540-560°C. These peak temperatures are close to the breccia equilibrium temperature inferred from measurements of the crystallinity of the matrix glass (see Section 1.2), which gives confidence in both results.

Because the reported χ^2_u misfit values were calculated from the entire age spectrum, they mitigate the observed differences between the model age spectra and the sample age spectrum in the low temperature release fraction where discordance manifests. We attempted to further

refine the breccia formation age by plotting the best fit model age spectrum from each modeled impact age and comparing the model release steps to the path of the sample release steps for the low temperature fraction most affected by impact heating (i.e., steps 2-6, ranging between ~10-30% of the total ^{39}Ar release). We found that 5 out of 5 model release steps fell on the sample release path for breccia formation occurring at 1000 Ma, 4 out of 5 model release steps matched the sample path for breccia formation occurring at 1500-3000 Ma, and only 3 out of 5 model release steps matched for breccia formation at 3300 Ma (see Fig. 3 of the main text.). Our thermochronometry models provide an constraint on the formation age which is entirely independent from the previously measured trapped ^{40}Ar/^{36}Ar breccia lithification age of 1.32 ± 0.43 (*45*). Remarkably, both findings strongly suggest that the glass matrix of breccia 15498 formed and acquired TRM at ~1-2.5 Ga.

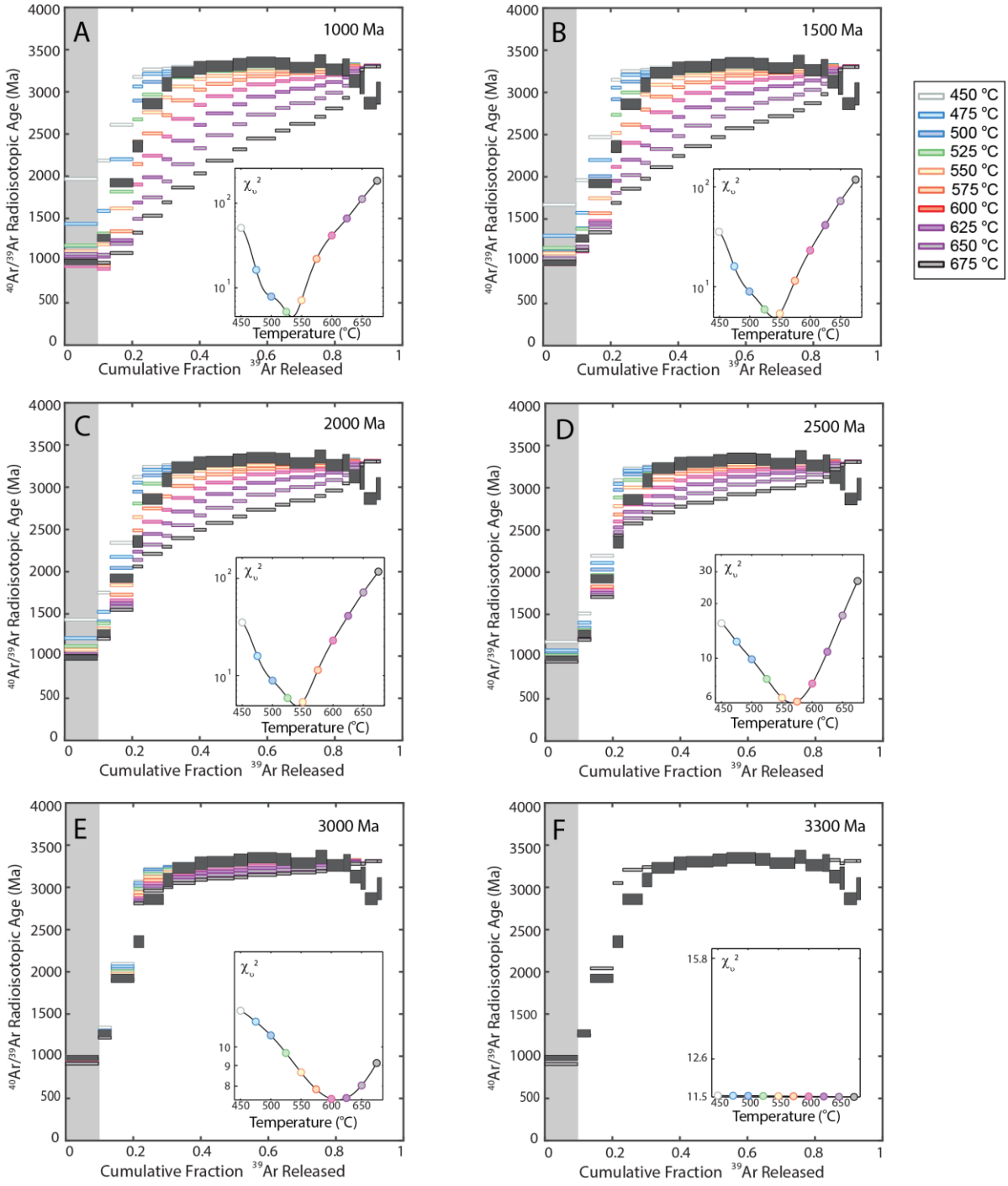

fig. S17. 15498 MP-MDD model predictions for diffusion of ^{40}Ar* resulting from impact heating at various times in lunar history (to temperatures ranging between 450° and 675°C), followed by daytime heating to effective mean temperatures ranging between 35° and 56°C after 600 Ma. (**A**) 1000 Ma, (**B**) 1500 Ma, (**C**) 2000 Ma, (**D**) 2500 Ma, (**E**) 3000 Ma, (**F**) 3300 Ma. The crystallization age was assumed to be 3310 Ma. The observed ages ± 1 standard deviation (dark gray boxes) are plotted against the cumulative release fraction of ^{39}Ar released. The colored steps are model release spectra calculated using the MP-MDD model parameters shown in table S8. Insets show reduced chi squared fit statistics for each model.

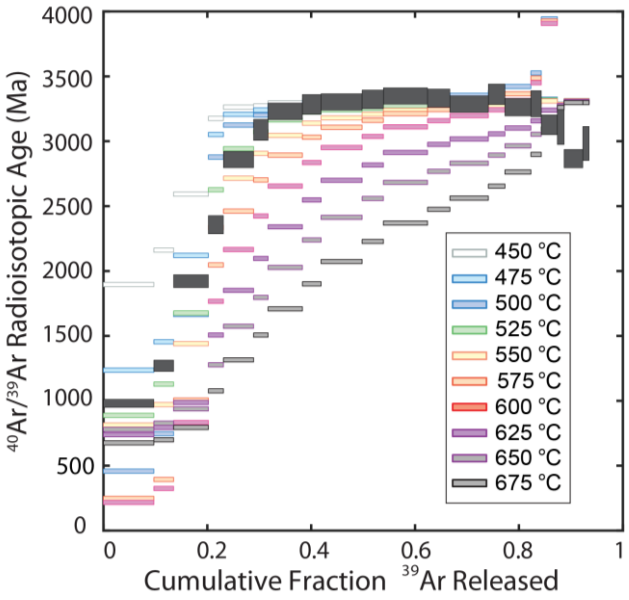

fig. S18. 15498 MP-MDD model age spectra incorporating diffusion of $^{40}Ar^*$ resulting from impact heating at 650 Ma (to temperatures ranging between 450° and 675°C), followed by daytime heating to an effective mean temperature of 25°C after 600 Ma. The clast crystallization age was assumed to be 3310 Ma. The observed ages ± 1 standard deviation (dark gray boxes) are plotted against the cumulative release fraction of ^{39}Ar released. The colored steps are model release spectra calculated using the MP-MDD model parameters shown in table S8. χ^2_u misfit values were not amenable to curve fitting. The minimum χ^2_u misfit value from this set of models was obtained from the model utilizing a peak impact heating temperature of 525 °C.

table S1. WDS measurements of metal grains in 15498 thin sections 298 and 299.

Sample	Occurrence	#	Fe	Ni	P	Co	S	Si	Al	W	Ti	O	Cr	Total
15498,298	lithic fragment in glass	1	91.25	2.55	0.00	1.12	0.01	0.10	0.88	0.00	0.16	1.90	0.07	98.04
	isolated in glass	2T1	90.63	2.67	0.20	1.30	0.54	0.00	1.14	0.00	0.02	1.71	0.02	98.24
	isolated in glass	2T2	92.12	2.70	0.27	1.38	0.47	0.00	0.60	0.00	0.02	1.10	0.00	98.67
	lithic fragment in glass	3T1	89.06	5.33	0.01	1.95	0.03	0.00	0.96	0.00	0.03	1.66	0.00	99.03
	lithic fragment in glass	3T2	89.24	5.26	0.00	1.98	0.05	0.00	1.14	0.00	0.04	1.67	0.03	99.40
	lithic fragment in glass	3T3	87.91	6.17	0.00	1.84	0.03	0.27	0.75	0.00	0.03	1.60	0.04	98.64
	within basalt clast	4	89.30	3.76	0.00	1.23	0.00	0.00	2.96	0.00	0.06	3.22	0.04	100.58
	within basalt clast	5	89.82	3.86	0.00	2.02	0.03	0.00	0.94	0.00	0.17	1.60	0.13	98.57
	within basalt clast	6T1	92.23	3.06	0.00	1.16	0.01	0.00	1.21	0.00	0.07	1.78	0.00	99.52
	basalt/glass boundary	6T2	92.72	3.12	0.01	1.24	0.03	0.00	0.84	0.00	0.02	1.29	0.03	99.30
	basalt/glass boundary	6T3	92.23	3.03	0.00	1.23	0.03	0.00	0.79	0.00	0.07	1.51	0.03	98.93
	basalt/glass boundary	7T1	85.59	8.63	0.00	1.51	0.03	0.00	1.09	0.00	0.04	1.56	0.02	98.47
	basalt/glass boundary	7T2	86.30	7.20	0.03	1.54	0.00	0.00	1.30	0.00	0.07	2.10	0.04	98.57
15498,299	lithic fragment in glass	1T1	76.61	19.36	0.03	2.09	0.05	0.00	0.56	0.00	0.02	1.11	0.04	99.87
	lithic fragment in glass	1T2	75.79	19.33	0.02	1.99	0.01	0.00	0.39	0.13	0.01	1.07	0.03	98.77
	lithic fragment in glass	1T3	75.60	19.27	0.01	2.00	0.04	0.00	0.37	0.00	0.04	0.94	0.01	98.28
	lithic fragment in glass	2T1	83.35	12.55	0.36	1.17	0.07	0.00	0.27	0.00	0.03	0.75	0.05	98.59
	lithic fragment in glass	2T2	82.71	12.79	0.34	1.18	0.04	0.00	0.36	0.00	0.02	0.63	0.00	98.07
	lithic fragment in glass	4T1	86.39	8.52	0.02	1.56	0.06	0.00	1.03	0.00	0.00	1.41	0.02	99.01
	lithic fragment in glass	4T2	87.19	8.77	0.02	1.59	0.03	0.00	0.52	0.00	0.00	0.92	0.01	99.05
	lithic fragment in glass	4T3	87.94	8.74	0.03	1.48	0.04	0.00	0.42	0.00	0.03	1.05	0.02	99.75
	lithic fragment in glass	4T4	87.52	8.84	0.02	1.56	0.06	0.00	0.79	0.00	0.00	1.47	0.01	100.26
	lithic fragment in glass	4T5	87.66	8.42	0.02	1.56	0.02	0.00	0.46	0.00	0.02	1.25	0.02	99.43
	lithic fragment in glass	4T6	87.61	8.83	0.03	1.55	0.04	0.00	0.58	0.00	0.01	1.10	0.04	99.79
	lithic fragment in glass	4T7	87.54	8.04	0.02	1.53	0.02	0.00	0.58	0.00	0.01	1.22	0.00	98.97
	lithic fragment in glass	4T8	87.37	8.44	0.01	1.59	0.03	0.04	0.32	0.00	0.05	1.13	0.03	99.01
	lithic fragment in glass	5T1	91.74	3.78	0.00	1.44	0.03	0.00	0.50	0.00	0.02	1.13	0.02	98.67
	lithic fragment in glass	5T2	90.96	3.94	0.03	1.41	0.04	0.00	0.46	0.00	0.03	0.85	0.02	97.74
	lithic fragment in glass	5T3	91.13	3.75	0.01	1.42	0.05	0.00	0.28	0.00	0.10	0.81	0.04	97.57
	lithic fragment in glass	5T4	91.68	3.67	0.00	1.37	0.02	0.00	0.37	0.00	0.04	1.08	0.10	98.33
	lithic fragment in glass	6	93.10	2.71	0.02	1.60	0.00	0.00	0.32	0.00	0.12	0.67	0.00	98.55
	lithic fragment in glass	7	88.78	6.46	0.02	1.78	0.02	0.00	0.45	0.00	0.07	0.99	0.05	98.62

Note: The first column contains the sample name. The second column describes the petrographic setting of each measured metal grain. The third column contains a number corresponding to the grain measured if there was only one data point per grain or the transect measured across a single grain if multiple points were measured (when number is preceded by a "T"). The fourth through fourteenth columns contain the elemental abundances in mass percent for Fe, Ni, P, Co, S, Si, Al, W, Ti, O, and Cr, respectively. The fifteenth column contains the sum (in percent) of the measured elemental abundances.

table S2A. NRM components identified for interior matrix glass subsamples of 15498.

Sample, Component	Mass (mg)	AF or Unblocking Temperature Range Fit	Type	Dec., Inc. (°)	MAD, MADd (°)	DANG (°)	*N*	Orientation: strike, dip (°)
274d	165							90, 90
LC		1.5-5 mT	L	243.9, -0.8	3.4		8	
MC		5-48 mT	L	173.1, 42.9	20.7		64	
HC		48-85 mT	AL	73.8, -24.5	4.2, 18.8	12.8	38	
282a	89							0, 90
LC		NRM-4 mT	L	92.8, -24.7	2.5		7	
MC		4-50 mT	L	133.7, -5.2	19.1		68	
HC		50-85 mT	AL	52.6, -41.9	0.7, 8.3	4.6	36	
282b	85							0, 180
LC		NRM-6.5 mT	L	230.9, 20.2	14.3		12	
MC		6.5-43 mT	L	265.3, 21.4	9.2		56	
HC		43-85 mT	AL	34.6, -26.1	4.5, 29.8	53	43	
282c	113							0, 90
LC		NRM-5 mT	L	67.9, 11.7	8.9		4	
MC		5-45 mT	L	263.9, 15.5	2.4		13	
HC		45-85 mT	AL	42.7, -28.9	1.7, 21.6	13.1	9	
282t	100							90, 90
LT		NRM-125ºC	L	120.5, 44.7	11.2		5	
MT		125-200ºC	L	288.6, -80.0	10.4		4	
HT		200-785ºC	AL	38.4, -50.0	6.2, 17.7	1.5	24	
287b	123							270, 90
LC		NRM-6 mT	L	195.4, 15.2	3.2		10	
MC		6-41 mT	L	171.5, 12.9	18.4		55	
HC		41-85 mT	AL	47.3, -58.9	5.3, 37.1	30.7	45	
313e	104							180, 90
LT		NRM-100°C	L	311.1, -36.6	0		2	

HT		100-680°C	AL	68.2, -64.4	2.8, 7.6	0.4	28	
313h	102							0, 90
LT		NRM-100°C	L	227.0, -72.7	0		2	
HT		100-675°C	AL	56.1, -58.7	3.7, 8.4	1.3	27	
313j	139							0, 90
LC		NRM-30 mT	L	280.9, -43.9	11.3		16	
HT		100-665°C	AL	55.0, -56.4	3.8, 11.4	2.8	25	
313k1	51							180, 90
LT		NRM-100°C	L	290.5, -50.3	0		2	
HT		100-660°C	AL	74.5, -61.3	5.8, 17.7	7.1	24	
313k2	40							180, 90
LT		NRM-100°C	L	307.7, -38.3	0		2	
HT		100-675°C	AL	67.2, -59.6	4.6, 10.5	4.53	27	
314a	127							0, 90
MT		NRM-450°C	L	75.3, 7.1	11.3		12	
HT		450-665°C	AL	55.8, -37.3	5.3, 12.3	2.9	16	

Note: The first column contains the subsample and component names. The second column contains the subsample mass. The third column contains the AF levels or unblocking temperature range corresponding to each magnetization component. The fourth column contains the type of PCA fit (L = linear fit not forced through the origin, AL = linear fit forced through the origin). The fifth column contains the declination and inclination of the fit. The sixth column contains the MAD of the corresponding PCA fit, followed by the MAD of an unconstrained (i.e., not forced through the origin) linear PCA fit (defined here as MADd) determined for the same AF levels. The seventh column contains the DANG value. The eighth column contains the number of data points used to determine each fit. The ninth column contains the strike and dip of each subsample's top face as they were oriented in our magnetometer for measurements. Following demagnetization experiments, the data were rotated into a common reference frame.

table S2B. NRM components identified for peripheral matrix glass subsamples of 15498.

Sample, Component	Mass (mg)	AF or Unblocking Temperature Range	Type	Dec., Inc. (°)	MAD, MADd (°)	DANG (°)	*N*	Orientation: strike, dip (°)
274a	103							90, 90
LC		1.5-6.5 mT	L	197.3, 15.2	2.4		11	
MC		6.5-14.5 mT	L	179.1, 16.0	16.4,		10	
274t	86							0, 90
LT		NRM-200ºC	L	125.5, 15.3	16.8		4	
MT		200-250ºC	L	118.5, -34.5	17.3		5	
MT2		250-550ºC	AL	103.1, -29.0	10.3, 26.6	65.3	7	
274v3	55							270, 90
LC		NRM-3.5 mT	L	103.8, -15.2	7.3		7	
MC		3.5-20 mT	L	151.3, -13.5	6.4		34	
MT		150-300°C	AL	21.6, -52.1	12, 14.9	20.8	4	
274v5	41							270, 90
LC		NRM-5.5 mT	L	76.2, -7.0	4.5		11	
MC		5.5-16.5 mT	L	223.8, -11.6	18.1		23	
MC2		17-29 mT	L	191.1, 6.9	26		21	
MT		29 mT-300°C	L	47.0, -22.6	42.7		17	
274v6	43							270, 90
LT		NRM-200°C	L	75.4, 30.7	4.1		4	
274v8	66		L					270, 180
LT		NRM-200°C	L	84.4, 17.1	6.3		4	
MT		200-360°C	L	303.0, 9.0	18		5	
274v9	70							270, 180
LC		NRM-7 mT	L	259.6, 4.2	5.2		14	
MC		7-20 mT	L	88.3, 2.3	18		27	
287a	164							180, 90
LC		NRM-2.5 mT	L	296.1, -27.3	5.3		4	
MC		5-37 mT	L	109.1, -17.4	6.4		53	
MC2		37-85 mT	AL	89.0, -0.7	10.8, 34.9	9.1	57	

Note: All columns defined as in table S2a.

table S2C. Fisher mean component directions derived from 15498 data in table S2A.

Component	Dec. (°)	Inc. (°)	α_{95} (°)	κ	*N*
HC/HT	54.2	-48.2	9.5	19.9	12

Note: All subsamples were mutually oriented. The first column gives the name of the component used to compute the mean direction. The second and third columns contain the declination and inclination of the mean direction. The fourth column gives the 95% angular confidence interval (α_{95}). The fifth column gives the Fisher precision parameter (κ). The sixth column gives the number of subsamples used in the calculation.

table S3A. Thellier-Thellier paleointensity determinations for 15498 subsamples.

Sample	Temperature Range	DANG (°)	MAD (°)	*N*	FRAC	*β*	GAP-MAX	DRATS (%)	*q*	Paleointensity (μT)
313e	250-540°C	78	33	11	0.18	0.43	0.22	71	1.5	0.2 ± 0.1
	560-680°C	2.1	7.3	14	0.64	0.11	0.16	17	5.8	5.1 ± 0.6
313h	250-540°C	72	35	11	0.23	0.38	0.18	45	0.6	0.8 ± 0.3
	560-675°C	3.3	6.2	13	0.57	0.14	0.15	63	4.1	6.5 ± 0.9
313j*	250-540°C	16	44	11	0.21	0.12	0.23	34	0.3	0.8 ± 0.1
	560-665°C	3.3	12	11	0.80	0.29	0.27	36	1.1	3.1 ± 0.9
313k1	250-540°C	76	42	11	0.22	0.35	0.19	38	2.3	0.5 ± 0.2
	560-660°C	5.5	12	10	0.51	0.25	0.19	8	1.2	7.7 ± 1.9
313k2	250-540°C	85	45	11	0.29	0.44	0.13	35	2.5	0.7 ± 0.3
	560-675°C	3.8	11	13	0.51	0.20	0.13	46	2.7	4.7 ± 1.0
314a	250-450°C	49	23	7	0.32	0.40	0.17	99	0.1	7.1 ± 2.9
	480-665°C	3.4	13	15	0.38	0.11	0.10	42	2.4	3.8 ± 0.4

Note: The first column contains the sample. The second column contains the temperature range used in the paleointensity regression calculation. The third column contains the DANG value of the fit. The fourth column contains the unconstrained MAD value of the fit. The fifth column contains the number of NRM-pTRM steps used in the regression. The sixth through tenth columns contain the following Thellier statistics: FRAC value, *β,* GAP-MAX, DRATS parameter, and *q*. The eleventh column contains retrieved Thellier-Thellier paleointensity values. Uncertainties on paleointensity values are determined from the standard error (σ_b) of the least squares slope of the HT component on the Arai diagram, following ref. (*124*).
*Subsample 313j was AF-pretreated to 30 mT prior to thermal demagnetization experiments.

table S3B. Comparison of pTRM and pTRM check values for 15498 subsamples.

Preceding pTRM (°C)	pTRM check (°C)	% between pTRM and pTRM checks					
		313e	**313h**	**313j**	**313k1**	**313k2**	**314a**
360	300	43.4	27.1	9.9	12.8	9.1	46.9
420	360	16.8	15.5	10.6	8.0	6.9	12.7
480	420	13.2	13.4	14.5	4.6	0.3	51.4
520	480	12.0	18.8	7.3	7.6	11.1	22.5
560	520	27.2	1.1	3.7	17.2	15.5	9.5
600	560	7.1	47.2	19.3	1.3	23.6	25.6
630	600	1.9	24.8	10.7	2.5	2.5	10.2
645	630	0.4	12.0	7.6	4.8	11.7	6.9
655	645	1.1	2.5	2.9	0.7	3.7	2.1
665	655	6.3		4.4		3.6	1.6
675	665	2.8				10.0	
680	675	0.9					

Note: The first column contains the temperature of the thermal demagnetization step preceding the pTRM check. The second column contains the temperature of the pTRM check. The third through eighth columns contain the percentage difference between the pTRM check values and the previously applied pTRM at the same temperature for subsamples 313e, 313h, 313j, 313k1, 313k2, and 314a, respectively.

table S3C. ARM paleointensity determinations for 15498 subsamples.

Subsample, Component	AF levels included (mT)	ARM bias field (μT)	Paleointensity
274d			
LC	NRM-5	50	7 ± 0.4 μT
MC	5-48	50	610 ± 70 nT
HC	48-85	50	770 ± 150 nT
282a			
LC	NRM-4	50	9.8 ± 3.5 μT
MC	4-50	50	1.1 ± 0.1 μT
HC	50-85	50	2.8 ± 0.3 μT
282c			
LC	NRM-5	3	9.8 ± 8.4 μT
MC	5-45	3	5.8 ± 1.7 μT
HC	45-85	3	1.1 ± 0.2 μT
287b			
LC	NRM-6.5	50	20 ± 3.9 μT
MC	6.5-43	50	1.3 ± 0.2 μT
HC	43-85	50	1.3 ± 0.3 μT

Note: The first column identifies each subsample and specifies whether the data presented for each row refers to a low coercivity (LC), medium coercivity (MC), or high coercivity (HC) magnetization component. The second column contains the AF range used for the paleointensity determination. The third column contains the intensity of the dc bias field to produce the ARM (along with a 290 mT ac field). The fourth column contains paleointensity values. Uncertainties are 95% confidence intervals determined using a two-tailed Student's *t*-test. All paleointensity values are computed assuming the components are thermally activated remanences.

table S3D. IRM paleointensity determinations for 15498 subsamples.

Subsample, Component	AF levels included (mT)	Paleointensity
282a		
LC	NRM-4	9.5 ± 1.2 μT
MC	4-50	0.9 ± 0.1 μT
HC	50-85	2.0 ± 0.1 μT

Note: The first column identifies each subsample and specifies whether the data presented for each row refers to a LC, MC, or HC magnetization component. The second column contains the AF range used for the paleointensity determination. The third column contains paleointensity values. Uncertainties are 95% confidence intervals determined using a two-tailed Student's *t*-test. All paleointensity values are computed assuming the components are thermally activated remanences.

table S4. Rock magnetic and hysteresis parameters.

Sample	M_{rs} (Am^2kg^{-1})	M_s (Am^2kg^{-1})	M_{rs}/M_s	H_{cr} (mT)	H_c (mT)	H_{cr}/H_c	R	MDF_{IRM} (mT)	MDF_{ARM} (mT)	Source
15498,282a	0.107			70			0.39	52	51	this study
15498,287b1	0.079	0.87	0.091	69	8.8	7.8				this study
15498,287b2	0.058	0.73	0.079	59	6.6	8.9				this study
15498,35	0.066	0.75	0.088	77	7.8	9.9				(*39*)

Note: The first column gives the subsample name, the second column shows the saturation remanent magnetization normalized by mass, the third column shows the saturation magnetization normalized by mass, the fourth column shows the ratio of saturation remanent magnetization to saturation magnetization, the fifth column shows coercivity of remanence, the sixth column shows coercivity, the seventh column shows the ratio of coercivity of remanence to coercivity, the eighth column shows the Cisowski *R*-value (*109*), and the ninth and tenth columns show the MDF of IRM and ARM, respectively (*110*). During our MDF experiments, we imparted ARM using a 200 mT AC field and a 2 mT DC field and IRM using a 200 mT DC field. The eleventh column shows the sources for the data.

table S5. Anisotropy of ARM (85-mT ac field with 0.01-mT dc field).

Subsample	Anisotropy degree *P*	Shape factor *T*
274d	1.10	0.70
282a	1.20	0.29
282b	1.16	0.44
282c	1.20	0.70
287a	1.08	-0.20
287b	1.08	0.15

Note: The first column contains the subsample name, the second column contains the degree of anisotropy *P*, and the third column contains the shape factor *T* of the anisotropy ellipsoid.

table S6. Complete $^{40}Ar/^{39}Ar$ incremental heating results.

#	Temp (°C)	^{40}Ar ± 1σ	^{39}Ar ± 1σ	^{38}Ar ± 1σ	^{37}Ar ± 1σ	^{36}Ar ± 1σ	$^{40}Ar^*$ (%)	$^{39}Ar_k$ (%)	$^{38}Ar_{cos}$ (%)	$^{38}Ar_{trap}$ (%)	$^{38}Ar_{Cl}$ (%)	$^{36}Ar_{cos}$ (%)	$^{36}Ar_{trap}$ (%)	Ca/K	$^{40}Ar/^{39}Ar$ Age ± 1s (Ma)	Apparent ^{38}Ar Exposure Age ± 1s (Ma)
15498-282-1		**whole-rock fragment**														
1	460 °C	1.36302 ± 0.00112	0.02550 ± 0.00035	0.00820 ± 0.00022	0.14454 ± 0.00101	0.00692 ± 0.00075	100.0	99.6	91.5	0.0	0.0	100.0	0.0	11.2	980 ± 31	153 ± 7
2	459 °C	0.75503 ± 0.00091	0.00998 ± 0.00028	0.00528 ± 0.00021	0.05918 ± 0.00066	0.00345 ± 0.00075	100.0	99.6	97.3	0.4	0.0	96.3	3.2	11.7	1270 ± 44	258 ± 20
3	513 °C	2.48711 ± 0.00211	0.01778 ± 0.00029	0.02699 ± 0.00022	0.24312 ± 0.00115	0.01780 ± 0.00075	100.0	99.0	98.9	0.3	0.0	97.1	2.6	27.1	1922 ± 50	350 ± 12
4	513 °C	1.53017 ± 0.00137	0.00774 ± 0.00028	0.01750 ± 0.00022	0.13218 ± 0.00090	0.01140 ± 0.00075	100.0	98.8	99.3	0.1	0.0	98.8	0.9	33.9	2357 ± 70	425 ± 32
5	566 °C	4.37503 ± 0.00303	0.01551 ± 0.00030	0.06628 ± 0.00024	0.43664 ± 0.00135	0.04332 ± 0.00076	100.0	98.0	99.6	0.1	0.0	98.7	1.1	56.3	2859 ± 63	499 ± 20
6	566 °C	2.51871 ± 0.00218	0.00765 ± 0.00029	0.04030 ± 0.00023	0.24826 ± 0.00119	0.02620 ± 0.00076	100.0	97.7	99.7	0.0	0.0	99.3	0.4	65.0	3088 ± 81	537 ± 41
7	619 °C	6.41119 ± 0.00362	0.01780 ± 0.00031	0.11943 ± 0.00027	0.70627 ± 0.00213	0.07820 ± 0.00076	100.0	97.2	99.7	0.1	0.0	98.6	1.2	80.0	3231 ± 64	562 ± 20
8	618 °C	3.55884 ± 0.00254	0.00955 ± 0.00030	0.06827 ± 0.00025	0.38961 ± 0.00136	0.04498 ± 0.00076	100.0	97.2	99.6	0.2	0.0	97.9	1.9	82.3	3284 ± 76	583 ± 37
9	671 °C	8.05683 ± 0.00431	0.02141 ± 0.00032	0.17160 ± 0.00030	0.97854 ± 0.00199	0.11300 ± 0.00078	100.0	96.8	99.6	0.2	0.0	98.0	1.8	92.5	3303 ± 63	585 ± 18
10	670 °C	4.26142 ± 0.00311	0.01121 ± 0.00029	0.09761 ± 0.00026	0.55884 ± 0.00169	0.06322 ± 0.00077	100.0	96.5	99.9	0.0	0.0	99.9	0.0	101.2	3323 ± 72	586 ± 31
11	722 °C	8.93960 ± 0.00470	0.02321 ± 0.00031	0.23182 ± 0.00043	1.29740 ± 0.00467	0.15162 ± 0.00078	100.0	96.1	99.7	0.1	0.0	98.8	1.0	114.0	3349 ± 63	601 ± 17
12	722 °C	4.52658 ± 0.00330	0.01194 ± 0.00028	0.12922 ± 0.00026	0.73581 ± 0.00176	0.08413 ± 0.00077	100.0	95.7	99.8	0.1	0.0	99.3	0.5	126.2	3332 ± 70	593 ± 29
13	777 °C	7.45697 ± 0.00571	0.02030 ± 0.00030	0.23362 ± 0.00037	1.29481 ± 0.00491	0.15296 ± 0.00079	100.0	95.6	99.8	0.1	0.0	98.7	1.1	130.8	3286 ± 63	609 ± 19
14	775 °C	3.35612 ± 0.00270	0.00875 ± 0.00028	0.11257 ± 0.00028	0.64050 ± 0.00177	0.07341 ± 0.00077	100.0	94.9	99.8	0.1	0.0	99.1	0.6	151.1	3362 ± 79	596 ± 40
15	829 °C	5.00366 ± 0.00351	0.01393 ± 0.00029	0.18433 ± 0.00030	1.01218 ± 0.00243	0.12372 ± 0.00078	100.0	94.9	99.4	0.5	0.0	95.9	3.9	150.0	3263 ± 67	615 ± 27
16	824 °C	1.94652 ± 0.00151	0.00536 ± 0.00027	0.07936 ± 0.00025	0.43715 ± 0.00151	0.05293 ± 0.00076	100.0	94.3	99.5	0.4	0.0	96.6	3.1	169.5	3289 ± 101	616 ± 66
17	879 °C	2.87663 ± 0.00250	0.00879 ± 0.00028	0.12810 ± 0.00026	0.67431 ± 0.00192	0.08866 ± 0.00077	100.0	94.7	99.0	0.9	0.0	92.6	7.2	158.9	3127 ± 76	640 ± 42
18	880 °C	1.13868 ± 0.00121	0.00354 ± 0.00027	0.05478 ± 0.00024	0.28965 ± 0.00134	0.03737 ± 0.00076	100.0	94.3	99.2	0.7	0.0	94.2	5.6	170.2	3109 ± 134	640 ± 103
19	931 °C	2.69626 ± 0.00280	0.00978 ± 0.00028	0.13364 ± 0.00029	0.66159 ± 0.00189	0.09743 ± 0.00078	100.0	95.3	98.2	1.7	0.0	87.2	12.6	139.1	2866 ± 71	672 ± 40
20	931 °C	1.05289 ± 0.00111	0.00358 ± 0.00027	0.06193 ± 0.00025	0.31788 ± 0.00148	0.04257 ± 0.00076	100.0	93.8	99.1	0.8	0.0	93.4	6.4	185.5	2983 ± 131	660 ± 105
21	982 °C	4.68186 ± 0.00341	0.01608 ± 0.00028	0.56377 ± 0.00056	2.86228 ± 0.01692	0.37317 ± 0.00094	100.0	87.6	99.7	0.3	0.0	97.5	2.3	398.1	3068 ± 65	693 ± 29
22	982 °C	0.92273 ± 0.00131	0.00335 ± 0.00027	0.13005 ± 0.00028	0.68687 ± 0.00201	0.08460 ± 0.00077	100.0	85.8	99.9	0.0	0.0	99.5	0.3	468.0	3017 ± 149	674 ± 124
23	1030 °C	2.27567 ± 0.00210	0.00836 ± 0.00028	0.61011 ± 0.00052	3.14172 ± 0.01662	0.39536 ± 0.00091	100.0	73.9	100.0	0.0	0.0	99.9	0.0	997.0	3222 ± 91	744 ± 68
24	1031 °C	0.42961 ± 0.00073	0.00186 ± 0.00027	0.11074 ± 0.00028	0.58569 ± 0.00197	0.07132 ± 0.00076	100.0	78.1	100.0	0.0	0.0	100.0	0.0	790.6	2899 ± 273	705 ± 256
25	1083 °C	1.74716 ± 0.00131	0.00971 ± 0.00029	1.00902 ± 0.00102	5.47803 ± 0.02425	0.65021 ± 0.00113	100.0	60.8	100.0	0.0	0.0	100.0	0.0	1817.8	2899 ± 91	798 ± 78
26	1082 °C	0.11198 ± 0.00031	0.00199 ± 0.00027	0.08025 ± 0.00026	0.43387 ± 0.00156	0.05117 ± 0.00076	100.0	84.8	100.0	0.0	0.0	100.0	0.0	504.5	1152 ± 138	664 ± 205

Isotope abundances given in nanoamps (spectrometer sensivity is ~1.12×10^{-14} mols/nA),
and corrected for ^{37}Ar and ^{39}Ar decay, half-lives of 35.2 days and 269 years, respectively,
and for spectrometer discrimination per atomic mass unit of 1.004535 ± 0.002968.

Isotope sources calculated using the reactor constants in Renne et al. (1998),
assuming $(^{38}Ar/^{36}Ar)_{cos} = 1.54$, $(^{38}Ar/^{36}Ar)_{trap} = 0.188$, and $(^{40}Ar/^{36}Ar)_{trap} = 0$.

No corrections were made for cosmogenic ^{40}Ar.

Ages calculated using the decay constants and standard calibration of Renne et al. (2011) and isotope abundances of Steiger and Jäger (1977)
and calculated relative to Hb3gr fluence monitor (1081 Ma). Corrections were made for reactor produced ^{38}Ar and ^{36}Ar in age calculations.
J-Value is 0.013415 ± 0.000521.

Average analytical blanks are: $^{40}Ar = 0.015$; $^{39}Ar = 0.0001$; $^{38}Ar = 0.00002$; $^{37}Ar = 0.0001$; $^{36}Ar = 0.00007$ (nanoamps).

Temperature was controlled with approximately ± 10 °C precision and ± 10 °C accuracy; each heating duration was 600 seconds.

The apparent ^{38}Ar exposure ages are calculated for ^{38}Ar production in K-glass and plagioclase solely from Ca, K, Fe and Ti; other sources are assumed to be negligible.

table S7. Oxide weight percent compositions of K-bearing phases in basalt clast 15498-282-1.

Oxide	Mean Feldspathic Glass	± 1σ	Mean K-glass	± 1σ
SiO_2	46.05	0.45	60.98	1.71
TiO_2	0.07	0.18	0.20	0.36
Al_2O_3	34.34	0.25	19.58	1.24
FeO	0.34	0.28	0.37	0.28
MnO	0.00	0.00	0.07	0.13
MgO	0.05	0.04	0.05	0.10
CaO	17.42	0.30	1.28	1.26
Na_2O	1.18	0.21	0.68	0.16
K_2O	0.07	0.04	13.84	1.90
Total	**99.51**	**0.71**	**97.06**	**3.15**

Note: The first column contains the oxide name. The second and third columns contain mean oxide weight percentages and corresponding standard deviation values for feldspathic glass in the basalt clast, respectively. The fourth and fifth columns contain mean oxide weight percentages and corresponding standard deviation values for K-rich glass in the basalt clast, respectively.

table S8. Summary of MP-MDD model parameters with cosmogenic ^{38}Ar production rates for 15498.

Phase	E_a (kJ/mol)	$\ln(D_o/a^2)_1$ [$\ln(s^{-1})$]	$F_{39\text{-}1}$	$F_{37\text{-}1}$	K/Ca_1	Fe/Ca_1	$P_{38}/[Ca]_1$ (mol/g_{Ca}/Ma)	$\ln(D_o/a^2)_2$ [$\ln(s^{-1})$]	$F_{39\text{-}2}$	$F_{37\text{-}2}$	K/Ca_2	Fe/Ca_2	$P_{38}/[Ca]_2$ (mol/g_{Ca}/Ma)
15498													
Feld. Glass	146	7.5	0.25	0.600	0.004	0.015	4.91×10^{-13}	2.5	0.15	0.397	0.004	0.015	4.91×10^{-13}
K-Glass	143	14.0	0.20	0.001	2.08	0.23	2.09×10^{-12}	8.0	0.40	0.002	2.08	0.23	2.09×10^{-12}

Note: Each phase is fit with a two-domain model. *F* is the fraction of $^{39}Ar_K$ or $^{37}Ar_{Ca}$ contained within a given domain and was calculated relative to the total gas released in the first 20 extractions. $P_{38}/[Ca]$ is the domain-specific production rate for $^{38}Ar_{cos}$ and is calculated based on the relative concentrations of Ca, K, Fe and Ti in feldspathic glass and K-rich glass, using the ^{38}Ar production rate of Ca from Turner (*115*), and relative production rates for K, Fe, and Ti from Eugster and Michel (*125*).

table S9. Summary of $^{40}Ar/^{39}Ar$ chronology for 15498.

$^{40}Ar/^{39}Ar$ Radioisotopic Age (Ma)					$^{38}Ar/^{37}Ar$ Exposure Age (Ma)				
Steps	**MSWD**	**Age**	**±**	**1σ ***	**Steps**	**MSWD**	**Age**	**±**	**1σ**
8-16	0.22	3310	±	24 (50)	8-18	0.28	600	±	8

Note: MSWD = mean square weighted deviation for age fits to release listed steps. Errors reflect analytical uncertainties on isotope measurements and do not include decay constant, standard age, *J*-value, or production rate uncertainties.
* 1σ error is 50 Ma when *J*-value, standard age, and decay constant uncertainty are included.

table S10. Reduced χ^2 misfit statistics for best-fit thermochronometry models for a variety of breccia formation ages.

	Impact age (Ma)						
	3300	**3000**	**2500**	**2000**	**1500**	**1000**	**650**
Peak impact temperature	675	611	566	556	546	538	Non-unique (525)
Best fit χ^2_u	11.1	7.2	5.4	5.3	5.7	6.2	Non-unique (6.7)
Effective daytime temperature	56	55	53	50	46	35	25

Note: The columns denote the different modeled impact ages. The first row contains values for the peak impact temperature experienced by the clast during the breccia formation event. The second row contains the best fit χ^2_u misfit values. The third row contains the effective temperature used to simulate 600 Myr of daytime heating at the lunar surface in each model. The 650 Ma impact model (final column) yielded non-unique extrapolated best fit χ^2_u solutions. Therefore, instead of showing an extrapolated best fit χ^2_u value and corresponding peak impact temperature, we present values for the individual model run with the lowest χ^2_u value (i.e, the model corresponding to a peak impact temperature of 525°C for the 650 Ma impact event).